# The Performance of a Waveguide-Coupled

# Metal-Semiconductor-Metal Optoelectronic Matrix Switch

The Performance of a Waveguide-Coupled

Metal-Semiconductor-Metal Optoelectronic Matrix Switch

by

Ying Liu, B.Sc and M.Sc

A Thesis

Submitted to the School of Graduate Studies

in Partial Fulfillment of the Requirements

For the Degree

Master of Engineering

June 1998

Master of Engineering (1998)                    McMaster University

Department of Engineering Physics               Hamilton, Ontario


Title:         The Performance of a Waveguide-Coupled Metal-Semiconductor-Metal

               Optoelectronic Matrix Switch

Author:        Ying Liu, B.Sc. (Peking University) and M.Sc. (Nankai University)

Supervisor:    Dr. Paul E. Jessop

No. of pages:  i-xiii, 1-105

# ABSTRACT

Metal-semiconductor-metal (MSM) photodetectors are becoming attractive devices for optoelectronic integrated circuits due to their high speed and simplicity. Optoelectronic matrix switches based on MSM detector arrays offer many advantages such as zero-bias off-state, low bias voltage, high speed and large bandwidth. While in many applications the optical input is coupled in through the top surface of the device, optical signals can also be distributed through transparent waveguides that are located below the absorbing detector layer. Such waveguide-coupled detectors will act as optical taps when the coupling between the waveguide and detector layers is well under control. In this thesis, a 4×4 MSM waveguide-coupled optoelectronic matrix switch was demonstrated and analyzed. The strength of the coupling between the waveguide and detector layers was predicted theoretically and confirmed experimentally. Franz-Keldysh effect in this device was also demonstrated.

# ACKNOWLEDGMENTS

# TABLE OF CONTENTS

# LIST OF FIGURES

# LIST OF TABLES

# CHAPTER 1    INTRODUCTION

## 1.1 Overview

Optical communication is now an important practical technology for long-distance transport of wide-band signals. The application of photonic methods in computing, signal processing, and routing broad-band signals is foreseeable. Photonics is particularly promising for switching broadband signals where the high frequencies involved would require exotic electronic devices, or where electronic signal routing becomes a problem because of electromagnetic coupling among circuits.

Planar optoelectronic integrated circuits that switch or process light propagating in optical waveguides become more and more attractive due to their high-speed operation. Waveguide-coupled photodetectors are now important components in many advanced photonic integrated circuits[1.1,1.2]. Such detectors can be applied to areas of wavelength division multiplexed receivers[1.3-1.5], optoelectronic switches[1.6], and time delay networks for microwave phased arrays [1.7, 1.8].

Most waveguide-coupled detectors are based on evanescent coupling between a transparent passive waveguide and a smaller bandgap absorbing layer that is grown above the guiding layer. Such detectors are usually intended to terminate the waveguide, converting all of the optical power to photocurrent. However, in some applications it is necessary to distribute the optical power in a waveguide among the elements of a detector array. A key element for such circuits is a high-speed optical tap that samples a small part of the light in a waveguide and converts it to an electrical signal while allowing most of the light to continue through for further signal processing. This can be achieved by placing a series of detectors in-line on a single waveguide and controlling the waveguide-to-detector coupling so that each detector element acts as an optical tap, removing only a controlled fraction of the optical power.

Among the photodetectors that have been developed so far for lightwave applications, such as photoconductors, metal-semiconductor-metal (MSM) photodiodes, p-i-n photodiodes, and

avalanche photodiodes, MSM detectors have developed into one of the most promising photodetectors for receivers in optoelectronic integrated circuits due to their speed and simplicity.

MSM photodetectors consist of interdigitated metal contacts deposited on semiconductor substrates to form Schottky barriers. When a voltage is applied, one of the barriers is under forward bias; the other is reverse biased whose depletion region spans the channel between the contacts. Absorption occurs near the semiconductor surface between the electrodes.

The positive attributes of MSMs are numerous. These include large bandwidth, zero off-state power consumption, low bias voltage, high performance and easy fabrication [1.10], [1.11]. They do not add significantly to the complexity of the whole circuit. Also the response time is short [1.12], [1.13]. Based on an interdigitated Schottky contact structure, the MSM photodetectors also have low dark current [1.14, 1.15], and process compatibility with high-performance field-effect transistors [1.10, 1.16], which make it suitable for monolithic integration of optoelectronic circuits.

These advantages have made the MSM photodetectors an attractive device for optoelectronic integrated circuit[1.17,1.18], high-speed receivers in optical communication[1.19,1.20] and high-speed optically controlled digital integrated circuits[1.18]. Especially, MSM detector arrays can act as matrix switches because of their zero-bias off-state, low bias voltage, high speed and large bandwidth.

A matrix switch must deliver any one signal from a set of signals presented at its input ports to any of the output ports (Fig.1.1). In the optoelectronic version of a matrix switch the optical power in each input signal is divided among a group of photodetectors, one associated with each of the output ports. The responses of all photodetectors associated with a single output port are electrically summed. Switching is obtained by controlling the sensitivity of the photodetectors; if they are sensitive to the signal, a cross-point connection is made. The number of cross-points required for full connection of all the nodes increases as $N^2$.
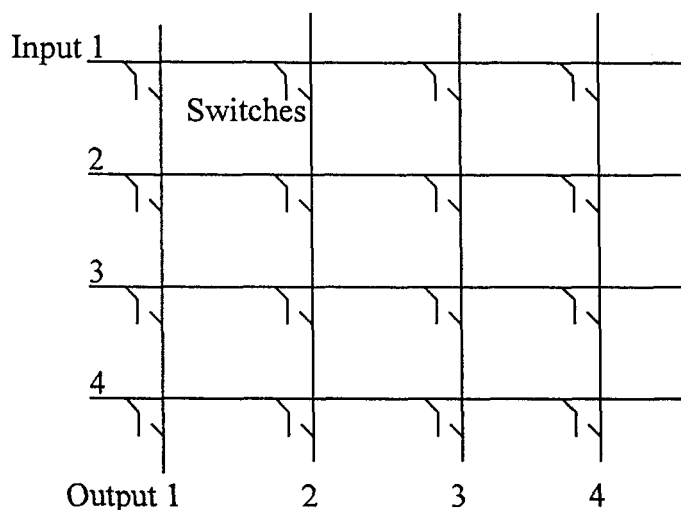
**Fig.1.1** Structure of an N×N (here as an example, 4×4) matrix switch.

Up to now, the reported experimental optoelectronic switch matrices have employed several different types of optical networks for signal distribution – such as fused junctions, fiber power splitters, and fiber-coupled planar waveguide splitters [1.9] among which fibers have been used quite a lot as power splitters in some networks. In this case the complexity of the matrix switches with a large number of elements and the need to align fibers precisely to the individual detector elements become obstacles to practical implementation.

In the mean time, group III-V semiconductor materials are playing an increasingly important role in integrated optics, especially in the construction of active components such as optical switches and modulators. It is recognized that the integration of the signal-distribution waveguide with the semiconductor detector array would greatly simplify manufacturing. Manufacturing costs could be reduced and reliability improved by integrating optical waveguides into the matrix structure to distribute the lightwave signal on-chip without the use of optical fiber splitters.

In this thesis, we report the integration of AlGaAs rib waveguides into a 4×4 array of GaAs metal-semiconductor-metal detectors. In our system the information is carried via optical fibers and injected into a semiconductor waveguide-detector structure. The optical signal is distributed

to the detectors by routing it through transparent waveguides that are located directly below the absorbing detector layers. Thus the optical signal can thus be shared among a series of detectors as is required in optoelectronic switching applications.

## 1.2 Device Structure and Some Basic Characteristics of the Detectors

Our device was fabricated from a wafer with the structure shown in Fig.1.2. It was grown at the Communication Research Centre (CRC). Fig.1.3 is the structure of our GaAs MSM photodetector integrated with AlGaAs rib waveguides. A 0.75μm thick waveguide layer, $Al_{0.20}Ga_{0.80}As$ cladding layers and a 0.4μm thick GaAs absorbing layer were grown on undoped GaAs substrates by metal organic chemical vapor deposition (MOCVD). All layers were undoped with nominal background carrier concentrations of less than $5 \times 10^{14} cm^{-3}$. The thickness of the upper and lower cladding layers were 0.3 and 2.2μm, respectively. A series of straight parallel rib waveguides was patterned using wet chemical etching. Rib widths were 3 and 10μm. The absorbing layer was removed everywhere except for small mesas distributed along the waveguides to form the detector elements. Prior to metallization a dielectric layer was deposited with windows opened above the mesas for the integrated metal-semiconductor contacts. The metal was Ti:Pt:Au with 2μm finger width and spacing.

Light is coupled in at the cleaved end facet of the waveguide. The optical signal is distributed to the detectors by routing the optical signal through transparent waveguides that are located directly below the absorbing detector layers. The amount of optical power absorbed in each detector section can be controlled by adjusting the degree of coupling between detector layer and waveguide layer. Modeling of the devices was carried out in terms of the transverse electric slab-waveguide modes and also using the two-dimensional beam propagation method (BPM) [1.21].

GaAs 0.40μm — Detector Layer

20% GaAlAs 0.30μm — Confining/Isolation Layer

15% GaAlAs 0.75μm — Waveguide Layer

20% GaAlAs 2.23μm — Confining Layer

GaAs 0.50μm — Buffer Layer

GaAs — Substrate
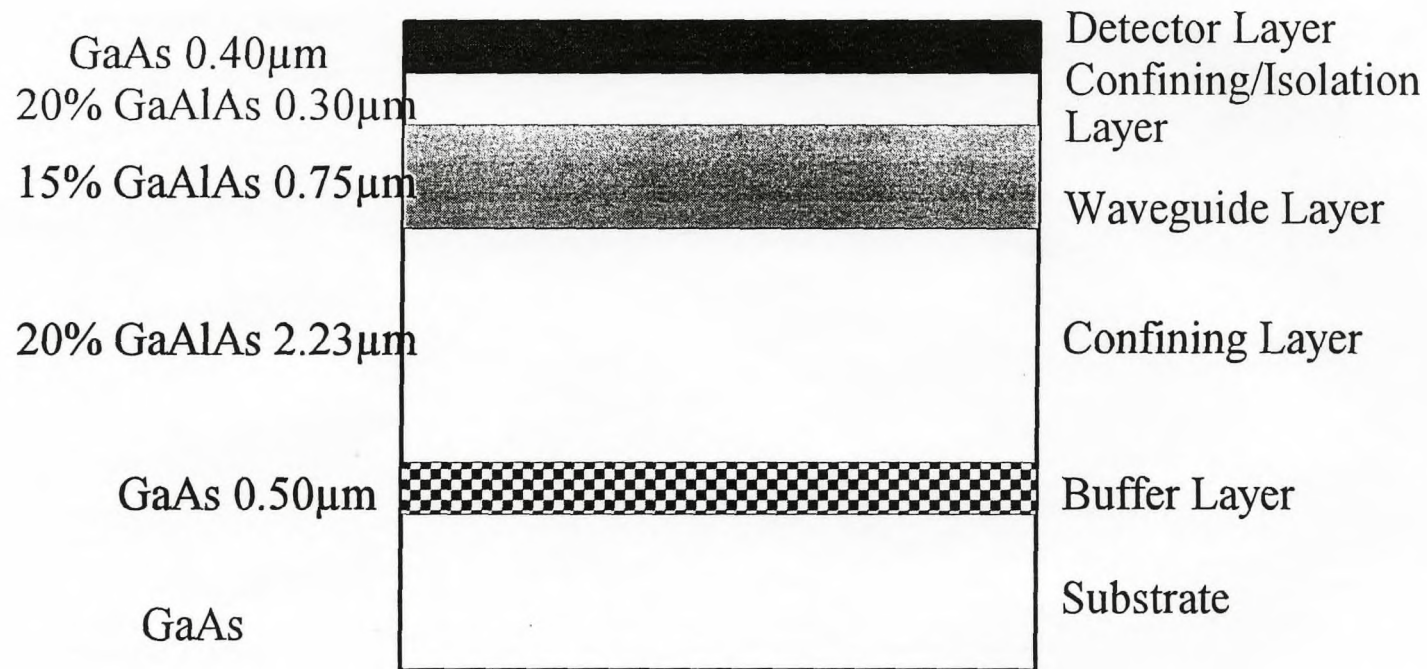
Fig. 1.2 Wafer #94-095 single-mode waveguide/detector structure.
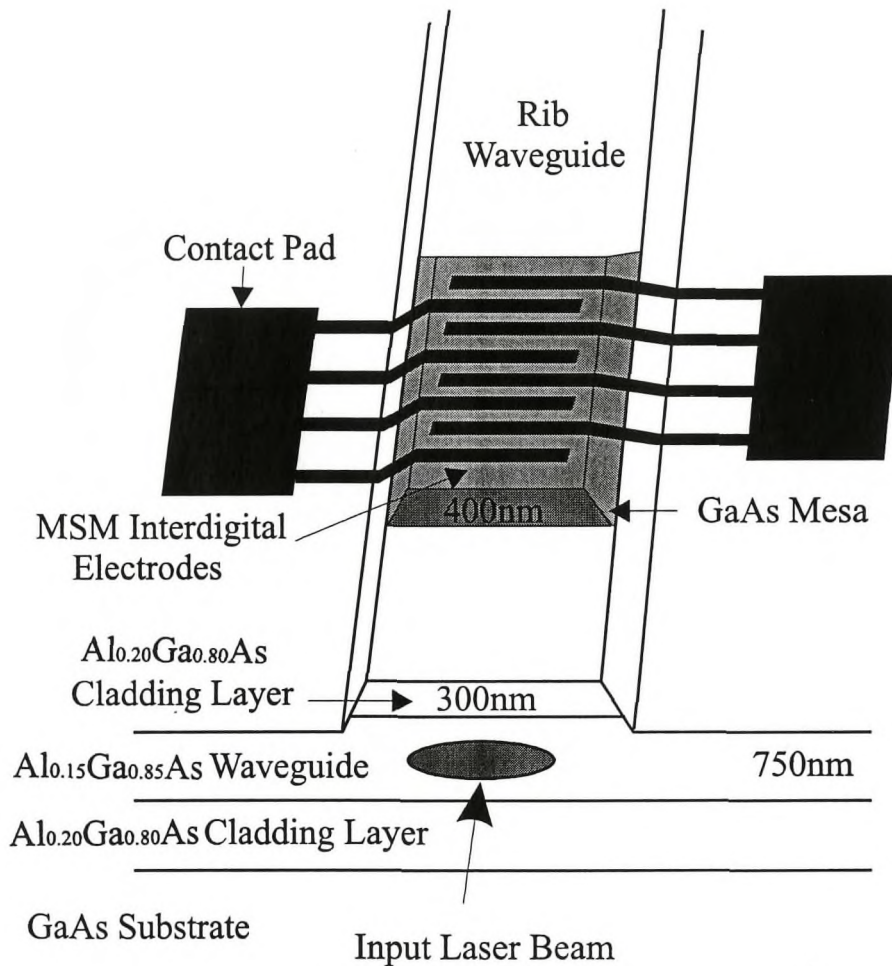
Fig. 1.3 Structure of the metal-semiconductor-metal waveguide-coupled photodetector.

Fig.1.4 illustrates the 4×4 matrix switch used in our work, which consists of an interconnected array of MSM photodiodes. Each of the input lightwave signals is divided among all of the detectors in a row of the matrix. Electrodes are put on the contacts of the detectors directly. All of the detectors in a column are electrically connected so that their output signals are summed. Switching action relies on the fact that the photo-response of an individual detector is reduced effectively to zero when its bias voltage is set to zero. Connections are made simply by biasing

detectors at the desired crosspoints.

The matrix switch was fabricated using ten-micron wide parallel waveguides spaced 300μm apart. Along each waveguide the detector lengths were 45, 63, 106 and 177μm. These values were selected in an effort to equalize the power absorbed in each detector, based on a preliminary estimate of a 3dB attenuation length of 110μm[1.21].

Figure 1.5(a) shows the photocurrent in the first detector as a function of bias voltage for a series of input power levels at a wavelength of 820nm. Figure 1.5(b) shows the photocurrent in all four detectors in a line, as a function of bias voltage for a fixed optical input power level of 450μw. The dark currents of the in-line detectors are shown in Fig.1.6.
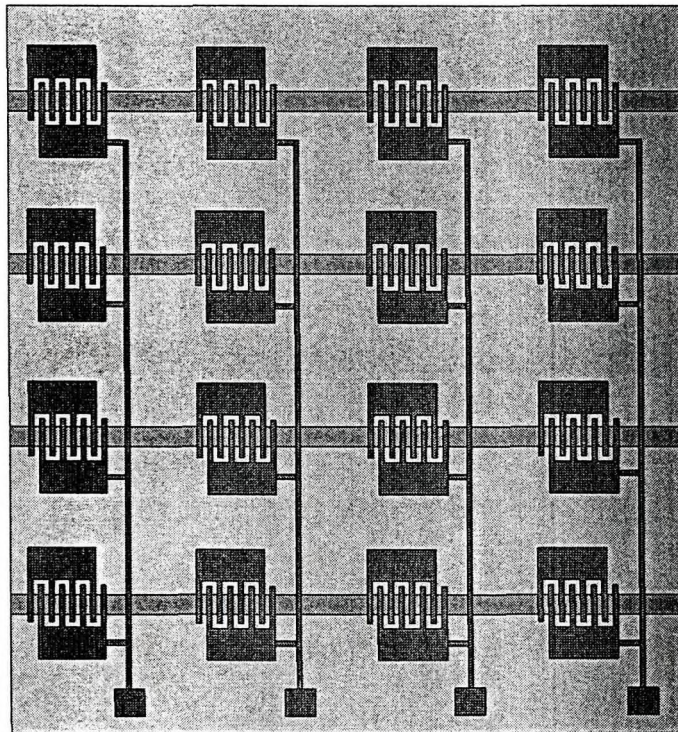


Fig. 1.4 Layout of the 4×4 MSM photodetector array in our experiment.
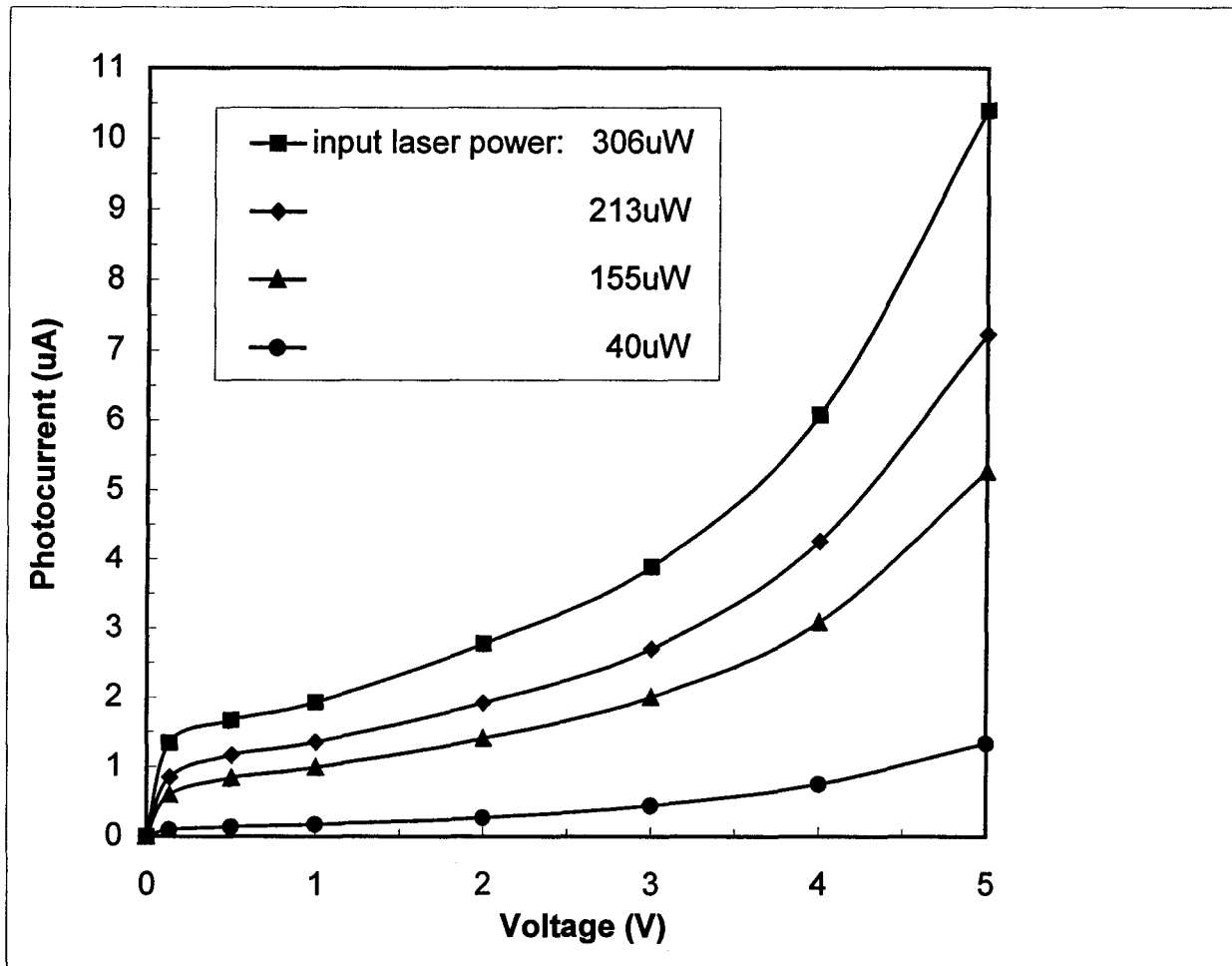
Figure 1.5(a)  I-V characteristics of the first photodetector in the array as a function of bias voltage for a series of input power levels at a wavelength of 820nm.
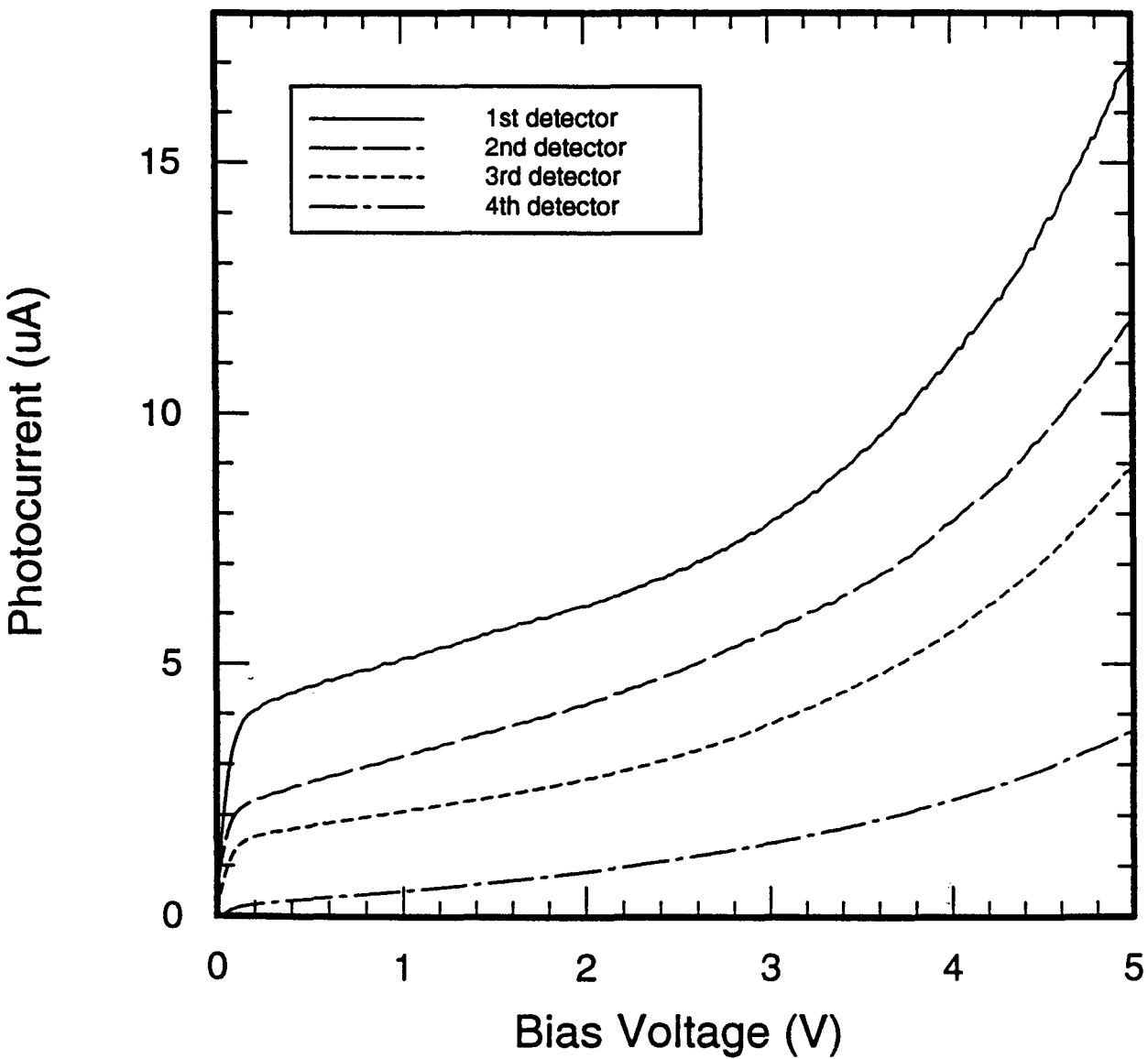
**Figure 1.5(b)** I-V characteristics of the four in-line photodetectors for a fixed optical input power level of 450μw at wavelength 820nm.
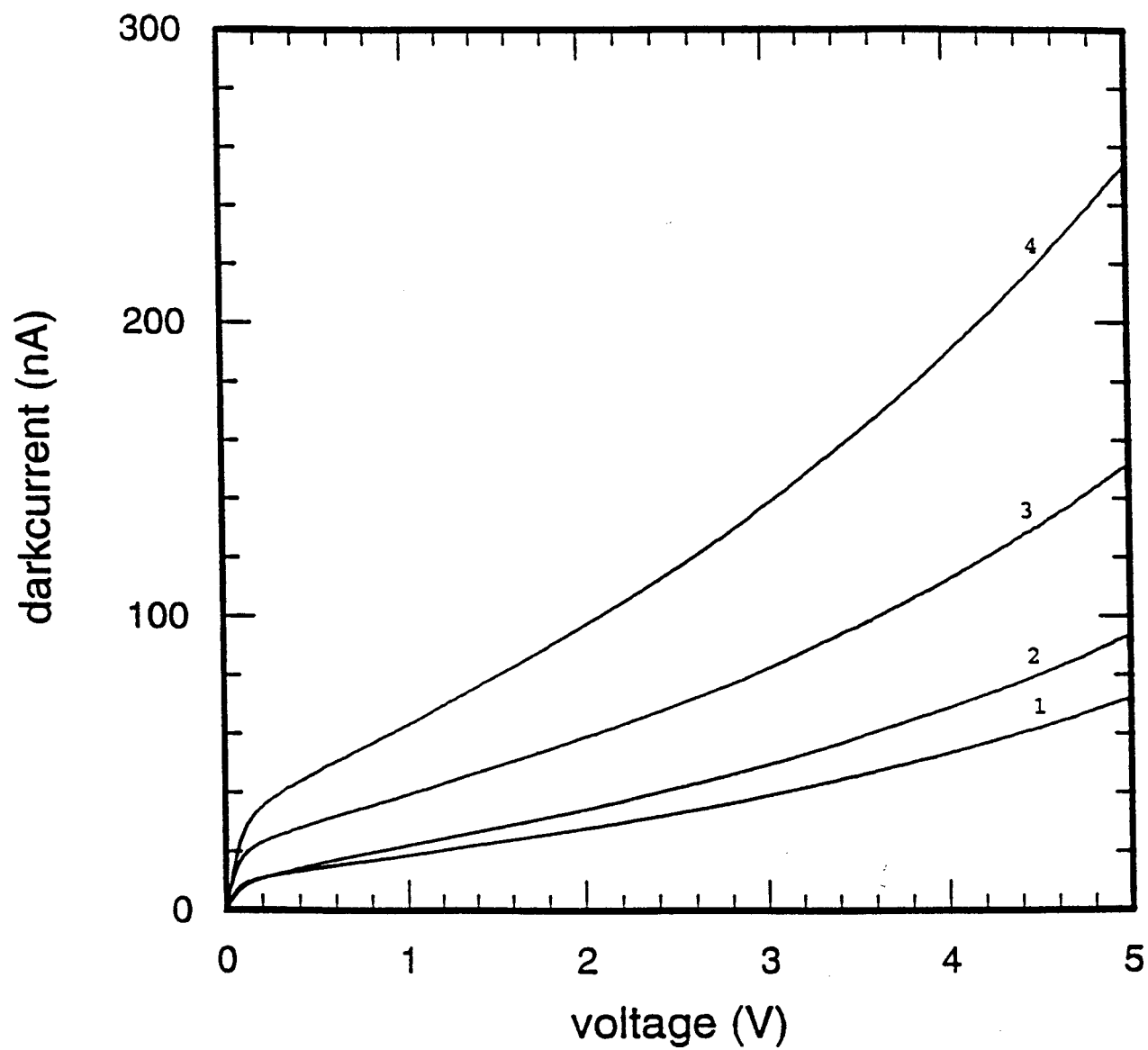
**Figure 1.6**     Dark currents of the four inline photodetectors.

## 1.3 Contents of the Thesis

In the previous work, which was done by Mike Ersoni [1.22], the feasibility of the integration of MSM photodetectors and waveguides into an optoelectronic switch was examined. The optical characterization of both passive and detector regions and high speed performance were measured. The aim of my thesis is to extend this initial work and improve our knowledge of the important device design parameters. In particular, the strength of the coupling between the waveguide and detector layers was predicted to have a complex oscillatory behavior, as a function of the absorber layer thickness. This behavior was modeled and then confirmed experimentally. Also, the thesis examines the use of in-line waveguide coupled MSM photodetectors at wavelengths near the absorption band edge. In this wavelengh range, absorption is enhanced due to Franz-Keldysh effect, which makes possible more efficient use of the input power. It is also possible to use in-line detectors as wavelength monitors when they are operated near the absorption band edge. The use of our waveguide coupled MSM detectors for this somewhat different application is also considered in this thesis.

In Chapter 2, we present a simple analytical model of the bias dependent photocurrent for the MSMs so that we can have a clear idea of the I-V characteristics of the MSM detectors. This analysis helps understanding of the optical behavior of the MSMs at different biases.

Chapter 3 focuses on the investigation of the enhanced coupling between waveguide layer and integrated detector layer. An oscillatory behavior of the absorption coefficient as a function of the absorbing layer thickness was predicted using a beam propagation method (BPM) analysis. This theoretical prediction was confirmed by measuring the absorption coefficients of a series of optical waveguide taps with varying absorber thicknesses for an operating wavelength of 820nm. By taking advantage of this thickness dependence, we can have better control of the power tapped in the detector region, which is very important in the operation of matrix switches.

We explored the Franz-Keldysh effect in our device in Chapter 4. Much work on the Franz-Keldysh effect in III-V devices has proven useful in miniature, high-speed, absorptive light-modulators [1.23, 1.24]. In our experiment, we observed the photocurrent increase as the electric

field applied increases at wavelength 890nm. In order to simulate a wide range of coupling strength, the diode laser was replaced by a titanium:sapphire laser that could be tuned continuously on either side of the GaAs band edge to vary the absorption coefficient.

An additional experiment was conducted as to the possibility of a wavelength monitor for the inline photodetectors in our device and presented in Chapter 5.

In Chapter 6, the crosstalk in the device is discussed; both electrical and optical crosstalks are included. Ways of reducing the crosstalk are also suggested.

Finally, a conclusion is given in Chapter 7.

# Chapter 2  Analytical Model of Photocurrent of MSM Photodetectors

## 2.1 Introduction

The current-voltage (I-V) characteristics of metal-semiconductor-metal (MSM) photodetectors under various light intensities will be analytically examined in this chapter. Typical I-V characteristics of a MSM photodetector show an initial increase in photocurrent followed by saturation as bias increases before breakdown occurs. So far, several explanations have been proposed to account for a qualitative increase of photocurrent, and hence gain or sensitivity, of MSM's with applied electric field. These include: 1) Sugeta et al. [2.1] argued that under bias holes are accumulated at the cathode because of the presence of a thin nonintentional insulating layer, which causes electron injection from the cathode and hence an increase of current. 2) Slayman and Figueroa [2.2] suggested that long-life traps in the semiconductor are filled by photoexcited carriers and cause an increase in conductivity and hence photoconductive gain. 3) According to Wei et al. [2.3] large applied bias produces a concave conduction band and hence electron accumulation at the anode, which causes hole injection from the anode and hence an increase of current.

All these models often require numerical simulations and can be used to examine bias dependence of photocurrent at high biases. A closed-form formula for the description of current-voltage relationship of MSM's under different light intensities in all regions of operation has been presented by Liann-Chern Liou and Bahram Nabet [2.4] in which analysis of the photocurrent is based on drift collection of carriers in the depletion regions of the cathode and anode and diffusion and recombination of carriers in the undepleted region. The equations are derived by directly solving the diffusion equation for a one-dimensional back-to-back Schottky diode model with boundary conditions. This theoretical model for bias dependence in all regions of operation except for breakdown is used to explain the MSM I-V characteristics here.

## 2.2 Analysis

The energy band diagram of a MSM device is shown in Fig.2.1. Assuming that the metal contacts form a Schottky barrier, it is clear that an MSM structure is basically two Schottky barriers connected back to back. Under an applied voltage, one of the contacts, contact No.1, called cathode, is reverse biased and the other, contact No.2, called anode, is forward biased. An increase in the applied bias results in an increase in the depletion region at the cathode as most of the voltage is dropped across this reverse biased junction. The voltage at which the whole region between contacts is depleted is the reach-through voltage ($V_{rt}$), which is illustrated in Fig.2.2(a)[after Ref.2.5]. A further increase of bias extends the depletion region toward the anode.
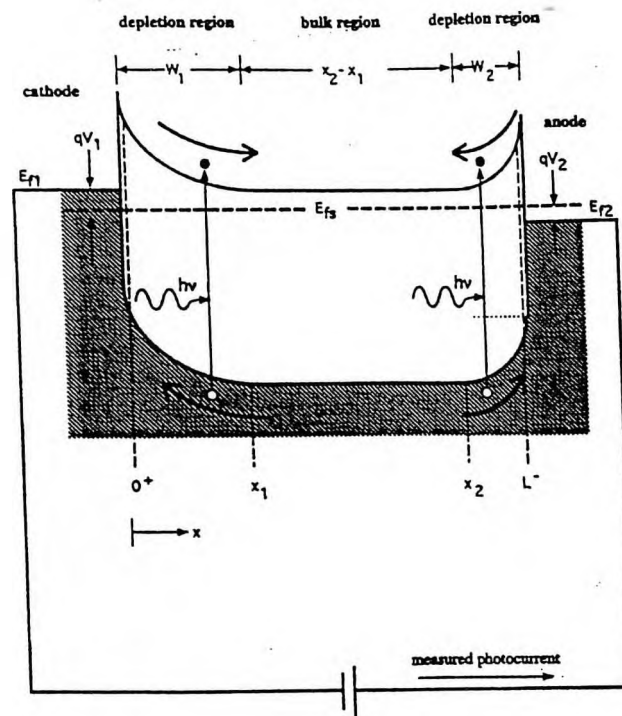


**Figure 2.1**    Energy band diagram of a MSM device under applied bias voltage. [after ref.2.4]

The voltage at which the electric field at the anode reaches zero is called the flat-band voltage ($V_{fb}$), shown in Fig.2.2(b). For voltages larger than $V_{fb}$, the energy band is bent further downward as illustrated in Fig.2.2(c); breakdown occurs and dark current dominates the response. The maximum voltage that can be applied to the MSM structure is limited by the avalanche breakdown near the maximum field at contact No.1.

The total current of a MSM photodetector is the sum of the photocurrents at the cathode, which is reverse biased by $V_1$, and the anode, which is forward biased by $V_2$ and is

$$J = J_{0+} + J_{L-}$$ (2.1)

Here $J_{0+}$ and $J_{L-}$ are the current at the metal-semiconductor junction on the semiconductor side of the cathode and anode, respectively.

Let us assume that the optically generated carriers are in transit in the depleted regions for a duration of much less than the recombination lifetime and that the optical response dominates the dark current flow. In this case, carrier recombination can be neglected and the continuity equation in the depletion regions can be written as

$$-\frac{1}{q}\frac{\partial J}{\partial x} + G = 0$$ (2.2)

where q is the electron charge and G, the carrier generation rate. Integrating the above results in

$$J_{0+} = J_{x1} - qGW_1$$ (2.3)

$$J_{L-} = J_{x2} + qGW_2$$ (2.4)

where $W_1$ and $W_2$ are the depletion region width of the cathode and anode and $J_{x1}$ and $J_{x2}$ are currents at the edge of the depletion region of the cathode and anode, respectively. These currents are due primarily to diffusion of minority carriers, holes and electrons, toward the cathode and anode, respectively, and are also affected by recombination with electrons accumulated in the concave shape of the conduction band. The contribution from thermionic emission of carriers from contacts to these currents is neglected since the optical response is several orders of magnitude higher than the dark current.
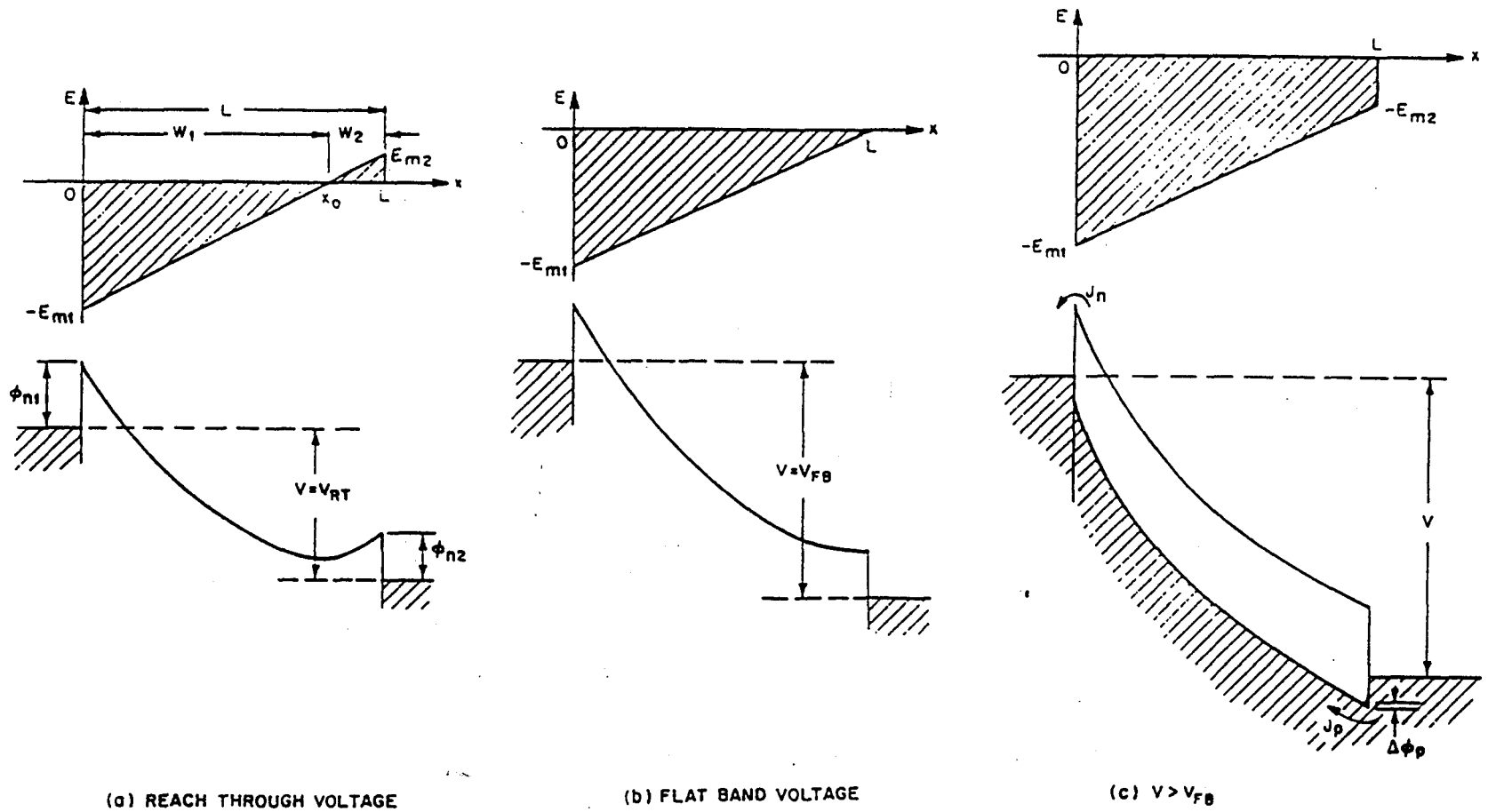
**Figure 2.2**    (a) Condition of reach-through: the two depletion regions touch each other; (b) Condition of flat-band: the energy band at x=L becomes flat; (c) Condition for applied voltage larger than $V_{FB}$. [after ref.2.5]

Consider the following diffusion equation

$$D_p \frac{d^2 \delta p}{dx^2} - \frac{\delta p}{\tau_p} + G = 0 \qquad (2.5)$$

where $D_p$ is the diffusion coefficient, $\tau_p$ is the lifetime, and $\delta p$ is the excess hole concentration. Since the electric field at the cathode is large, we can assume that there is no excess of holes at the edge of its depletion region,

$$\delta p = -P_{n0} \qquad \text{at } x = x_1, \qquad (2.6)$$

where $P_{n0}$ stands for the equilibrium hole concentration.

Because of the asymmetry of the electric field distribution of the photodetector, the boundary condition at the anode is not the same as at the cathode. This condition can be written as

$$-qD_p \frac{d\delta p}{dx} = qGf \qquad \text{at } x = x_2, \qquad (2.7)$$

where f is a function of applied bias and light intensity and is in units of length which can be interpreted as the effective diffusion length [2.4].

With these boundary conditions, Eq.(2.5) is solved as

$$\delta p(x) = A \exp(x / L_p) + B \exp(-x / L_p) + \frac{L_p^2}{D_p} G \qquad (2.8)$$

where A and B are

$$A = \frac{-(p_{n0} + G\tau_p)\exp(-x_2 / L_p) - \dfrac{L_p Gf}{D_p}\exp(-x_1 / L_p)}{2\cosh\left(\dfrac{x_2 - x_1}{L_p}\right)} \qquad (2.9a)$$

$$B = \cfrac{-(p_{n0} + G\tau_p)\exp(x_2 / L_p) + \cfrac{L_p Gf}{D_p}\exp(x_1 / L_p)}{2\cosh\left(\cfrac{x_2 - x_1}{L_p}\right)} \qquad (2.9b)$$

Here $x_2 - x_1$ is the width of the undepleted region.

Then we differentiate Eq.(2.8) and evaluate it at $x_1$. This leads to the diffusion current density as

$$J_{x1} = -qD_p\left.\frac{\partial \delta p}{\partial x}\right|_{x=x1}$$

$$= \left(-\frac{qD_p}{L_p}\right)\left[\cfrac{(G\tau_p + P_{n0})\sinh\left(\cfrac{x_2 - x_1}{L_p}\right) - \cfrac{L_p Gf}{D_p}}{\cosh\left(\cfrac{x_2 - x_1}{L_p}\right)}\right] \qquad (2.10a)$$

$J_{x2}$ is given by the boundary condition Eq.(2.7), that is,

$$J_{x2} = -qD_p\left.\frac{d\delta p}{dx}\right|_{x=x2} = qGf \qquad (2.10b)$$

The total current was obtained from Eqs.(2.1), (2.3), and (2.4)

$$J = J_{x1} + J_{x2} - qG(W_1 - W_2) \qquad (2.11)$$

Neglecting $P_{n0}$ and substituting Eqs. (2.7) and (2.10) into Eq.(2.11), the photocurrent of the MSM photodetector is expressed as

$$J = -qG(W_1 - W_2) - qGL_p \tanh\left(\frac{x_2 - x_1}{L_p}\right) + qGf \sec h\left(\frac{x_2 - x_1}{L_p}\right) + qGf \qquad (2.12)$$

In Eq.(2.12), the first term is due to the electron-hole pairs that are generated in the depletion regions of the cathode and anode. The other terms are the contributions of the holes generated in the undepleted regions $(x_2 - x_1)$ between the cathode and anode. The middle two terms are due to the carriers generated in the bulk and extracted at the end of the cathode depletion region. The last term is the current that is due to extraction of holes at the anode end and has a sign opposite the first term. To demonstrate the generality of this equation, in the following we will discuss several special cases.

## 2.3 Special Cases of Bias Values and Corresponding Photocurrents

### 2.3.1 Bias Values Below Reach Through

For applied bias such that the undepleted bulk region is much larger than the diffusion length, we have the approximations $\tanh((x_2-x_1)/L_p)=1$ and $\operatorname{csch}((x_2-x_1)/L_p)=0$, and Eq.(2.12) is reduced to

$$J = -qG(W_1 + L_p) + qG(W_2 + f) \qquad \text{for } x_2-x_1 \gg L_p, \qquad (2.13)$$

This equation shows that carriers generated in the cathode depletion region and holes within a diffusion length of its edge produce the cathode current whereas holes generated in the anode depletion region and within a distance f its edge comprise the anode current. The parameter f shows the average distance that holes diffuse toward the anode and are then swept by the electric field and collected, so f can be termed the effective anode diffusion length. Since the electric field at the cathode and anode depletion edges differ because of a much larger potential drop across the cathode, parameters $L_p$ and f are not generally equal.

However, for small values of voltage, equal numbers of holes can diffuse to the anode or cathode and the device becomes almost symmetrical, that is, $f=L_p$, in which case Eq.(2.12) is

reduced to

$$J = -qG(W_1 - W_2) \qquad \text{for small V,} \qquad (2.14)$$

It is noteworthy that it becomes zero if no bias is applied.

## 2.3.2 Bias Values Close to Reach Through

For high-speed devices, the undepleted region is smaller than a diffusion length. Since application of bias further reduces this distance, Eq.(2.12) is modified for $(x_2-x_1) \ll L_p$ by setting $\tanh((x_2-x_1)/L_p)=(x_2-x_1)/L_p$ and $\text{sech}((x_2-x_1)/L_p)=1$. Thus we get

$$J = -qG(W_1 - W_2) - qG(x_2 - x_1) + 2qGf \qquad \text{for } x_2-x_1 \ll L_p \qquad (2.15)$$

The maximum value that f can assume is $(x_2-x_1)$, which corresponds to the case when all the carriers generated in the bulk diffuse to the anode. In this case Eq.(2.15) becomes

$$J = -qG(W_1 - W_2) + qG(x_2 - x_1) \qquad (2.16)$$

This underestimates the total hole current but allows that not all the electrons generated in the depletion regions are collected as indicated by the first term of the Eq.(2.16). This provides a good match with experiment [2.4].

## 2.3.3 Bias Values above Reach Through

When the depletion regions between the cathode and anode meet, the length of the undepleted region is zero and from Eq.(2.15) or Eq.(2.16), the photocurrent is obtained as

$$J = -qG(W_1 - W_2) \qquad (2.17)$$

For higher bias values, the depletion region of the cathode impinges on the anode until the

electric field at the anode becomes zero. For voltages higher than the flat-band voltage, the detector current is given by

$$J = -qGL \qquad (2.18)$$

Here L is the distance between electrodes. For voltages higher than flat-band voltage but before breakdown, the current is expected to remain constant.

## 2.3.4 High-Bias Region

For very large values of applied bias, breakdown at the cathode causes a fast rise of dark current to the extent that it dominates the response. Since the above derivation is concerned with the collection of optically generated carriers, it does not apply to the high-bias region.

The closed-form solution thus derived agrees with physical expectations [2.4]. It predicts the photocurrent-voltage characteristics of our MSM photodetectors and our measured photocurrents show an initial increase followed by saturation as bias increases before breakdown happens.

## Chapter 3  Enhanced Coupling Between Absorbing Layer and Waveguide Layer

### 3.1 Introduction

The advantage of compact integrated waveguide-detector couplers (IWDCs) is that the coupling of optical power out of the waveguide occurs within the detector region. The IWDC is a versatile component for device applications. For example, an IWDC placed in-line with an integrated laser diode can function as a monitor photodetector. Also, to distribute optically a point-to-multipoint signal, a set of IWDCs can be located along a single waveguide. The application that is of particular interest for this thesis is the use of an IWDC as a switching element in an optoelectronic switching matrix.

An optical tap that extracts a controlled fraction of the optical power propagating in a waveguide and converts it to a photocurrent is a common component in semiconductor photonic integrated circuits. In order to design waveguide-coupled detectors that tap off a controlled fraction of the guided optical power, the degree of coupling between the waveguiding and absorbing layers must be controlled precisely. This coupling depends in detail on the thicknesses and refractive indices of the waveguide and detector layers and the buffer layer that separates them. It will be shown theoretically in this chapter that for thin absorbing layers the coupling does not simply increase monotonically with layer thickness, but has an oscillatory behaviour and exhibits a pronounced enhancement at specific thicknesses associated with the cutoff of low order waveguide modes. Experiments were conducted to confirm this prediction. This effect must be considered when waveguide photodetectors and optical taps are designed. In our case, to obtain precise control of the optical coupling rather than the maximum coupling strength, thicker absorber layers which are outside the oscillatory range are chosen.

### 3.2 Analysis of Optical Waveguide Modes

A prerequisite to an understanding of guided-wave interactions is a knowledge of the properties

of the guided modes. From Maxwell's equations in an isotropic, lossless dielectric medium we have

$$\nabla \times E = -\mu_0 \frac{\partial H}{\partial t} \tag{3.1a}$$

$$\nabla \times H = \epsilon_0 n^2 \frac{\partial E}{\partial t} \tag{3.1b}$$

where $\epsilon_0$ and $\mu_0$ are the dielectric permittivity and magnetic permeability of free space, respectively, and n is the refractive index. In the orthogonal coordinate system (x,y,z), suppose that the light wave propagates along the z direction with the propagation constant $\beta$ (Fig.3.1). The electromagnetic fields varies as

$$E = E(x,y) \cdot \exp j(\omega t - \beta z) \tag{3.2a}$$

$$H = H(x,y) \cdot \exp j(\omega t - \beta z) \tag{3.2b}$$

Fig. 3.1 Structure of a planar waveguide.
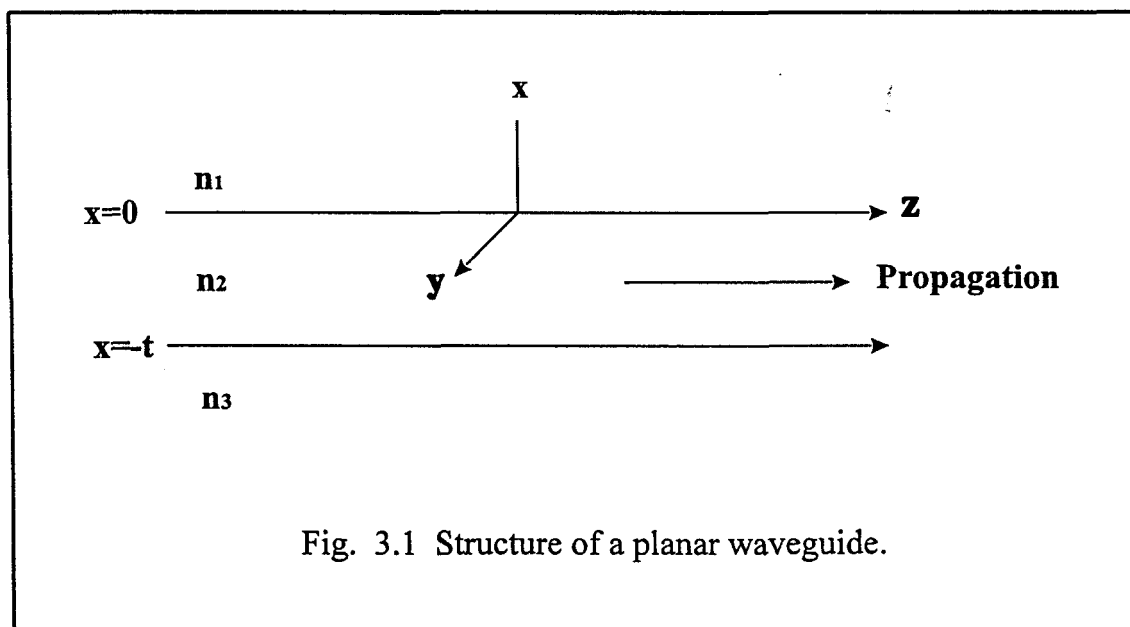
where the angular frequency $\omega = 2\pi c/\lambda$, and c is the light velocity in free space ($c=1/(\epsilon_0\mu_0)^{1/2}$) and $\lambda$ is the wavelength in free space.

The basic features of the behaviour of dielectric waveguides can be extracted from a planar model in which no variation exists in one, say, the y dimension. In the case of 3D structures, it can be approximated by using 2D calculations such as effective index method [3.1, 3.2]. Because of this and of the immense mathematical simplification that results, we will limit our treatment to planar waveguides. Accordingly, since $\partial/\partial t = j\omega$, $\partial/\partial z = -j\beta$ and $\partial/\partial y = 0$, the above equations yield two different modes with mutually orthogonal polarization states, i.e., the TE mode, which consists of the field components $E_y$, $H_x$ and $H_z$ and the other, TM mode, which has $E_x$, $H_y$ and $E_z$. The wave equations for the TE mode are the following:

$$\frac{\partial^2 E_y}{\partial x^2} + (k_0^2 n^2 - \beta^2)E_y = 0 \tag{3.3a}$$

$$H_x = -\frac{\beta}{\omega\mu_0}E_y \tag{3.3b}$$

$$H_z = -\frac{1}{j\omega\mu_0}\frac{\partial E_y}{\partial x} \tag{3.3c}$$

And the wave equations for the TM mode are:

$$\frac{\partial^2 H_y}{\partial x^2} + (k_0^2 n^2 - \beta^2)H_y = 0 \tag{3.4a}$$

$$E_x = \frac{\beta}{\omega\epsilon_0 n^2}H_y \tag{3.4b}$$

$$E_z = \frac{1}{j\omega\epsilon_0 n^2}\frac{\partial H_y}{\partial x} \tag{3.4c}$$

Limiting ourselves to waves with phase fronts normal to the waveguide axis z, and writing Eq. (3.3a) separately for regions 1, 2 and 3 yields:

$$\frac{\partial^2}{\partial x^2}E(y)+(k_0^2 n_i^2-\beta^2)E(y)=0 \qquad (3.5)$$

where i=1,2,3, which stand for regions 1, 2 and 3, respectively. Before embarking on a formal solution of the above three equations, we may learn a great deal about the physical nature of the solutions by simple arguments. Let us consider the nature of the solutions as a function of the propagation constant $\beta$ at some fixed frequency $\omega$. Assuming that $n_2>n_3 \geq n_1$, for $\beta>k_0 n_2$, i.e., curve a in Fig.3.2 [3.3], it follows directly from Eq.(3.5) that

$$\frac{1}{E}\frac{\partial^2 E}{\partial x^2}>0 \qquad (3.6)$$

everywhere and E(x) is exponential in all three layers of the waveguides. Because of the need to match both E(x) and its derivatives at the interfaces, the resulting field distribution is as shown in Fig.3.2(a). The field increases without bound away from the waveguide so that the solution is not physically realizable and thus does not correspond to a confined wave.

For $k_0 n_3<\beta<k_0 n_2$, as in points b and c, it follows from Eq.(3.5) that the solution is sinusoidal in region 2, since $(1/E)(\partial^2 E/\partial x^2)<0$, but is exponential in regions 1 and 3, which makes it possible to have a solution E(x) that can satisfy the boundary conditions that $H_z$ and $E_y$ must be continuous at x=0 and x=-t while decaying exponentially in regions 1 and 3. These solutions are shown in Fig.3.2(b) and (c). The energy carried by these modes is confined to the vicinity of the guiding layer 2 and we shall, consequently, refer to them as confined or guided modes. Thus we can see that a necessary condition for their existence is that $k_0 n_1$, $k_0 n_3<\beta<k_0 n_2$, i.e., the confined modes are possible only when the inner layer possesses the highest index of refraction.

As illustrated in Fig.3.2(d), solutions of Eq.(3.5) for $k_0 n_1<\beta<k_0 n_3$ (region d) correspond to exponential behaviour in region 1 and to sinusoidal behaviour in region 2 and 3. We shall refer

to these modes as substrate radiation modes. For $0<\beta<k_0n_1$, as in region e, the solution for E(x) becomes sinusoidal in all the three regions. These are the so-called radiation modes of the waveguides, which are not confined to propagate in the guiding layer.

A solution of Eq.(3.5), subject to the boundary conditions at the interfaces, shows that while there is a continuum of allowed $\beta$ values in regions d and e, the allowed $\beta$ values in the propagation regime $k_0n_3<\beta<k_0n_2$ are discrete. At a given wavelength, the number of guided modes increases from 0 with increasing t, the thickness of the inner guide layer. At some t, the $TE_0$ mode becomes confined. Further increases in t will allow $TE_1$ to exist as well, and so on.

Now let us denote the variations or parameters of the cover, guiding layer and substrate with subscription of c, f and s, respectively, which can make their meaning more explicit. So, instead of writing $n_1, n_2$ and $n_3$, we now start to write them as $n_c$, $n_f$ and $n_s$, respectively.
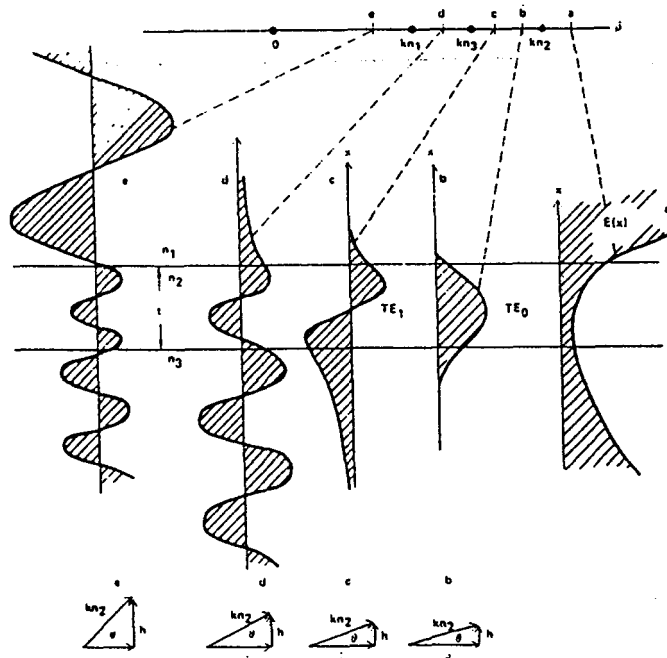


**Figure 3.2**     Propagation constants, electric field distributions, and wave vector diagrams for the different types of waveguide modes: a is not physically realizable; b and c are guided modes; d is a substrate radiation mode; and e is a radiation mode of the waveguide. [after ref.3.3]

The "radiation" modes of this structure, which are not confined to the inner layer, are not treated here. The field solutions of the eigenvalue equations are written in the form:

$$E_y = E_c \exp(-\gamma_c x) \qquad \text{(x>0, in the cover)} \qquad (3.7a)$$

$$E_y = E_f \cos(k_x x + \Phi_c) \qquad \text{(-t<x<0, in the guiding layer)} \qquad (3.7b)$$

$$E_y = E_s \exp[\gamma_s(x+t)] \qquad \text{(x<-t, in the substrate)} \qquad (3.7c)$$

where the propagation constants in the x direction are expressed in the following [3.4]:

$$\gamma_c = k_0\sqrt{N^2 - n_c^2} \qquad\qquad k_x = k_0\sqrt{n_f^2 - N^2} \qquad\qquad \gamma_s = k_0\sqrt{N^2 - n_s^2} \qquad (3.8)$$

where N is the effective index of the guided mode and $N = \beta/k_0$. The boundary condition that the tangential field components $E_y$ and $H_z$ are continuous at the interface x=0 yields

$$E_c = E_f \cos\Phi_c \qquad\qquad (3.9a)$$

$$\tan\Phi_c = \gamma_c/k_x \qquad\qquad (3.9b)$$

Similarly,

$$E_s = E_f \cos(k_x t - \Phi_c) \qquad\qquad (3.10a)$$

$$\tan(k_x t - \Phi_c) = \gamma_s/k_x \qquad\qquad (3.10b)$$

at x=-t. Eliminating arbitrary coefficients in the preceding relations results in an eigenvalue equation

$$k_x t = (m+1)\pi - \tan^{-1}(\frac{k_x}{\gamma_s}) - \tan^{-1}(\frac{k_x}{\gamma_c}) \qquad (3.11)$$

where m=0,1,2... denotes the mode number. When the indices of the waveguide material and the guide thickness t are given, $k_x$ and N can be obtained from Eq.(3.11) and Eq.(3.8). The allowed solutions for N form a discrete set of values in the range of $n_s < N < n_f$ because the mode number is a positive integer.

## 3.3 Beam Propagation Method (BPM)

In transitory, i.e., longitudinally variant, structures the guided modes are usually coupled to the radiation modes and, in consequence, part of the power guided by the waveguide structures is lost. One of the most commonly used methods that takes into account radiation losses is the beam propagation method (BPM) which has been used widely for the analysis of waveguides, couplers, junctions, etc [3.5, 3.6].

In this method, the waveguide cross section is covered with a rectangular mesh of size $\Delta x$ and $\Delta y$ in the x and y directions. At the mesh points, the function E(x,y) is replaced by its discrete values E(x=i$\Delta$x, y=j$\Delta$y). By replacing the partial derivatives by their variational expressions, and assuming $\Delta x = \Delta y$, the field E(x,y) can be written in the following form [3.7]:

$$E(x,y) => E(i,j) = \frac{E(i+1,j) + E(i-1,j) + E(i,j+1) + E(i,j-1)}{4 - k_0^2 \Delta x^2 (n^2(i,j) - n_{eff}^2)} \qquad (3.12)$$

The electric field distribution in the plane z=$z_0$+$\Delta$z, i.e., E(x,y,$z_0$+$\Delta$z), can be calculated from the field distribution in the plane z=$z_0$. Within the assumptions of small $\Delta$z, the field E(x,y,$z_0$+$\Delta$z) is related to E(x,y,$z_0$) by the following relationship [3.7]:

$$E(x,y,z_0+\Delta z)=\exp(-i\Delta z\frac{\nabla_{tr}^2}{(\nabla_{tr}^2+k_0^2)^{1/2}+k_0})E(x,y,z_0)$$ (3.13)

where $\nabla_{tr}$ is the transverse differential operator $(\partial^2/\partial x^2)+(\partial^2/\partial y^2)$. At each iteration, $n_{eff}$ can be estimated from the values of the electric field:

$$\beta^2=k_0^2 n_{eff}^2=\frac{\iint[\frac{\partial^2}{\partial x^2}+\frac{\partial^2}{\partial y^2}+\frac{\partial^2}{\partial z^2}+k_0^2 n^2]E(x,y)E^*(x,y)dxdy}{\iint E(x,y)E^*(x,y)dxdy}$$ (3.14)

where all the integrals are calculated in finite difference form. If the difference between the root mean-square values of the new and old propagation constants fall below a certain value, the electric fields are assumed to have converged.

For numerical simulations, the BPM has been developed into a program which consists of a stepwise propagation of a field through a structure. The method can be used for both three-dimensional and two-dimensional problems. Often a three-dimensional structure is reduces to a two-dimensional problem through the use of effective index method before running the BPM (in two dimensions).

The BPM has a number of important advantages. The algorithm is remarkably simple and numerically stable. High accuracy can be obtained with an adequate choice of the numerical parameter (lateral mesh size, propagation step, etc.). Furthermore, the method can be readily used for nonlinear waveguides and waveguides with loss or gain.

## 3.4 Guided-Wave Transmission Losses and Scatterings

So far, we have explained the various optical modes that can be supported. Following the question as to which modes propagate, the next important characteristic of a waveguide is the attenuation, or loss, that a light wave experiences as it travels through the guide. This loss is generally attributable to three different mechanisms: scattering, absorption and radiation.

Scattering loss usually predominates in glass or dielectric waveguides, while absorption loss is normally most important in semiconductors. Radiation losses become significant when waveguides are bent through a curve.

The loss mechanisms can often be described more conveniently by using the quantum mechanical description, in which the optical field is viewed as a flux of photons. Photons can be either scattered, absorbed or radiated as the optical beam progresses through the waveguide, thus reducing the total power transmitted. When photons are absorbed, they are annihilated by giving up their energy to either the atoms or subatomic particles (usually electrons) of the absorbing material. In contrast, when photons are scattered or radiated, they maintain their identity by changing only their direction of travel, and sometimes their energy (as in Raman scattering). Nevertheless, scattered or radiated photons are removed from the optical beam, thus constituting a loss as far as the total transmitted energy is concerned.

### 3.4.1 Scattering Losses

There are two types of scattering loss in an optical waveguide: volume scattering and surface scattering. Volume scattering is caused by imperfections, such as voids, contaminant atoms and crystalline defects, within the volume of the waveguide. The loss per unit length due to volume scattering is proportional to the number of imperfections (scattering centers) per unit length. Also, the volume scattering loss depends very strongly on the relative size of the imperfections, as compared to the wavelength of light in the material. In all but the crudest of waveguides, volume imperfections are so small compared to wavelength, and so few in number, that the volume scattering loss is negligible compared to surface scattering loss.

In surface scattering loss, "surface" could be the interfaces between guide layer and cladding layer or it could be the cover/air interface. This kind of loss can be significant even for relatively smooth surfaces, particularly in the case of higher-order modes, because the propagating waves interact strongly with the surfaces of the waveguide.

Surface scattering is generally the dominant loss in dielectric film waveguides, such as glasses

and oxides. While in semiconductor waveguides, thickness variations can usually be held to approximately $0.01\,\mu m$ (which is about 1/10 of the surface variation of glasses and oxides), and also, absorption losses are much larger, so that surface scattering is not as important.

## 3.4.2 Absorption Losses

In semiconductors, significant loss occurs because of both interband or band edge absorption and free carrier absorption. In interband absorption, photons with energy greater than the bandgap energy are strongly absorbed in semiconductors by giving up their energy to raise electrons from the valence band to the conduction band. This effect is generally very strong.

Free carrier absorption, sometimes called intraband absorption, occurs when a photon gives up its energy to an electron already in the conduction band, or to a hole in the valence band, thus raising it to higher energy. Usually free carrier absorption is taken to include absorption in which electrons are raised out of shallow donor states near the conduction band edge, or holes are excited into the valence band from shallow acceptor states near the valence band edge.

## 3.4.3 Radiation Losses

Optical energy can be lost from waveguided modes by radiation, in which case photons are emitted into the media surrounding the waveguide and are no longer guided. Radiation can occur from planar waveguides as well as from channel waveguides.

Radiation loss from either planar or straight channel waveguides is generally negligible for well confined modes that are far from cutoff. Since the higher-order modes of a waveguide are always either beyond cutoff or are, at least, closer to cutoff than the lower-order modes, radiation loss is greater for higher-order modes. In an ideal waveguide the modes are orthogonal, so that no energy will be coupled from the lower-order modes to the higher-order modes. However, waveguide irregularities and inhomogeneities can cause mode conversion, so that energy is coupled from lower-order to higher-order modes. In that case, even though a particular mode may be well

confined, it may suffer energy loss through coupling to higher-order modes with subsequent radiation. This problem is not usually encountered in typical waveguides of reasonably good quality, and radiation losses can generally be neglected compared to scattering and absorption losses. The one important exception is the case of curved channel waveguides.

Measurements of the total losses are desirable for improvement of waveguide characteristics, but it is usually difficult to measure the three kind of losses separately. Important information, however, can be obtained from measurements of mode dependence of losses (and angular dependence of scattering), and so on. When losses are larger for higher-order modes, for example, the major loss is due to the scattering at the waveguide surface, while the loss is due to absorption or scattering in the waveguide layer when the loss is mode independent.

## 3.5 Optical Parameters for Our Structure

### 3.5.1 Definition of the Structure

A multi-layer waveguide offers more flexibility for tailoring the loss and adjusting the coupling between the waveguide and absorbing layers than a three-layer waveguide. Fig.3.3 shows the waveguide structure considered in our calculation. The allowed waveguide modes for the structure are obtained by solving the eigenvalue equation for the multi-layer waveguide. The solutions for the propagation constant $\beta$ are complex ($\beta = \beta_r + j\beta_i$), and the power loss coefficient for a waveguide mode is $\alpha = -2\beta_i$. The fraction of the optical power extracted from the waveguide over the interaction length L is approximately $\alpha L$.

### 3.5.2 Bandgap Parameters of the Structure

$Al_xGa_{1-x}As$ bandgap energy at room temperature used in our calculations are obtained according to the following [3.8, 3.9]:

GaAs 0.40μm
20% GaAlAs 0.30μm
15% GaAlAs 0.75μm

20% GaAlAs 2.23μm

GaAs 0.50μm

GaAs

Detector Layer
Confining/Isolation
Layer

Waveguide Layer

Confining Layer

Buffer Layer

Substrate
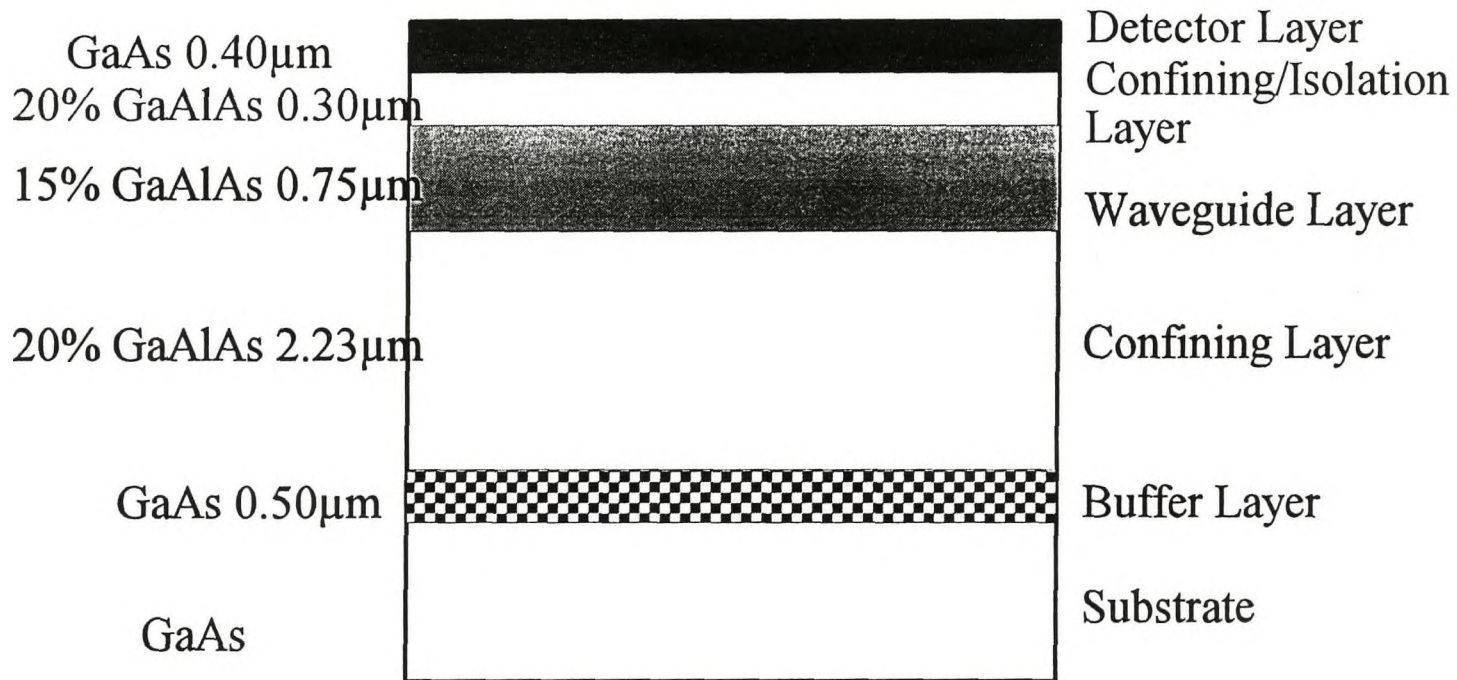
Fig. 3.3 Wafer #94-095 single-mode waveguide/detector structure.

$$E_{gAl_xGa_{1-x}As}=1.424+1.247{\cdot}x \qquad (0{\leq}x{\leq}0.35) \qquad (3.15)$$

where x is the atomic fraction of Al in Al$_x$Ga$_{1-x}$As. Thus the bandgap energy for the waveguide layer where x=0.15 is

$$E_{gAl_{0.15}Ga_{0.85}As}=1.611\,eV, \qquad \lambda_{gAl_{0.15}Ga_{0.85}As}=1.2399/E_g(eV)=0.770\mu m \qquad (3.16)$$

For upper and lower cladding layers, x=0.20,

$$E_{gAl_{0.20}Ga_{0.80}As}=1.673\,eV, \qquad \lambda_{gAl_{0.20}Ga_{0.80}As}=1.2399/E_g(eV)=0.741\mu m \qquad (3.17)$$

For the GaAs detector layer,

$$E_{gGaAs}=1.424\,eV, \quad \lambda_{gGaAs}=0.871\mu m \qquad (3.18)$$

The working wavelength for our device is selected at 820nm at which the waveguide and cladding layers are transparent but the GaAs layer is highly absorbing.

### 3.5.3 Index Calculation

For the optical modelling of the coupling between the waveguide and the detector, knowledge of both real part, n, and the imaginary part, k, of the complex index of refraction is needed. Note that the imaginary portions of the permittivity in the waveguide and upper and lower cladding layers are zero, indicating that they do not absorb light, while the semiconductor detector layer absorbs light and thus has a lossy or complex permittivity.

In this paper, we used the empirically determined Sellmeier equation [3.10] to obtain the refractive indices of GaAs and AlGaAs. For Al$_x$Ga$_{1-x}$As ($\lambda_0$ is in $\mu$m),

$$n^2 = A(x) + \frac{B}{\lambda_0^2 - c(x)} - D(x)\lambda_0^2 \tag{3.19}$$

where x is the atomic fraction of Al atoms in $Al_xGa_{1-x}As$, and parameters A, B, C and D are functions of x which are [3.10]:

| material | A | B | C | D |
|---|---|---|---|---|
| GaAs | 10.906 | 0.97501 | 0.27969 | 0.002467 |
| $Al_xGa_{1-x}As$ | 10.906-2.92x | 0.97501 | $(0.52886-0.735x)^2$ for $x \le 0.36$; $(0.30386-0.105x)^2$ for $x \ge 0.36$. | 0.002467·(1.41x+1) |

In this way, we get the refractive indices of GaAs and AlGaAs for the wavelength of 820nm which are illustrated below:

| $Al_{0.15}Ga_{0.85}As$ | $Al_{0.20}Ga_{0.80}As$ | GaAs |
|---|---|---|
| 3.5252 | 3.4888 | 3.6588 |

The complex refractive index of GaAs can be denoted as

$$\check{n} = n + i\kappa \tag{3.20}$$

where the real part of the refractive index of GaAs has already been obtained as above. Next let us calculate the imaginary part of the index. The complex dielectric function, $\epsilon(\omega) = \epsilon_1(\omega) + i\epsilon_2(\omega)$, can be used to describe the optical properties of the medium. The real and imaginary parts of this dielectric functions are connected by the Kramers-Kronig relations:

$$\varepsilon_1(\omega) = 1 + \frac{2}{\pi} \int_0^\infty \frac{\omega' \varepsilon_2(\omega')}{(\omega')^2 - \omega^2} d\omega' \qquad (3.21a)$$

$$\varepsilon_2(\omega) = -\frac{2}{\pi} \int_0^\infty \frac{\omega' \varepsilon_1(\omega')}{(\omega')^2 - \omega^2} d\omega' \qquad (3.21b)$$

The imaginary part of the dielectric function $[\epsilon_2(\omega)]$ is derived first from the joint density-of-states functions at energies of various critical points in the Brillouin zone [3.11]; then its real part $[\epsilon_1(\omega)]$ is obtained analytically using the Kramers-Kronig relation. The imaginary part of the refractive index $\kappa$ is determined by

$$\kappa(\omega) = \left( \frac{[\epsilon_1(\omega)^2 + \epsilon_2(\omega)^2]^{1/2} - \epsilon_1(\omega)}{2} \right)^{1/2} \qquad (3.22)$$

Alternatively, the absorption coefficient $\alpha(\omega)$ can be determined by [3.11]

$$\alpha(\omega) = \frac{4\pi}{\lambda_0} \left( \frac{[\epsilon_1(\omega)^2 + \epsilon_2(\omega)^2]^{1/2} - \epsilon_1(\omega)}{2} \right)^{1/2} \qquad (3.23a)$$

i.e.,

$$\alpha(\omega) = \frac{4\pi}{\lambda_0} \kappa(\omega) \qquad (3.23b)$$

where $\lambda_0$ is the light wavelength in the vacuum. So, $\kappa(\omega)$ can be deduced directly from experimentally obtained absorption coefficient $\alpha(\omega)$, i.e.,

$$\kappa(\omega) = \frac{\lambda_0}{4\pi} \alpha(\omega) \qquad (3.24)$$

Typical absorption coefficient values for GaAs at a photon energy of 1.5eV (820nm) deduced from transmission data are those of Moss and Hawkins [3.12] ($0.9 \times 10^4 cm^{-1}$), Sturge [3.13] ($1.2 \times 10^4 cm^{-1}$) and Sell et al. [3.14, 3.15] ($1.5 \times 10^4 cm^{-1}$).The value of Sturge has generally been taken as standard [3.16]. So according to Eq.(3.24), at the wavelength 820nm, $\kappa = 0.08$.

In summary, the refractive indices were obtained as:

| $Al_{0.15}Ga_{0.85}As$ | $Al_{0.20}Ga_{0.80}As$ | GaAs |
|---|---|---|
| 3.5252 | 3.4888 | 3.6588+0.08j |

## 3.6 Theoretical Calculations

## 3.6.1 Simulation Results

### 3.6.1.1 Waveguide Structure and Initial Conditions for Simulation

The MSM detectors that were fabricated employed a structure with a 0.3μm thick upper cladding layer and a 0.4μm thick GaAs absorbing layer. The BPM calculations have been performed with a 32×32 grid discretization. Because the index difference between the waveguide and the photodiode could be relatively important, the increment $\Delta z$ should be small enough in order to maintain a sufficient accuracy for the method. We used an increment of 0.02μm in all of our calculations. As the field evolves there is a gradual change in the profile and a decrease in the total optical power due to absorption in the GaAs layer. To model the input coupling between an optical fiber and the passive waveguide, a Gaussian input field distribution was assumed. Then the eigenmode of the passive waveguide was input into the structure with the absorber on.

The optical power can be calculated as a function of z. Fig.3.4 is the profile of the fundamental mode and the power propagation along z direction with the upper cladding layer and absorbing layer thicknesses of 0.3 and 0.4 μm, respectively.

### 3.6.1.2 Simulated Coupling Between Waveguide Layer and Detector Layer

The coupling between the AlGaAs waveguiding layer and the GaAs absorbing layer was modelled using two-dimensional beam propagation method. The calculated waveguide mode's

**(a) Output mode (820nm, d=0.4um)**

**(b) Power attenuation (820nm, d=0.4um)**
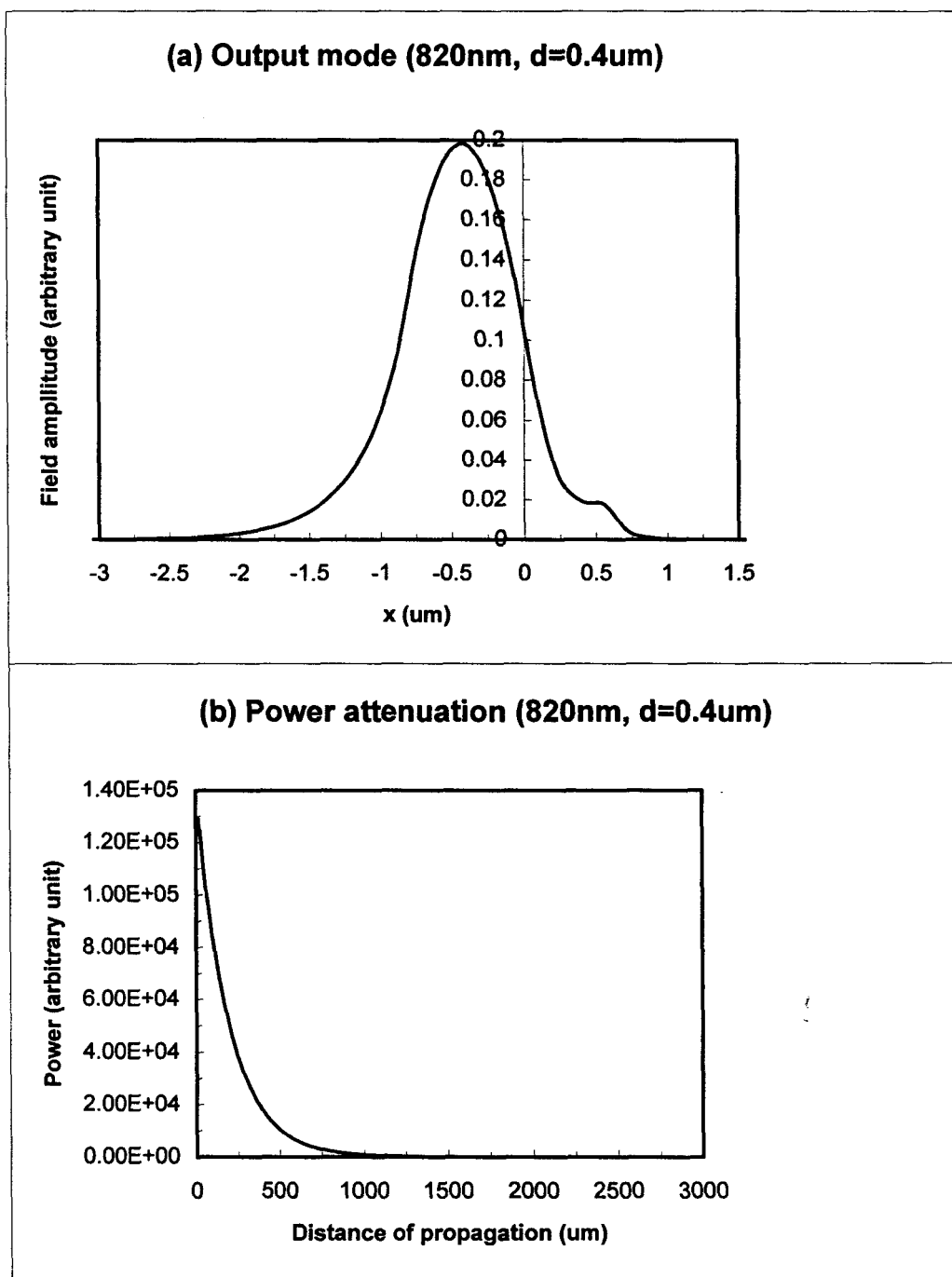
**Figure 3.4**   Profile of the fundamental mode (a) and the power propagation along z direction (b) with the upper cladding layer and absorbing layer thickness of 0.3 and 0.4μm, respectively. (x is defined the same as in Figure 3.1, for the thicknesses of different layers.)

attenuation coefficient's dependence on the thickness of the absorbing layer is complicated (Fig.3.5). As the absorbing layer thickness is increased, holding the upper cladding layer constant at 0.3μm, the attenuation increases from zero to a maximum value of 215.6cm$^{-1}$ at a GaAs thickness of 0.2μm. Increasing the GaAs layer thickness further causes the attenuation to drop to a local minimum of 81cm$^{-1}$ at a thickness of 0.4μm and then to oscillate with decreasing amplitude toward a constant value of 110cm$^{-1}$.

The reason why the attenuation is constant for GaAs thicknesses above about 1μm is that the propagating mode penetrates less than one μm into the absorbing layer. For thin absorbing layers, however, the oscillatory behaviour is due to an enhancement in the coupling between the waveguiding and absorbing layers that occurs when the multilayer detector structure has a higher order transverse mode that is near the cutoff condition. For the two thicknesses 0.2 and 0.6μm, the waveguide is just slightly above cutoff for the second and third slab waveguide modes, respectively. Large portions of the energy in the guided lightwave couple from the waveguide into the absorptive layer. The attenuation is then correspondingly high.

Similar theoretical predictions have been reported for an InGaAs p-i-n photodiode structure integrated with an InGaAsP waveguide [3.17].

### 3.6.1.3 The Effect of Thickness of Upper Cladding Layer on the Absorption Coefficient

The attenuation coefficient in the detector is also naturally dependent on the thickness of the upper cladding layer. Results of the calculated attenuation coefficients' dependence on the thickness of the absorber layer while taking the upper cladding layer thickness as a parameter are collected in Fig.3.6. For each calculated curve, the eigenmode used the input field was recalculated to be appropriate for the modified passive waveguide.

This figure shows that the oscillatory behaviour of the absorption coefficient's dependence on the thickness of the absorption layer exists for various thicknesses of the upper cladding layer. The attenuation coefficient in the detector segment was found to decrease monotonically as the cladding layer thickness increased if the absorption layer is thinner than ~0.14μm due to reduced
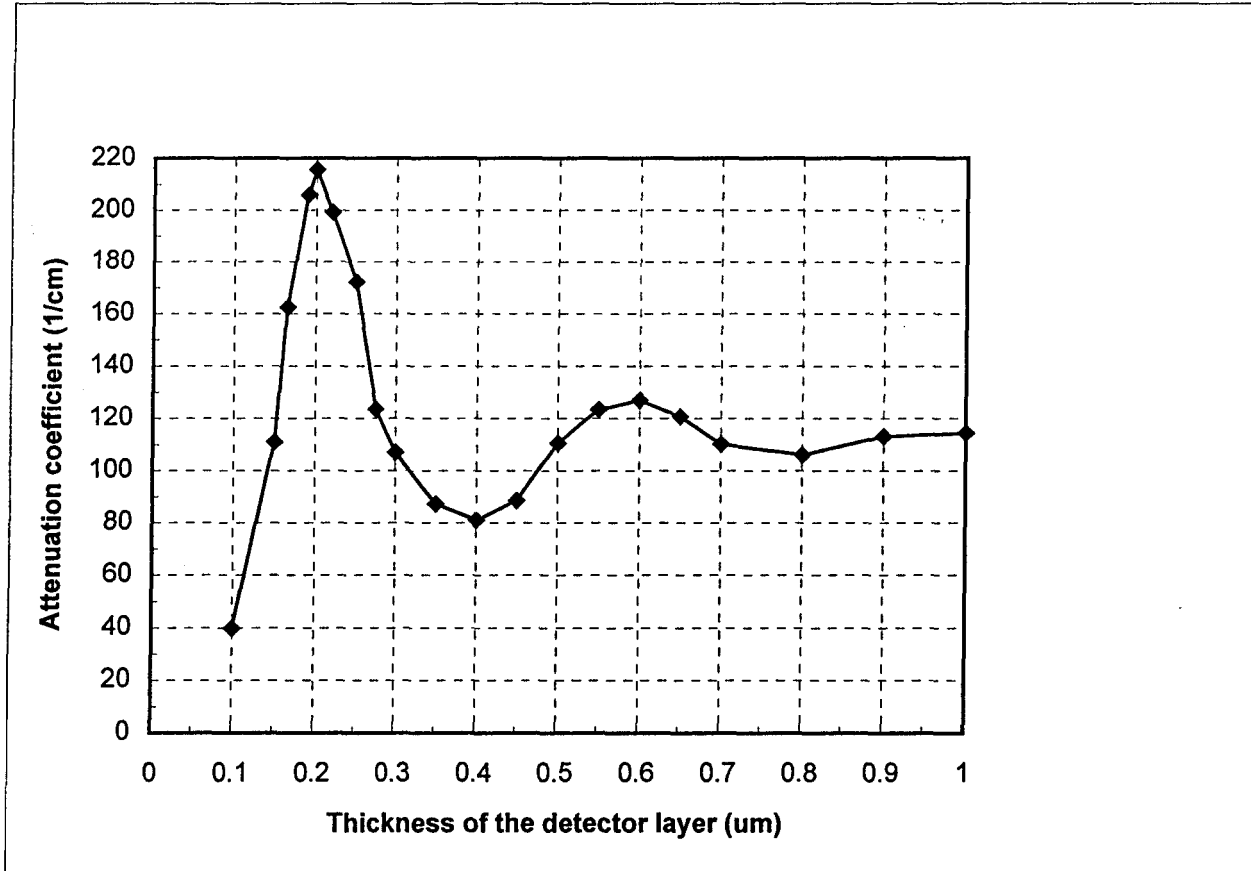
Figure 3.5 Calculated attenuation coefficient of the detector section as a function of the GaAs absorbing layer thickness. Waveguide layer and upper cladding layer are 0.75 and 0.3μm thick, respectively. The wavelength is 820nm.

light power carried in the region above this layer as the thickness of the upper cladding layer increases; while if the absorber layer is thicker than ~0.14 μm, the behavior is complex. The coupling strength depends on both the thickness of the detector layer and the upper cladding layer.

### 3.6.2 Theoretical Explanation for the Predicted Enhanced Coupling

To explain the enhanced coupling near cutoff of the modes, we write the field distribution in the detector section as:

$$E(x,z,t) = \sum_m a_m E_m(x) e^{j(\beta_m z - \omega t)} \qquad (3.25)$$

$E_m$ is an eigenmode of the waveguide detector and $\beta_m$ is its propagation constant. The coefficients
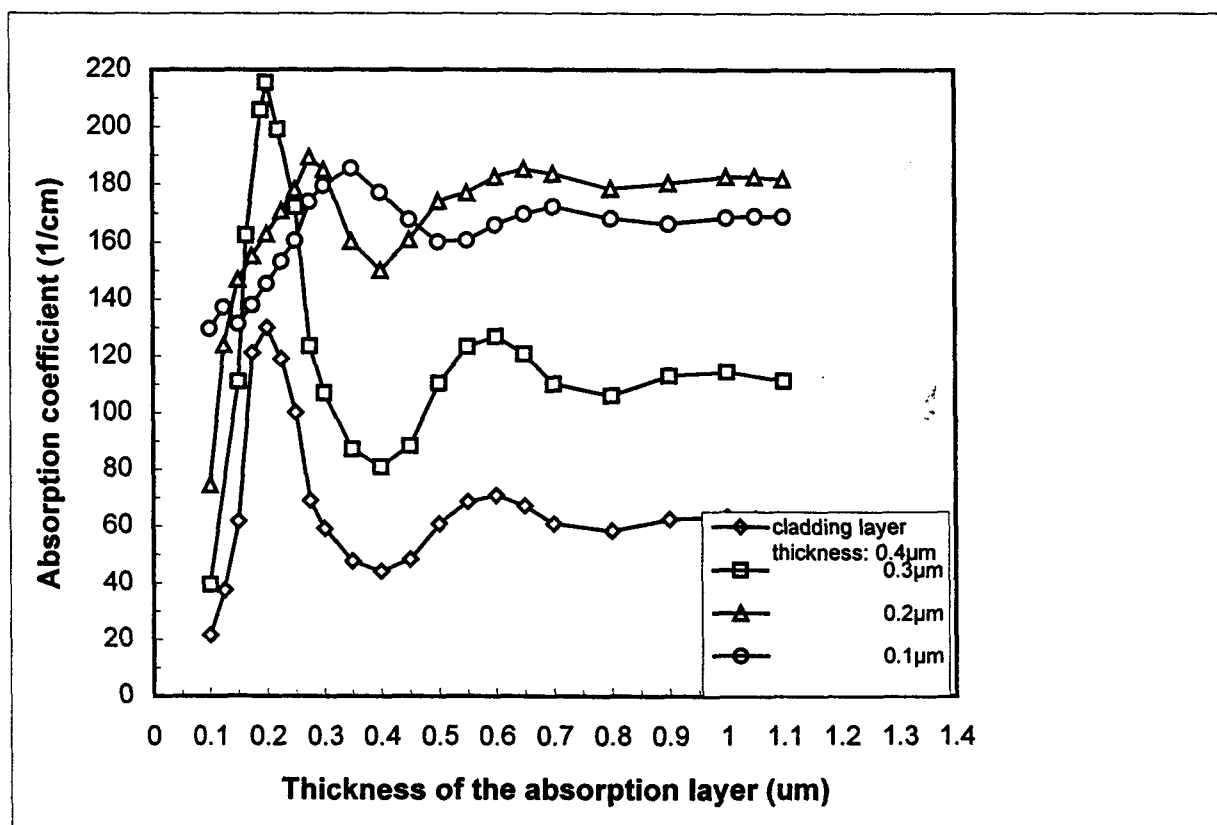


**Figure 3.6** Absorption coefficient vs. the thickness of the absorption layer with different cladding layer thicknesses.

$a_m$ are calculated as overlap integrals between the input field and the modes, $E_m$ [3.18]. This equation can offer a qualitative explanation for the enhanced absorption near cutoff of one of the low order eigenmodes. For the structure shown in Fig.3.3 with the upper cladding layer and the absorber layer having thicknesses 0.3 and 0.4 μm, respectively, the detector section supports two bound waveguide modes, $E_0$ and $E_1$. Their effective indices, as calculated using the transfer matrix approach, are 3.510+0.000526j and 3.583+0.0730j, respectively. The calculated mode profiles are shown in Fig.3.7(a) [3.18]. The field distribution, $E_1$, has a single lobe that is confined primarily to the high index GaAs absorbing layer and, as a result, its overlap with the input field ($a_1$ in Eq.(3.25)) is very small. The field distribution, $E_0$, has a dominant lobe in the 0.75μm thick $Al_{0.15}Ga_{0.85}As$ layer and only a modest penetration into the GaAs absorbing layer. It has a much larger overlap coefficient, $a_0$. The ratio of the coefficients is $|a_1|/|a_0|$=0.0002. $|a_1|$ is so much smaller than $|a_0|$ that $E_1$ makes a negligible contribution to the summation in Eq.(3.25).

If the thickness of the GaAs absorbing layer is reduced from 0.4 to 0.2 μm, the waveguide is still double mode. However, $E_1$ is very near cutoff. In this case the two modes have effective indices of 3.510+0.00162j and 3.93 +0.0406j for $E_0$ and $E_1$, respectively. The calculated mode profiles for this case are shown in Fig.3.7(b). Near cutoff both modes make significant contributions to the summation in Eq.(3.25) ($|a_1|/|a_0|$=0.052) and the attenuation coefficient becomes correspondingly high.

## 3.7 Experimental Measurement of the Absorption Coefficient:

### 3.7.1 Measuring Scheme

We conducted an experiment to confirm the theoretical prediction of the oscillatory dependence of the absorption coefficient on the thickness of the absorber. As far as we know, there has not been any other experimental confirmation of this oscillatory relation. A couple of schemes were designed for the measurement:
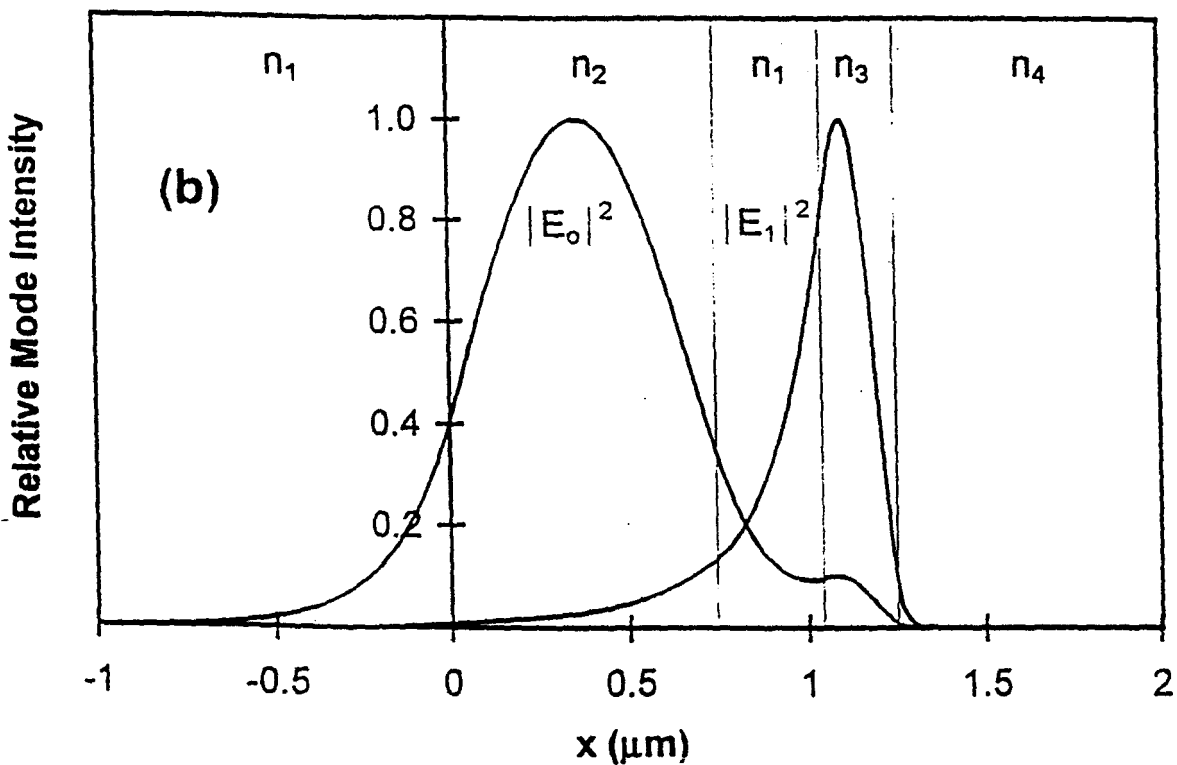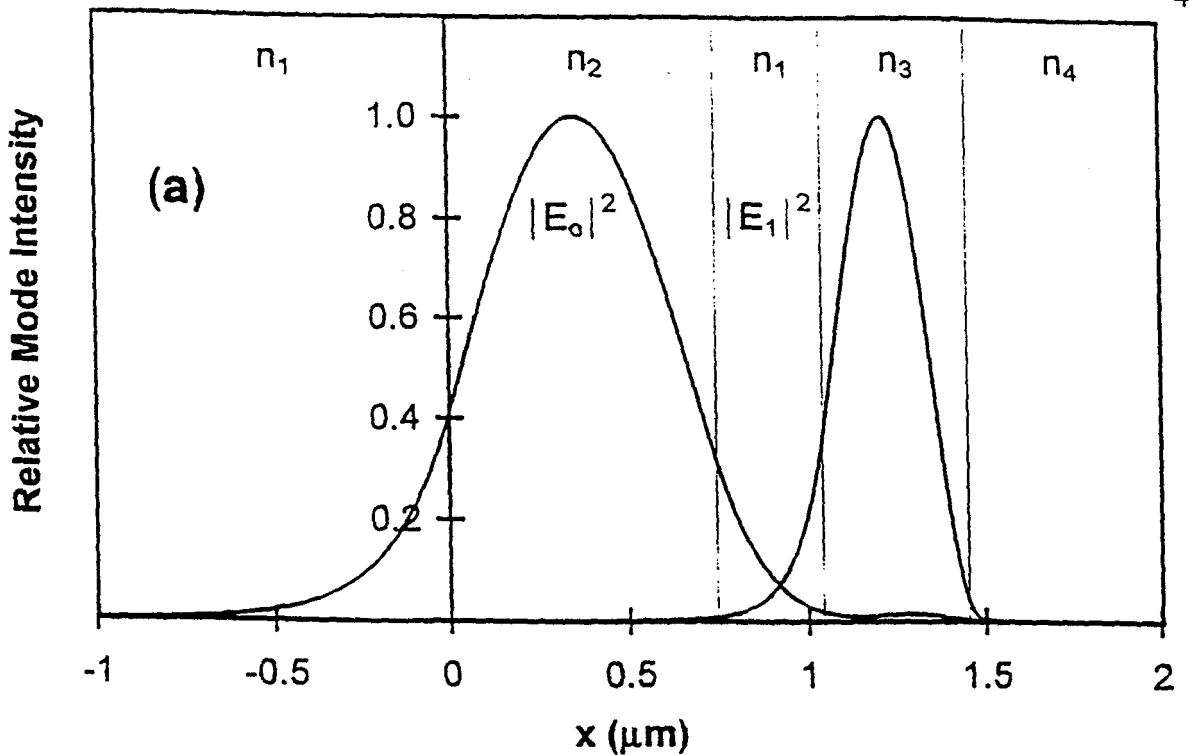
**Figure 3.7** Calculated mode intensity profiles for detector section with GaAs absorber thicknesses of (a) 0.4μm and (b) 0.2μm. The calculation assumed a wavelength of 820nm and refractive index values of $n_1$=3.4888, $n_2$=3.5252, $n_3$=3.6588-0.08i and $n_4$=1.0.

Scheme 1  Cut-Back Method:

A simple method for direct measurement of transmission losses is to compare the transmittances of waveguides having different lengths. A guided wave is excited by end-coupling and the transmitted-light intensity is measured. Then, the transmittance is measured again after the waveguide is shortened. This is the well-known cut-back method. Transmission losses are:

$$\alpha = |10\log(P_1/P_2)/(L_1 - L_2)| \, [dB/cm] \tag{3.26}$$

where $L_1$, $L_2$ [cm] and $P_1$, $P_2$ are the lengths and transmittances before and after cutting, respectively. High-quality waveguide edges must be prepared so that equal input and output coupling efficiencies may be reproduced for each measurement. This method has the advantage that relatively accurate measurement is possible with a simple configuration. One drawback of this scheme is that it is a destructive method. The sample is cut after each measurement . Another drawback is that in our experiment, a lot of measurements have to be conducted for different absorber thicknesses. Cutting the samples after each measurement will require tremendous work, which is not be favored.

Scheme 2  Transmission-Lateral-Comparison Method

In this scheme, the sample was patterned as Fig.3.8 where one guide has GaAs completely etched off while the guide next to it has a GaAs layer of thickness d. The absorption coefficient in the detector material (where the upper GaAs was not removed) was determined by coupling a beam of light from a diode laser of $\lambda$=820nm into the AlGaAs waveguide layer and measuring the transmitted power. This was compared to the transmitted power when the sample was translated laterally, as illustrated in Fig.3.8, so that the same laser beam was coupled into the same waveguide in a passive region where the absorbing layer was removed.  It is assumed that the input coupling efficiency and the reflection coefficiency of the adjacent regions are the same.

It is known from previous measurements that the propagation losses in the passive region is
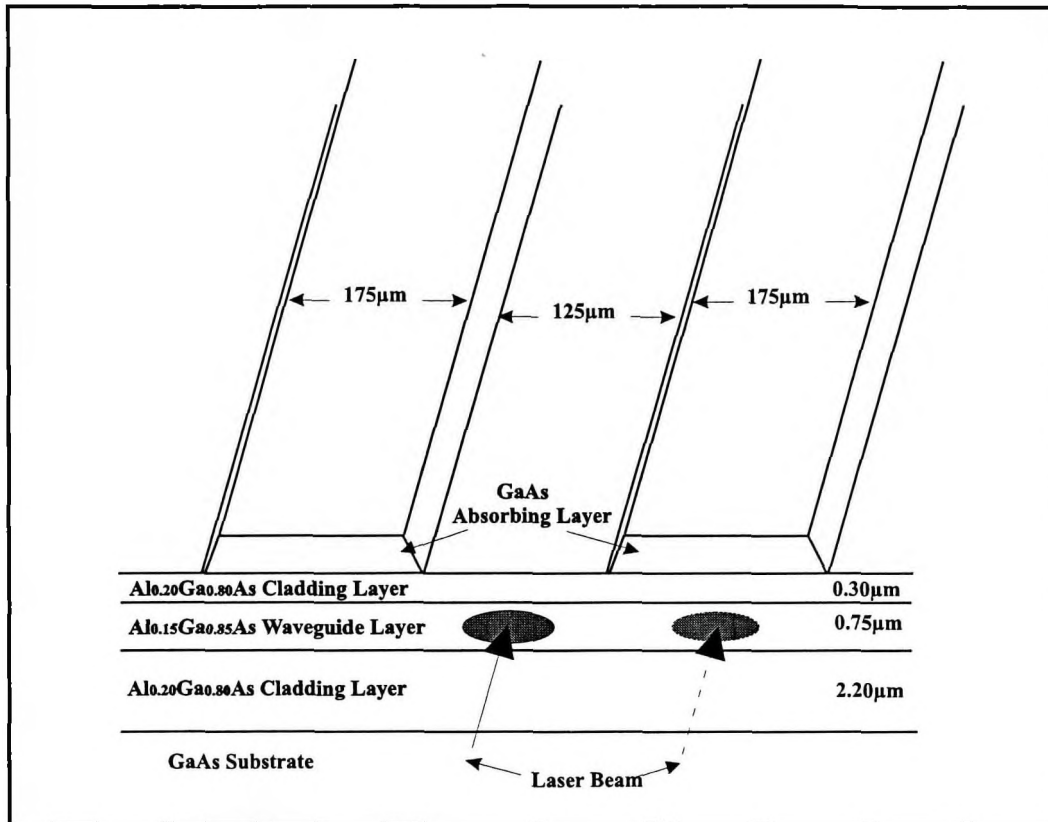
**Figure 3.8** Waveguide structure for measuring the attenuation coefficient in the detector section by comparing the transmissions between two adjacent guides. One guide has GaAs completely etched off, while the one adjacent to it has GaAs layer of thickness d.

below 2dB/cm [3.18], which is negligible compared to the absorbing region. The absorption coefficient in the absorbing region which is denoted as $\alpha$ is determined by taking the ratio of the measured transmission of the two guides to be exp(-$\alpha$L), where L is the sample length. We chose this scheme in our experiment to measure the absorption coefficients at different thickness of the absorber layer.

### 3.7.2 Sample Processing

For the present work, a new structure with a 0.8µm-thick GaAs layer was used (Fig.3.9) which

was grown in CRC. A selective chemical etch [3.19] was used to remove completely the GaAs layer in a series of 175-μm-wide parallel straight lines, separated by 125-μm-wide GaAs ridges. The etchant was superoxol (30% $H_2O_2$) with a pH value increased to 7.0±0.1 by the addition of a small quantity of Ammonium Hydroxide ($NH_4OH$).

When the pH of superoxol is varied in the range 1-6 by the addition of $NH_4OH$, the solution can be used to grow an oxide onto GaAs (or AlGaAs). As the pH is increased beyond 6, the solution becomes an etchant for GaAs while the adjacent $Al_xGa_{1-x}As$ layers show no apparent attack (for $x \geq 0.1$). The GaAs surface roughness increased with pH until at pH~8 the surface was very badly pitted [3.19]. So during the processing of the sample, the pH value of the etchant is controlled at 7.0±0.1.

The crystal etches by the growth of a surface oxide film that cracks into small segments that float away from the surface, permitting new oxide sheets to form. To assist the stripping of the
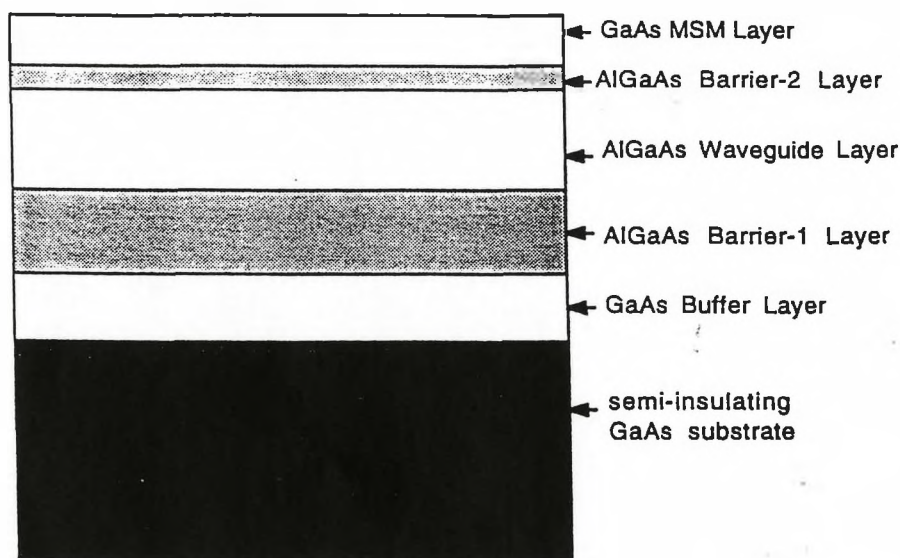


| Run No | Buffer | Barrier-1 | Waveguide | Barrier-2 | MSM |
|--------|--------|-----------|-----------|-----------|-----|
| 96-048 | t=0.50 um | t=2.20 um | t=0.75 um | t=0.30 um | t=0.80 um |

**Figure 3.9** GaAs-AlGaAs heterostructure MSM/waveguides for the measurement of the attenuation coefficient in the detector section.

oxide layers from the surface, we used an agitated bath. That is, the sample was held near the periphery of a 2-in.-diameter quartz beaker of etchant, which was placed on a hot plate that was used as a stirring plate. A magnetic bar of proper length (~1.5inch) was placed at the bottom of the beaker. The stirrer's rotating speed was set at 400RPM.

At pH of 7.0±0.1 and 22°C for the etchant, the etching depth in the agitated bath is approximately linear in time which is shown in Fig.3.10. The etching rate is about 0.089 μm/min.

In patterning the sample, we used a mask with parallel "strips" with width of 125μm and 175μm between each other. We did the photolithography on the whole piece of sample and developed it, leaving photoresist on the unexposed sections. At the exposed sections, GaAs was selectively etched all the way down to AlGaAs, by which the passive regions were defined. Then
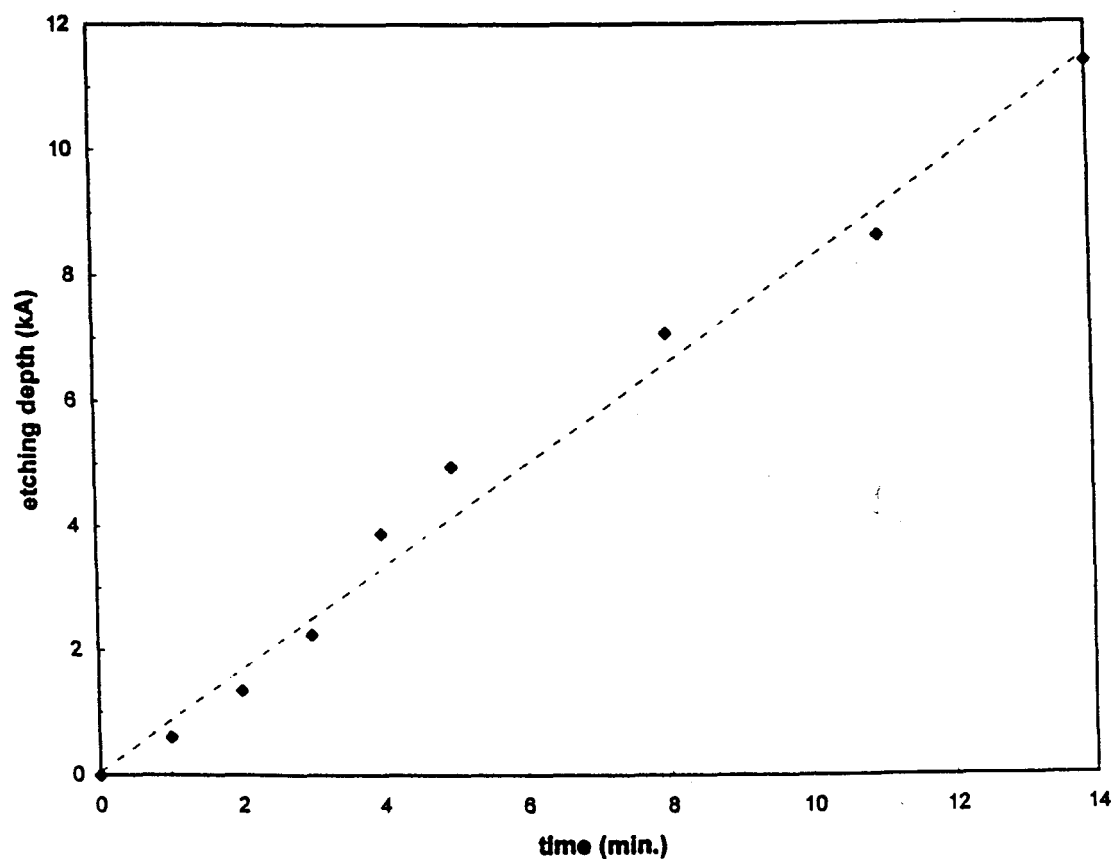


**Figure 3.10**    Distance etched into a GaAs surface against time of etching in superoxol etchant with pH=7.0±1.0 with agitation speed at 400rpm at 22°C.

the remaining photoresist was removed to expose the GaAs surface. The material was cleaved into a large number of small pieces of $3 \times 5mm^2$. Each piece was then exposed to the same selective etch for different time to get different thicknesses for the GaAs layer while negligible distance was etched in the passive regions . The final thickness of the GaAs ridge was measured for each piece using a surface profiler. Fig.3.11 are some of the pictures of the profiles of the etched guides. After the final etch each piece was then cleaved to a length of L=0.25 or L=0.5mm for the transmission measurements. The samples thus obtained are listed in Table 3.1 with their respective lengths and thicknesses of the absorbing layer. Fig.3.12 are typical scanning electron microscopes of the samples which show the clear edges and surfaces after etching.

The stripes of the sample, or widths of the passive (non-absorbing) and active (absorbing) regions were sufficiently wide so that, when light was coupled into the waveguide near the stripe centre, the waveguide acted as a slab, rather than a rib, waveguide.

## 3.7.3 Experimental Measurements

The experimental set-up uses a standard method of measuring the transmission of the sample (Fig.3.13). Light coming out of the diode laser is coupled into the fiber, and then is coupled into the waveguide from the tapered end of the fiber. A lens of numerical aperture 0.40 was employed to collect the radiation from the exit facet of the sample. All the guides were tested with the same lens arrangement in order to maintain a fixed input and output coupling efficiency. The leakage light from the input and output ends can be removed by inserting a spatial filter (an aperture) in front of the photodetector.

We measured the transmission from each guide, calculated the attenuation coefficient from the transmissions of each pair of adjacent guides, and then averaged the attenuation coefficients obtained for the GaAs detector layer of the same thickness, respectively. The results are listed in Table 3.2. The thus obtained average absorption coefficients with standard deviation are shown in Fig.3.14 together with the theoretical calculations as a function of the thickness of the GaAs absorbing layer.
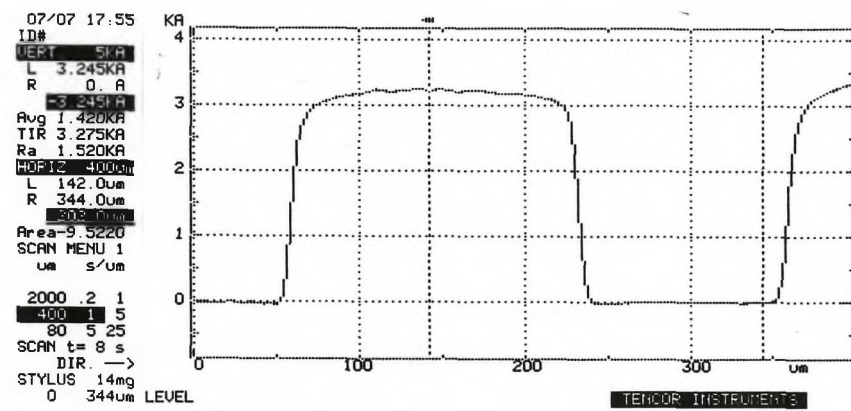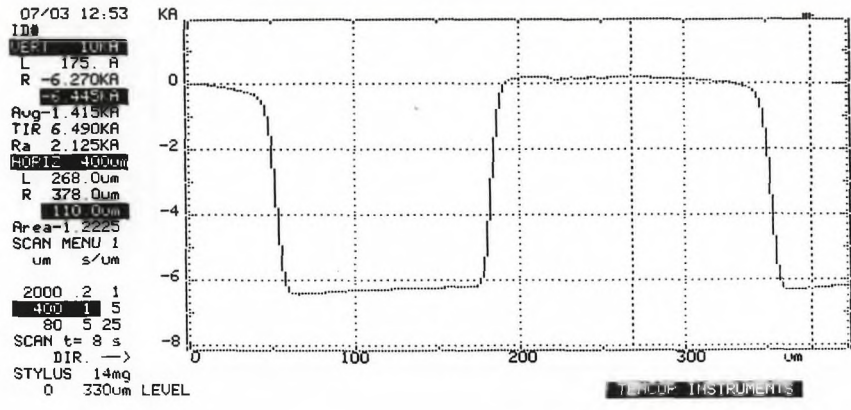
**Figure 3.11**  Profiles of the etched guides measured with a surface profiler.
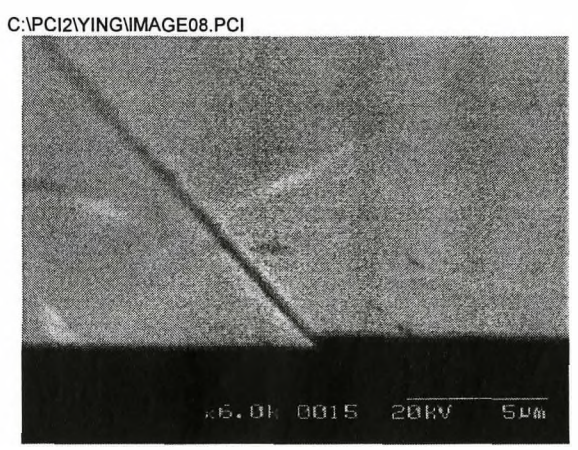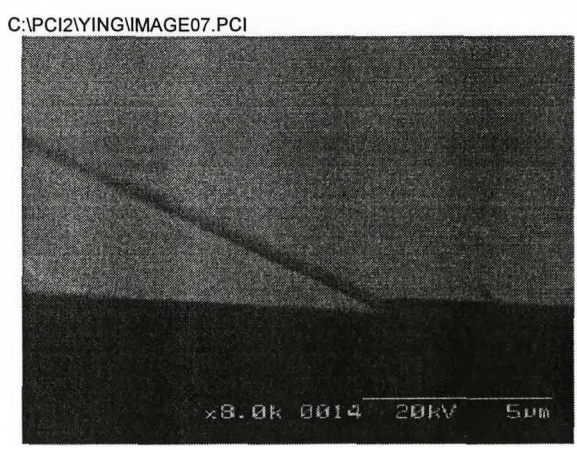


**Figure 3.12**  Typical scanning electron microscope pictures of the etched samples.

## Table 3.1  Samples with Different Etching Thicknesses

| Sample # | Measured Thicknesses at Different Points of the Samples (nm) | | | | | | | | | | | Average Thickness to (nm) | Max-to (nm) | to-Min (nm) | (Max-to)/to % | (to-Min)/to % |
|---|---|---|---|---|---|---|---|---|---|---|---|---|---|---|---|---|
| 2 | 665 | 655 | 645 | 630 | 655 | 625 | 640 | | | | | 645.0 | 20.0 | 20.0 | 3.10 | 3.10 |
| 3 | 775 | 790 | 785 | 780 | 820 | 775 | 770 | 775 | 795 | 770 | 805 | 785.5 | 34.5 | 15.5 | 4.40 | 1.97 |
| 4 | 390 | 385 | 360 | 350 | 395 | 405 | 405 | 410 | | | | 387.5 | 22.5 | 37.5 | 5.81 | 9.68 |
| 5 | 520 | 535 | 525 | 560 | 560 | 565 | 560 | | | | | 546.4 | 18.6 | 26.4 | 3.40 | 4.84 |
| 6 | 500 | 490 | 465 | 470 | 475 | 480 | 510 | 495 | 505 | 495 | 510 | 490.5 | 19.5 | 25.5 | 3.99 | 5.19 |
| 7 | 320 | 325 | 330 | 345 | 350 | 360 | 350 | 335 | 350 | 335 | | 340.0 | 20.0 | 20.0 | 5.88 | 5.88 |
| 8 | 410 | 430 | 420 | 410 | 400 | 410 | 430 | 420 | 410 | | | 415.6 | 14.4 | 15.6 | 3.48 | 3.74 |
| 10 | 465 | 440 | 460 | 460 | 420 | 440 | | | | | | 447.5 | 17.5 | 27.5 | 3.91 | 6.15 |
| 11 | 335 | 380 | 375 | 360 | 370 | 365 | 345 | 365 | 365 | 375 | 375 | 364.5 | 15.5 | 29.5 | 4.24 | 8.10 |
| 12 | 315 | 290 | 295 | 295 | 310 | 270 | | | | | | 295.8 | 19.2 | 25.8 | 6.48 | 8.73 |
| 13 | 285 | 290 | 300 | 270 | 285 | 275 | 285 | | | | | 284.3 | 15.7 | 14.3 | 5.53 | 5.03 |
| 14 | 285 | 260 | 250 | | | | | | | | | 265.0 | 20.0 | 15.0 | 7.55 | 5.66 |
| 15 | 250 | 245 | 280 | 290 | 270 | 250 | 220 | 245 | | | | 256.3 | 33.8 | 36.3 | 13.17 | 14.15 |
| 16 | 335 | 285 | 355 | 370 | | | | | | | | 336.3 | 33.8 | 51.3 | 10.04 | 15.24 |
| 18 | 185 | 180 | 170 | 160 | 180 | 185 | 160 | | | | | 174.3 | 10.7 | 14.3 | 6.15 | 8.20 |
| 19 | 145 | 135 | 170 | 110 | 175 | 110 | 175 | 125 | | | | 143.1 | 31.9 | 33.1 | 22.27 | 23.14 |
| 21 | 110 | 125 | 115 | 95 | | | | | | | | 111.3 | 13.8 | 16.3 | 12.36 | 14.61 |
| 22 | 190 | 230 | 210 | 270 | 225 | 240 | | | | | | 227.5 | 42.5 | 37.5 | 18.68 | 16.48 |
| 23 | 185 | 195 | 235 | 225 | 190 | 170 | | | | | | 200.0 | 35.0 | 30.0 | 17.50 | 15.00 |
| 31 | 739 | 765 | 700 | 734 | 742 | 729 | 730 | | | | | 734.1 | 30.9 | 34.1 | 4.20 | 4.65 |
| 32 | 560 | 569 | 577 | 568 | 566 | 560 | | | | | | 566.7 | 10.3 | 6.7 | 1.82 | 1.18 |
| 37 | 299 | 279 | 288 | 314 | 294 | 289 | 298 | | | | | 294.4 | 19.6 | 15.4 | 6.65 | 5.24 |
| 40 | 130 | 151 | 146 | 142 | 149 | 138 | 131 | 130 | 135 | 133 | | 138.5 | 12.5 | 8.5 | 9.03 | 6.14 |
| 41 | 217 | 236 | 188 | 186 | 217 | 229 | 244 | 215 | 212 | 208 | | 215.2 | 28.8 | 29.2 | 13.38 | 13.57 |
| 42 | 286 | 284 | 283 | 288 | 283 | 284 | 302 | 308 | | | | 289.8 | 18.3 | 6.8 | 6.30 | 2.33 |
| 43 | 244 | 219 | 250 | 256 | 262 | 249 | 245 | 246 | | | | 246.4 | 15.6 | 27.4 | 6.34 | 11.11 |
| 46 | 224 | 220 | 227 | 208 | 218 | 242 | 220 | | | | | 222.7 | 19.3 | 14.7 | 8.66 | 6.61 |
| 48 | 60 | 63 | 64 | 62 | 63 | 58 | 65 | | | | | 62.1 | 2.9 | 4.1 | 4.60 | 6.67 |
| 49 | 128 | 125 | 128 | 129 | 131 | | | | | | | 128.2 | 2.8 | 3.2 | 2.18 | 2.50 |
| 52 | 189 | 208 | 191 | 197 | 190 | 192 | 188 | | | | | 193.6 | 14.4 | 5.6 | 7.45 | 2.88 |
| 53 | 193 | 183 | 171 | 175 | 177 | 180 | 172 | 170 | | | | 177.6 | 15.4 | 7.6 | 8.66 | 4.29 |
| 54 | 590 | 603 | 605 | 589 | 597 | 595 | 602 | | | | | 597.3 | 7.7 | 8.3 | 1.29 | 1.39 |
| 55 | 287 | 255 | 256 | 246 | 281 | 278 | 277 | | | | | 268.6 | 18.4 | 22.6 | 6.86 | 8.40 |
| 56 | 225 | 242 | 233 | 240 | 218 | | | | | | | 231.6 | 10.4 | 13.6 | 4.49 | 5.87 |
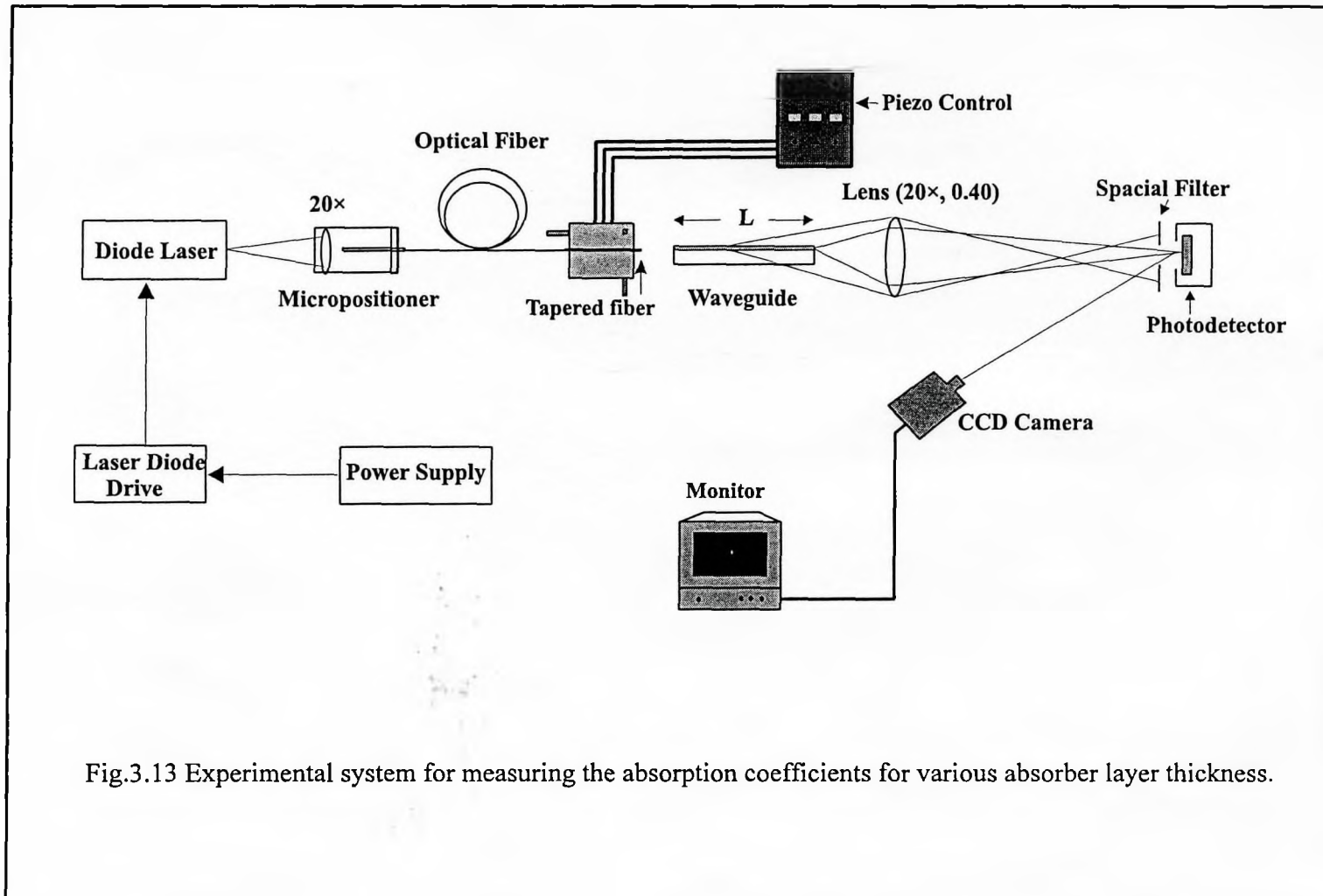
Fig.3.13 Experimental system for measuring the absorption coefficients for various absorber layer thickness.

# Table 3.2  Experimental Measurement of the Absorption Coefficients with Different Absorption Layer Thicknesses

| Samples | Channels | 1 | 2 | 1 | 2 | 1 | 2 | 1 | 2 | 1 | 2 | 1 | 2 | 1 | 2 | 1 | 2 | 1 | 2 | Average alpha α0 (1/cm) | (Max-α0)/α0 % | (α0-Min)/α0 % |
|---|---|---|---|---|---|---|---|---|---|---|---|---|---|---|---|---|---|---|---|---|---|---|
| #2 | transmission (μW) | 98.5 | 0.391 | 87.9 | 0.328 | 101.4 | 0.468 | 98.7 | 0.258 | | | | | | | | | | | | | |
| l=0.5mm | alpha (1/cm) | 110.6 | 108.3 | 111.8 | 114.7 | 107.6 | 107.0 | 118.9 | | | | | | | | | | | | 111.3 | 6.89 | 3.82 |
| #3 | transmission (μW) | 105.1 | 0.692 | 94.7 | 1.28 | 114.3 | 1.14 | 84.0 | 1.01 | 101.3 | | | | | | | | | | | | |
| l=0.5mm | alpha (1/cm) | 100.5 | 98.4 | 86.1 | 89.8 | 92.2 | 86.0 | 88.4 | 92.2 | | | | | | | | | | | 91.7 | 9.57 | 6.21 |
| #4 | transmission (μW) | 33.8 | 0.518 | 29.9 | ... | 33.3 | 1.08 | 35.2 | 1.09 | | | | | | | | | | | | | |
| l=0.5mm | alpha (1/cm) | 83.6 | 81.1 | | | 68.6 | 69.7 | 69.5 | | | | | | | | | | | | 74.5 | 12.19 | 7.94 |
| #5 | transmission (μW) | | 1.1 | 25.4 | 1.66 | 35.3 | 0.324 | 43.6 | 0.882 | 38.7 | 0.243 | ... | 1.45 | 72.4 | | | | | | | | |
| | l (mm) | | 0.25 | | 0.35 | 0.4 | 0.4 | 0.45 | 0.5 | | | | | | | | | | | | | |
| | alpha (1/cm) | | 125.6 | 109.1 | | 134.0 | 122.6 | 97.5 | 94.5 | 101.4 | | | 78.2 | | | | | | | 107.9 | 24.25 | 27.49 |
| #6 | transmission (μW) | 77.6 | 5.17 | ... | 8.18 | 88.8 | 9.14 | 90.8 | 10.54 | | | | | | | | | | | | | |
| l=0.25mm | alpha (1/cm) | 108.3 | | 95.4 | 90.9 | 91.8 | 86.1 | | | | | | | | | | | | | 94.5 | 14.61 | 8.88 |
| #7 | transmission (μW) | | 5.44 | 49.7 | 8.99 | ... | 8.04 | 41.7 | 8.59 | 37.5 | 2.29 | 41.7 | 3.77 | 36.4 | 5.64 | 28.0 | 1.86 | | | | | |
| l=0.25mm | alpha (1/cm) | | 88.5 | 68.4 | | 65.8 | 63.2 | 58.9 | 111.8 | 116.1 | 96.1 | 90.7 | 74.6 | 64.1 | 108.5 | | | | | 83.9 | 38.36 | 29.74 |
| #8 | transmission (μW) | 41.3 | 6.67 | 56.7 | 7.1 | 54.1 | 5.9 | 41.7 | 6.66 | 59.2 | 6.83 | 53.8 | 6.75 | 52.8 | 5.91 | | | | | | | |
| l=0.25mm | alpha (1/cm) | 72.9 | 85.6 | 83.1 | 81.2 | 88.6 | 78.2 | 73.4 | 87.4 | 86.4 | 82.6 | 83.0 | 82.3 | 87.6 | | | | | | 82.5 | 7.45 | 11.59 |
| #10 | transmission (μW) | | 4.35 | 52.5 | 5.52 | 51.7 | 6.36 | 48.6 | 6.64 | 53.7 | 6.61 | 53.0 | 5.25 | | | | | | | | | |
| l=0.25mm | alpha (1/cm) | | 99.6 | 90.1 | 89.5 | 83.8 | 81.3 | 79.6 | 83.6 | 83.8 | 83.3 | 92.5 | | | | | | | | 86.7 | 14.89 | 8.18 |
| #11 | transmission (μW) | 71.2 | 4.86 | ... | 6.09 | 62.4 | 6.63 | 47.4 | 8.67 | 46.0 | 7.52 | | | | | | | | | | | |
| l=0.25mm | alpha (1/cm) | 107.4 | | 93.1 | 89.7 | 78.7 | 68.0 | 66.8 | 72.4 | | | | | | | | | | | 82.3 | 30.50 | 18.87 |
| #12 | transmission (μW) | 39.7 | 4.88 | ... | 5.33 | 47.2 | 7.53 | 61.2 | 4.79 | 54.5 | 3.43 | 55.5 | 5.89 | 45.9 | 7.48 | | | | | | | |
| l=0.25mm | alpha (1/cm) | 83.8 | | 87.2 | 73.4 | 83.8 | 101.9 | 97.3 | 110.6 | 111.4 | 89.7 | 82.1 | 72.6 | | | | | | | 90.4 | 23.24 | 19.68 |
| #13 | transmission (μW) | 56.8 | 2.93 | 58.9 | 4.94 | 54.5 | 5.51 | 57.8 | 5.33 | | | | | | | | | | | | | |
| l=0.25mm | alpha (1/cm) | 118.6 | 120.0 | 99.1 | 96.0 | 91.7 | 94.0 | 95.3 | | | | | | | | | | | | 102.1 | 17.55 | 10.23 |
| #14 | transmission (μW) | 78 | 4.13 | 79.2 | 4.53 | 59.7 | 3.19 | 59.0 | ... | 63.4 | | | | | | | | | | | | |
| l=0.25mm | alpha (1/cm) | 117.5 | 118.1 | 114.5 | 103.1 | 117.2 | 116.7 | | | | | | | | | | | | | 114.5 | 3.16 | 9.94 |
| #15 | transmission (μW) | 43.7 | 3.94 | 31.2 | 3.07 | 36.6 | 3.59 | 35.7 | 5.73 | 40.9 | | | | | | | | | | | | |
| l=0.25mm | alpha (1/cm) | 96.2 | 82.8 | 92.7 | 99.1 | 92.9 | 91.9 | 73.2 | 78.6 | | | | | | | | | | | 88.4 | 12.10 | 17.25 |
| #16 | transmission (μW) | 65.5 | 5.95 | 56.9 | 5.69 | 60.8 | 3.93 | ... | 5.83 | 51.5 | 3.85 | 39.7 | 3.13 | 27.9 | 2.58 | 59.0 | 3.32 | | | | | |
| l=0.25mm | alpha (1/cm) | 95.9 | 90.3 | 92.1 | 94.8 | 109.6 | | 87.1 | 103.7 | 93.3 | 101.6 | 87.5 | 95.2 | 125.2 | 115.1 | | | | | 99.3 | 26.01 | 12.29 |
| #19 | transmission (μW) | | 12.0 | 80.8 | 9.71 | 79.8 | 11.7 | 83.8 | 5.7 | 80.6 | 14.7 | 75.1 | 6.3 | 69.5 | 5.3 | 72.5 | | | | | | |
| l=0.25mm | alpha (1/cm) | | 76.3 | 84.8 | 84.3 | 76.8 | 78.8 | 107.5 | 106.0 | 68.1 | 65.2 | 99.1 | 96.0 | 102.9 | 104.6 | | | | | 88.5 | 21.50 | 26.28 |
| #21 | transmission (μW) | 68.1 | 19.5 | 71.8 | 28.7 | 80.6 | 30.4 | 78.3 | 24.2 | 73.1 | 22.2 | 75.1 | 23.3 | 66.3 | 23.3 | 71.1 | | | | | | |
| l=0.25mm | alpha (1/cm) | 50.0 | 52.1 | 36.7 | 41.3 | 39.0 | 37.8 | 47.0 | 44.2 | 47.7 | 48.7 | 46.8 | 41.8 | 41.8 | 44.6 | | | | | 44.3 | 17.79 | 17.13 |
| #22 | transmission (μW) | 49.6 | 1.13 | 55.6 | 1.22 | 60.9 | 1.31 | 52.1 | 1.31 | 63.8 | 1.07 | 69.2 | | | | | | | | | | |
| l=0.25mm | alpha (1/cm) | 151.3 | 155.8 | 152.8 | 156.4 | 153.6 | 147.3 | 147.3 | 155.4 | 163.5 | 166.8 | | | | | | | | | 155.0 | 7.58 | 4.97 |
| #23 | transmission (μW) | 72.9 | 1.04 | 98.9 | 0.986 | ... | 1.21 | 75.9 | 1.06 | 83.8 | 1.13 | 81.5 | ... | 79.5 | | | | | | | | |
| l=0.25mm | alpha (1/cm) | 170.0 | 182.2 | 184.3 | | 165.6 | 170.8 | 174.8 | 172.2 | 171.1 | | | | | | | | | | 173.9 | 6.00 | 4.79 |
| #31 | transmission (μW) | 0.361 | 0.02 | 0.253 | 0.033 | 0.271 | 0.037 | 0.262 | 0.019 | 0.268 | | | | | | | | | | | | |
| l=0.25mm | alpha (1/cm) | 115.7 | 101.5 | 81.5 | 84.2 | 79.6 | 78.3 | 105.0 | 105.9 | | | | | | | | | | | 94.0 | 23.16 | 16.67 |
| #37 | transmission (μW) | 0.705 | 0.056 | 0.733 | 0.054 | 0.695 | 0.049 | 0.748 | 0.062 | 0.662 | 0.052 | 0.646 | 0.062 | 0.635 | 0.066 | 0.566 | | | | | | |
| l=0.25mm | alpha (1/cm) | 101.3 | 102.9 | 104.3 | 102.2 | 106.1 | 109.0 | 99.6 | 94.7 | 101.8 | 100.8 | 93.7 | 93.1 | 90.6 | 86.0 | | | | | 99.0 | 10.12 | 13.18 |
| #40 | transmission (μW) | 4.57 | 0.78 | 3.68 | 0.455 | 3.22 | | | | | | | | | | | | | | | | |
| l=0.25mm | alpha (1/cm) | 70.7 | 62.1 | 83.6 | 78.3 | | | | | | | | | | | | | | | 73.7 | 13.51 | 15.76 |
| #41 | transmission (μW) | 3.2 | 0.102 | 4.08 | 0.106 | 3.91 | 0.072 | 2.88 | 0.078 | 4.15 | 0.091 | 3.94 | 0.114 | 4.20 | | | | | | | | |
| l=0.25mm | alpha (1/cm) | 137.8 | 147.6 | 146.0 | 144.3 | 159.8 | 147.6 | 144.4 | 159.0 | 152.8 | 150.7 | 141.7 | 144.3 | | | | | | | 148.0 | 7.97 | 6.86 |
| #42 | transmission (μW) | | 0.019 | 0.322 | 0.021 | 0.264 | 0.014 | 0.291 | 0.034 | 0.335 | 0.029 | ... | 0.029 | 0.446 | 0.044 | 0.534 | 0.046 | 0.559 | | | | |
| l=0.25mm | alpha (1/cm) | | 113.2 | 109.2 | 101.3 | 117.5 | 121.4 | 85.9 | 91.5 | 97.9 | | 109.3 | 92.6 | 99.8 | 98.1 | 99.9 | | | | 102.9 | 17.96 | 16.53 |
| #43 | transmission (μW) | 0.213 | 0.028 | 0.487 | 0.019 | 0.424 | 0.021 | 0.459 | 0.023 | 0.596 | ... | 0.524 | 0.018 | | | | | | | | | |
| l=0.25mm | alpha (1/cm) | 81.2 | 114.2 | 129.8 | 124.2 | 120.2 | 123.4 | 119.7 | 130.2 | | | 134.8 | | | | | | | | 119.7 | 12.61 | 32.22 |
| #48 | transmission (μW) | | 0.085 | 0.156 | 0.079 | 0.163 | 0.079 | 0.132 | | | | | | | | | | | | | | |
| l=0.20mm | alpha (1/cm) | | 30.4 | 34.0 | 36.2 | 36.2 | 25.7 | | | | | | | | | | | | | 32.5 | 11.45 | 21.01 |
| #52 | transmission (μW) | 3.18 | 0.246 | 3.28 | 0.127 | 2.23 | 0.065 | 2.03 | 0.029 | 2.33 | 0.059 | | | | | | | | | | | |
| l=0.25mm | alpha (1/cm) | 102.4 | 103.6 | 130.1 | 114.6 | 141.4 | 137.7 | 169.9 | 175.5 | 147.0 | | | | | | | | | | 135.8 | 29.20 | 24.61 |
| #53 | transmission (μW) | | 0.077 | 1.97 | 0.082 | 1.382 | 0.059 | 1.275 | | | | | | | | | | | | | | |
| l=0.25mm | alpha (1/cm) | | 129.7 | 127.2 | 113.0 | 126.1 | 122.9 | | | | | | | | | | | | | 123.8 | 4.77 | 8.72 |
| #54 | transmission (μW) | 1.556 | 0.086 | 1.379 | 0.073 | 1.343 | 0.092 | 1.335 | | | | | | | | | | | | | | |
| l=0.25mm | alpha (1/cm) | 115.8 | 111.0 | 117.5 | 116.5 | 107.2 | 107.0 | | | | | | | | | | | | | 112.5 | 4.47 | 4.90 |
| #32 | transmission (μW) | 3.68 | 0.741 | 4.18 | 0.566 | 3.83 | 0.55 | 4.38 | 0.826 | 3.12 | 0.824 | 4.02 | 0.502 | 4.50 | 0.554 | 4.95 | 0.502 | 5.59 | 0.467 | | | |
| l=0.25mm | alpha (1/cm) | 64.1 | 69.2 | 80.0 | 76.5 | 77.6 | 83.0 | 66.7 | 53.2 | 64.4 | 74.5 | 83.2 | 87.7 | 83.8 | 87.6 | 91.5 | 96.4 | 99.3 | | 78.7 | 26.09 | 32.50 |
| #56 | transmission (μW) | 3.26 | 0.553 | 2.04 | 0.646 | 2.77 | 0.563 | 2.79 | 0.251 | ... | 0.262 | | | | | | | | | | | |
| l=0.25mm | alpha (1/cm) | 71.0 | 52.2 | 46.0 | 58.2 | 63.7 | 64.0 | 96.3 | | | | | | | | | | | | 64.5 | 49.36 | 28.69 |
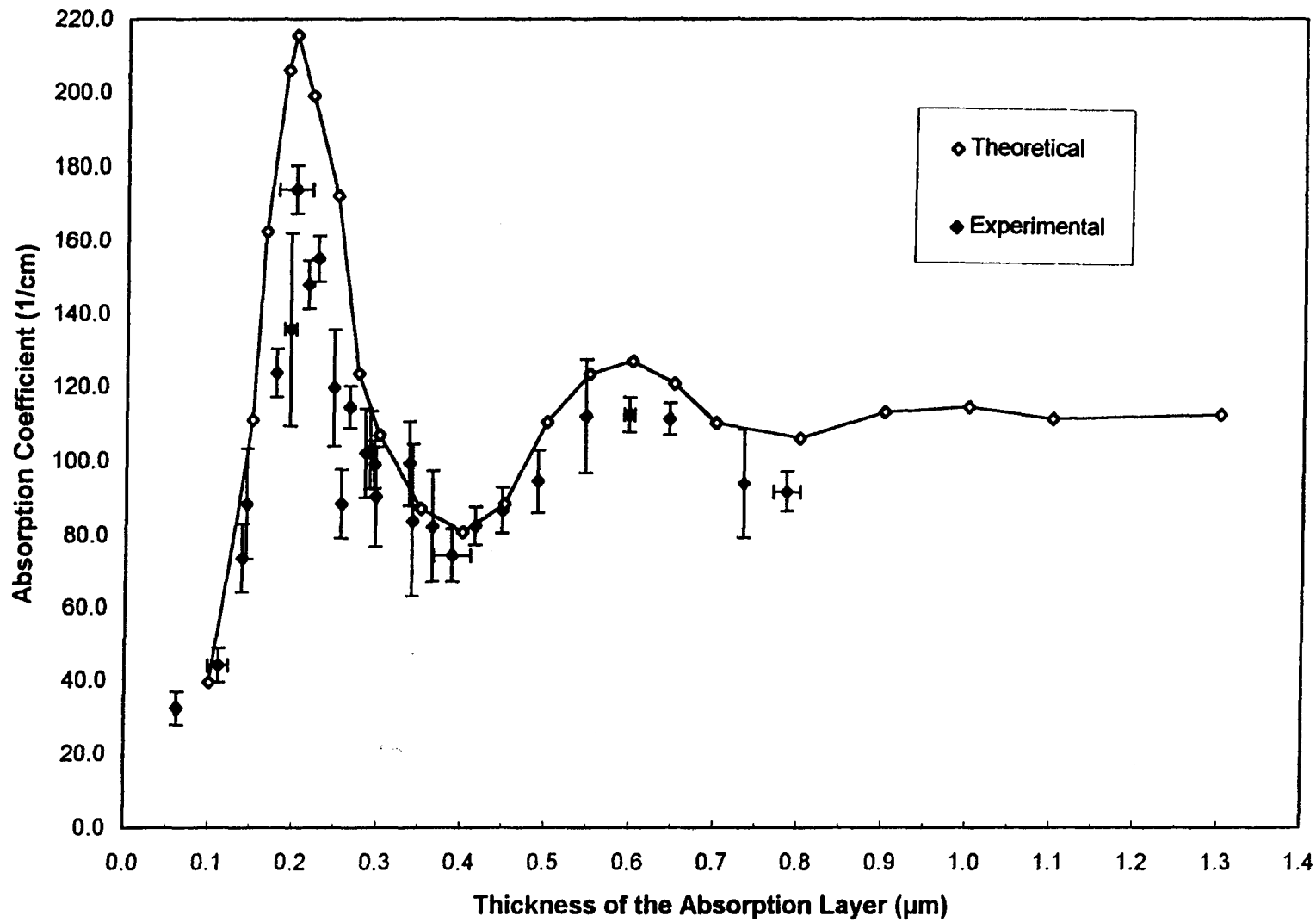
**Figure 3.14**    Measured absorption coefficients with error bars together with theoretical values as a function of the thickness of the GaAs absorbing layer.

From the experimental values, we can see that the predicted enhancement of the absorption for thicknesses around 0.2 and 0.6 μm and the reduction for a thickness of 0.4 μm are confirmed, although the measured enhancement is somewhat smaller. It is also noted that the agreement between the predicted and measured attenuation is better than that which was reported before as $115\pm16$cm$^{-1}$ for a single GaAs layer thickness of 0.4 μm [3.18]. Any deviation in the sample parameters in the experiment from the theoretical values will expect to drag the attenuation coefficient down from the predicted (local) maximum. The discrepancy between the calculated and measured values also relates to uncertainties in the extent of surface scattering.

## 3.8 Summary and Discussion

The absorption coefficient in a GaAs/AlGaAs optical waveguide tap structure has been measured. As had been predicted theoretically, it was found to have an oscillatory dependence on the GaAs absorbing layer thickness. For the waveguide structure considered in this section, a 0.2 μm thick absorbing layer results in an absorption coefficient that is approximately twice as large as for a very thick ($\geq$1μm) layer. This effect must be taken into account in the design of waveguide photodetectors and optical taps. While the use of relatively thin absorbing layers can increase the waveguide-to-detector coupling, it also makes the design less tolerant to small thickness variations. In the case of optical taps, precise control of the optical coupling is more important than achieving the maximum coupling strength, so thicker absorber layers which are outside the oscillatory range are preferred.

## Chapter 4  Franz-Keldysh Effect in Our Device

### 4.1 Introduction

Various devices for modulation, detection, and all-optical switching have been developed for use in optical computing and ultra-fast telecommunications. A large family of these devices is based on the electroabsorption effect in which the absorption coefficient is enhanced with an applied field.

The electroabsorption effect for photon energies below the band gap energy in bulk semiconductors was identified by Franz [4.1] and Keldysh [4.2] in 1958, and is known as the Franz-Keldysh effect. They explained the electric field effect as being a shift of the band edge toward the red. The early works on CdS [4.3] and GaAs [4.4] interpreted the effect as a shift to lower energies of an exponential absorption edge. Tharmalingam [4.5] and Callaway [4.6] further analyzed the expression for the optical absorption coefficient for direct transitions in 1963. In 1976, the electroabsorption effect in semiconductor bulk material was exploited as an optical modulator by Stillman et al.[4.7]. A. Schmeller, et al. reported photocurrent experiments on the Franz-Keldysh effect in a two-dimensional system of InGaAs/GaAs material[4.8]. Their resulting photo-I-V characteristic shows high potential for electro-optic applications.

In our experiments, the Franz-Keldysh effect was employed in an effort to broaden the operating wavelengths in our device, and try to make efficient use of the light below the band gap energy.

### 4.2 Basic Concept and Image of the Franz-Keldysh Effect

The principle of the electroabsorption modulator is that when light, which has a photon energy slightly below the absorption edge ($\approx E_g$) passes through the modulator, absorption is negligible and transmission is high. But with an applied electric field, the absorption edge is shifted which results in high absorption and low transmission. The modulation of absorption and transmission

by an electrical signal is the electroabsorption effect. And the electroabsorption effect in bulk semiconductor is attributed to the Franz-Keldysh effect which can be simply put as that at a given energy there is a greater probability of finding the electron (or the hole) inside the energy gap, or that the tunneling probability is increased when an electric field is present.

Direct-gap semiconductors exhibit strong electroabsorption, i.e., an increase of optical absorption with electric field, while the effect is negligible in indirect-gap materials such as Si. Fig.4.1 is for the case of GaAs in the presence of a strong electric field from which we can see that its absorption edge is shifted to longer wavelength. Because of the steepness of the absorption edge in a direct bandgap material such as GaAs, large changes in absorption of wavelength near the band edge can be produced by the application of an electric field.

The mechanism responsible for the Franz-Keldysh effect can be described straightforwardly with reference to the semiconductor energy band diagram shown in Fig.4.2. When a strong electric field is present, the band edges bend. The left-hand limit of the diagram represents the surface of the semiconductor, at which a Schottky barrier contact is formed.
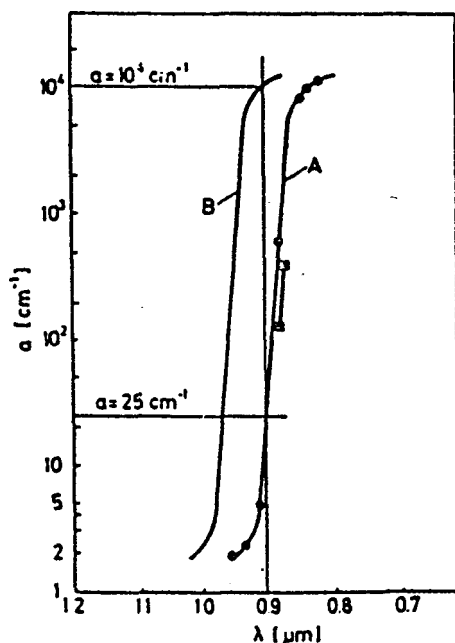


Figure 4.1 Franz-Keldysh shift of the absorption edge of GaAs. Curve A is the zero field absorption cureve for GaAs; Curve B shows the shifted absorption edge for a field of $1.3 \times 10^5$ V/cm. [after ref.4.10]

A charge depletion layer is formed and extends to depths x within the semiconductor after the application of a reverse-bias voltage to this rectifying junction. A nonuniform electric field is present within the depletion layer, with the largest amplitude existing at the surface. Outside of the depletion layer, the bands are flat, as at the right side of the figure. In this region, a photon can be absorbed only if it has enough energy to raise an electron across the bandgap, as in transition (a) of Fig.4.2. Closer to the surface, where the bands have been bent by the field, a transition (b) can occur in which photon energy is sufficient only to lift the electron partway across the gap. Ordinarily such a transition could not occur because there would be no allowed

E

(b)

(a)

Ec

Ev

x
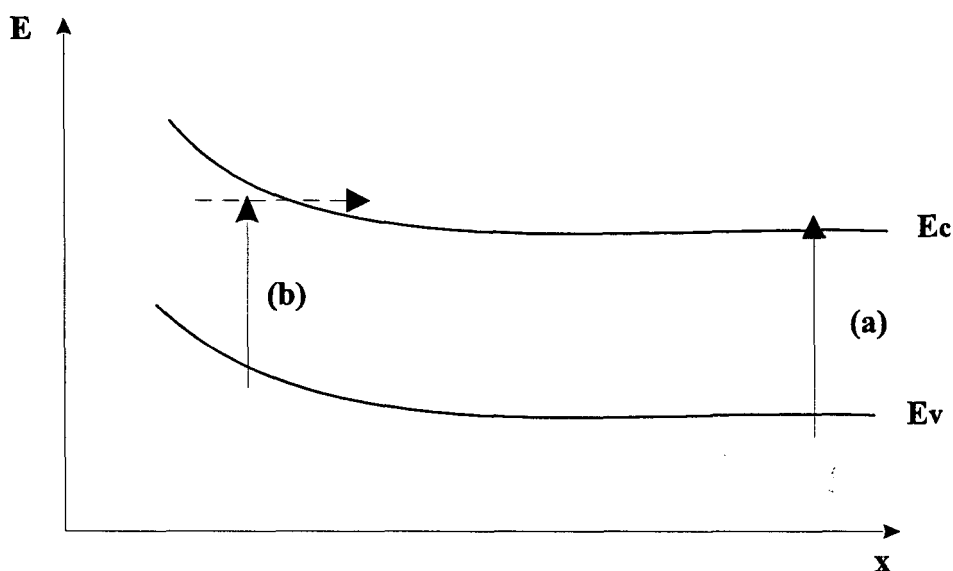
Fig. 4.2   Energy band diagram of a semiconductor exhibiting the Franz-Keldysh effect in the presence of a strong electric field. The parameter x represents the distance from the surface of the semiconductor, and E is the electron energy. Ec and Ev are the conduction and valence bandedges, respectively.

electron state within the bandgap. However, the electric field effectively broadens the states of the conduction band so that there is a finite probability of finding the electron in the gap. This, of course, reduces the effective bandgap and thereby shifts the absorption edge to longer wavelength.

The probability of finding an electron in the energy gap away from the band edge decreases according to [4.9]:

$$\exp(-\frac{|E - E_e|}{\Delta E}) \tag{4.1}$$

where E is the energy in the gap at position x, $E_e$ is the energy of the band edge at x and ΔE is a parameter which depends on the field. Therefore the states at the band edges are effectively broadened exponentially into the gap by an average deviation ΔE.

It can be shown that the effective change in bandgap energy ΔE is given by [4.9]

$$\Delta E = \frac{3}{2}(m*)^{-1/3}(q\hbar\mathscr{E})^{2/3} \tag{4.2}$$

where m* is the effective mass of the carrier, q is the magnitude of the electrical charge of a carrier, ħ is Planck's constant divided by 2π, and $\mathscr{E}$ is the electric field strength.

## 4.3 Theoretical Deduction of Absorption Coefficient in Franz-Keldysh Effect

Let us consider the case of a uniform applied electric field, $V(\mathbf{r})=e\,\mathbf{F}\cdot\mathbf{r}$. The Schrödinger equation for the wave function ϕ(r) is:

$$(\frac{-\hbar^2}{2\mu}\nabla^2 + e\mathbf{F}\cdot\mathbf{r})\phi(\mathbf{r}) = E\phi(\mathbf{r}) \tag{4.3}$$

Here μ is the reduced effective mass, defined by $1/\mu=(1/m_e*)+(1/m_h*)$. Assume that the applied field is in the z direction, $\mathbf{F}=\hat{z}\,F$. The solution can be written as

$$\phi(\mathbf{r}) = \frac{e^{ik_x x + ik_y y}}{\sqrt{A}} \phi(z) \qquad (4.4)$$

where the z-dependent wave function $\phi(z)$ satisfies

$$\left(\frac{-\hbar^2}{2\mu} \frac{d^2}{dz^2} + eFz\right)\phi(z) = E_z \phi(z) \qquad (4.5)$$

and the total energy E is

$$E = \frac{\hbar^2}{2\mu}(k_x^2 + k_y^2) + E_z \qquad (4.6)$$

The solution of the Schrödinger equation (4.5) with a uniform field can be obtained by a change of variable:

$$Z = \left(\frac{2\mu eF}{\hbar^2}\right)^{1/3}\left(z - \frac{E_z}{eF}\right) \qquad (4.7)$$

Therefore,

$$\frac{d^2\phi(Z)}{dZ^2} - Z\phi(Z) = 0 \qquad (4.8)$$

The Airy functions Ai(Z) or Bi(Z) (and Bi(x) is sometimes referred to as the Bairy function) are the solutions. Ai(x) and Bi(x) are linearly independent solutions of the Airy equation:

$$y''(x) = xy(x) \qquad (4.9)$$

We use the integral representations [4.11, 4.12]

$$Ai(x) = \frac{1}{\pi} \int_0^\infty \cos(\frac{s^3}{3} + sx) ds \qquad (4.10a)$$

$$Bi(x) = \frac{1}{\pi} \int_0^\infty \left[ \exp\left( -\frac{s^3}{3} + sx \right) + \sin(\frac{s^3}{3} + sx) \right] ds \qquad (4.10b)$$

although some authors use a factor of $\pi^{1/2}$ rather than $\pi$. The real wave function satisfies the normalization condition

$$\int_{-\infty}^\infty dz \phi_{E_{z1}}(z) \phi_{E_{z2}}(z) = \delta(E_{z1} - E_{z2}) \qquad (4.11)$$

The absorption coefficient is given by [4.13]

$$\alpha(\omega) = C_0 |\ell \cdot P_{cv}|^2 2 \sum_n |\phi_n(0)|^2 \delta(\xi_n + E_g - \hbar\omega) \qquad (4.12)$$

where n corresponds to the discrete and continuum states of $\phi(r)$, e is a unit vector in the electric field direction, and $C_0$ is defined by

$$C_0 = \frac{\pi e^2}{n_r c \epsilon_0 m_0^2 \omega} \qquad (4.13)$$

Here $\omega$ is the optical angular frequency, c is the speed of light in free space, $n_r$ is the refractive index of the material, $m_0$ is the free electron mass, $e=-|e|$ for electrons and $\epsilon_0$ is the permittivity in free space.

Since the quantum number is determined by $(k_x, k_y, E_z)$ as described above in the wave function Eq.(4.4) and the corresponding energy spectrum Eq.(4.6), the sum over all the states n for the

absorption spectrum in Eq.(4.12) has to be replaced by the sum over all the quantum numbers:

$$\sum_n \rightarrow \sum_{k_x} \sum_{k_y} \int dE_z \tag{4.14}$$

where the sum over the energy $E_z$ is an integral since $E_z$ is a continuous spectrum and a delta function normalized rule Eq.(4.11) has been adopted. Therefore,

$$\alpha(\hbar\omega) = A_0 2 \sum_{k_x k_y} \int dE_z |\phi(\mathbf{r}=0)|^2 \delta\left[\frac{\hbar^2}{2\mu}(k_x^2 + k_y^2) + E_z + E_g - \hbar\omega\right] \tag{4.15}$$

where $A_0$ is given by

$$A_0 = \frac{\pi e^2 |\ell \cdot P_{cv}|^2}{n_r c \varepsilon_0 m_0^2 \omega} \tag{4.16}$$

and the momentum-matrix element of a bulk semiconductor is [4.14]

$$|\ell \cdot P_{cv}|^2 = \frac{m_0}{6} E_P \tag{4.17}$$

where $E_p$ is the energy parameter for the matrix element [4.14]. The integration for the absorption coefficient is carried out

$$\alpha(\hbar\omega) = A_0 \frac{\mu}{\pi\hbar^2} \int_{-\infty}^{\hbar\omega-E_g} dE_z |\phi_{E_z}(z=0)|^2$$

$$= A_0 \frac{\mu}{\pi\hbar^2} \int_{-\infty}^{\hbar\omega-E_g} dE_z \left(\frac{2\mu}{\hbar^2}\right)^{2/3} \frac{1}{(eF)^{1/3}} Ai^2\left[\left(\frac{2\mu}{\hbar^2 e^2 F^2}\right)^{1/3}(-E_z)\right] \tag{4.18}$$

Let

$$\hbar\theta_F = \left(\frac{\hbar^2 e^2 F^2}{2\mu}\right)^{1/3} \qquad \tau = -\frac{E_z}{\hbar\theta_F} \qquad \eta = \frac{E_g - \hbar\omega}{\hbar\theta_F} \qquad (4.19)$$

We find the absorption coefficient

$$\alpha(\hbar\omega) = \frac{A_0}{2\pi}\left(\frac{2\mu}{\hbar^2}\right)^{3/2} \sqrt{\hbar\theta_F} \int_\eta^\infty d\tau Ai^2(\tau)$$

$$= \frac{A_0}{2\pi}\left(\frac{2\mu}{\hbar^2}\right)^{3/2} \sqrt{\hbar\theta_F}\left[-\eta Ai^2(\eta) + Ai'^2(\eta)\right] \qquad (4.20)$$

where Ai'($\eta$) is the derivative of Ai($\eta$) with respect to $\eta$.

Physically, Franz-Keldysh absorption below the band gap results from electrons tunneling between the conduction band and both light- and heavy-hole valence bands. The total absorption is given by Bennett and Soref [4.10]:

$$\alpha(\omega,\xi) = \frac{B\pi}{nc\omega}\left\{\mu_{ehh}^{3/2}\left[1+\frac{m_0}{m_{hh}}\right]\theta_1^{1/2}\left[|Ai'(x_1)|^2 - x_1 Ai^2(x_1)\right] + \right.$$

$$\left. + \mu_{elh}^{3/2}\left[1+\frac{m_0}{m_{lh}}\right]\theta_2^{1/2}\left[|Ai'(x_2)|^2 - x_2 Ai^2(x_2)\right]\right\} \qquad (4.21)$$

where B is given by

$$B = \frac{4\pi e^5}{m^2\hbar^2} \qquad (4.22)$$

Let $\theta_i$ denote the function of the reduced effective mass of the electron and heavy- and light-holes, $\theta_{ehh}$ or $\theta_{elh}$, and the electric field.

$$\theta_1 = \theta_{ehh} = \left(\frac{e^2 F^2}{2\mu_{ehh}\hbar}\right)^{1/3} \qquad\qquad \theta_2 = \theta_{elh} = \left(\frac{e^2 F^2}{2\mu_{elh}\hbar}\right)^{1/3} \qquad (4.23)$$

And the argument of the Airy function is

$$x_i = \frac{\omega_g - \omega}{\theta_i} \qquad (4.24)$$

By substituting the values of the constants such as $\hbar$, $m_0$ and so on into the absorption coefficient equation, we get

$$\alpha(\omega,F) = \frac{1.0 \times 10^4}{n} F^{1/3} \sum_j \left(1 + \frac{m}{m_{v_j}}\right)\left(\frac{2\mu_j}{m}\right)^{4/3}$$

$$\times \left[ \left|\left(\frac{dAi(z)}{dz}\right)_{\beta_j}\right|^2 - \beta_j \left|Ai(\beta_j)\right|^2 \right] \qquad (4.25)$$

where

$$\beta_j = 1.1 \times 10^5 (E_g - \hbar\omega)(2\mu_j / m)^{1/3} F^{-2/3} \qquad (4.26)$$

where $\sum$ is the sum over the light- and heavy-hole valence bands; $j=1$ is for heavy-hole valence band; $j=2$ is for light-hole valence band; $m_{v1}$ stands for $m_{hh}$ and $m_{v2}$ stands for $m_{lh}$.

## 4.4 Numerial Calculation for Bulk GaAs

We calculated the absorption coefficient using Eq.(4.25) to get an idea of its increase under the

influence of the electric field. At room temperature the absorption edge of GaAs occurs at a wavelength of 0.870μm, and calculations were made at wavelength of 0.890μm.

For the numerical calculations the parameters were chosen as [4.8]:

n=const=3.63          $m_{v1}/m$=0.087          $\mu_1/m$=0.0377

$m_{v2}/m$=0.450          $\mu_2/m$=0.0579          Eg=1.424eV

To calculate the Airy function, we first considered the following equation:

$$\int^t \cos\left(\frac{1}{3}t^3 + xt\right)dt = \frac{\sin\left(\frac{1}{3}t^3 + xt\right)}{t^2+x} + 2\int^t \sin\left(\frac{1}{3}t^3 + xt\right)\frac{tdt}{\left(t^2+x\right)^2} \qquad (4.27)$$

As t→∞, the first term on the right side of Eq.(4.27) vanishes, and the last integral converges absolutely. Fig.4.3 is the Airy function and its derivative in the corresponding range of the electric field. Fig.4.4 is our calculated absorption for bulk GaAs at the wavelength of 890nm as the electric field increases.

## 4.5 Experimental Results

Experimentally, we observed photocurrent increase as the applied electric field increases at the wavelength of 890nm. We measured the photocurrent of one detector with the other in-line detectors electrically floated. Fig.4.5 is the photocurrent of the first detector in the switch array with different input light power, and Fig.4.6 shows the photocurrents for the four in-line photodetectors at the input power level of 431μw.

Comparing our numerical calculation of the absorption coefficient with experimentally obtained photocurrent of the detector against the bias voltage, we see that the Franz-Keldysh effect accounts mainly for the rise in the photocurrent as the bias voltage increases at 890nm
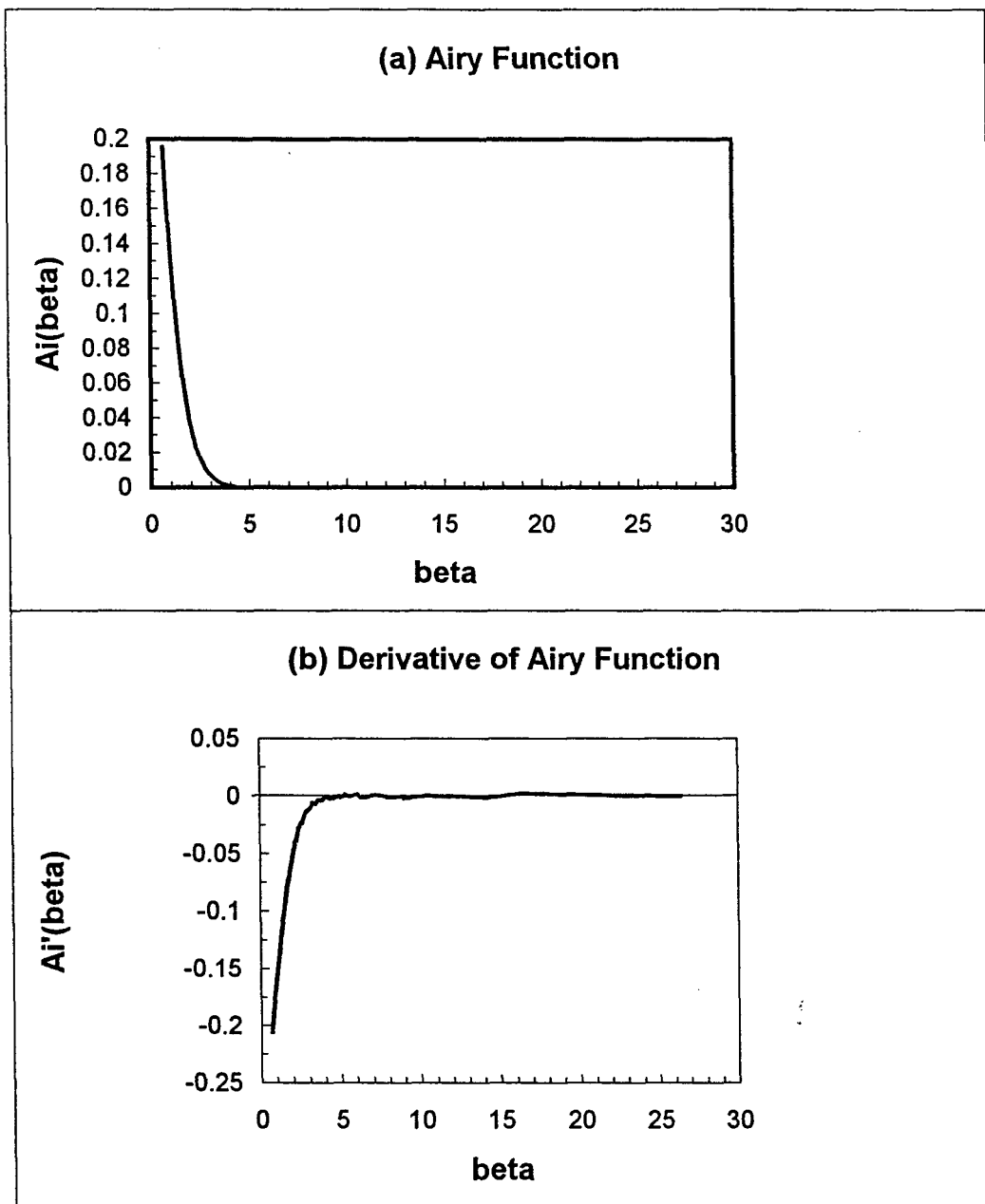
Figure 4.3 (a) Airy function and (b) derivative of the Airy function for beta values in the range of the considered electric field.
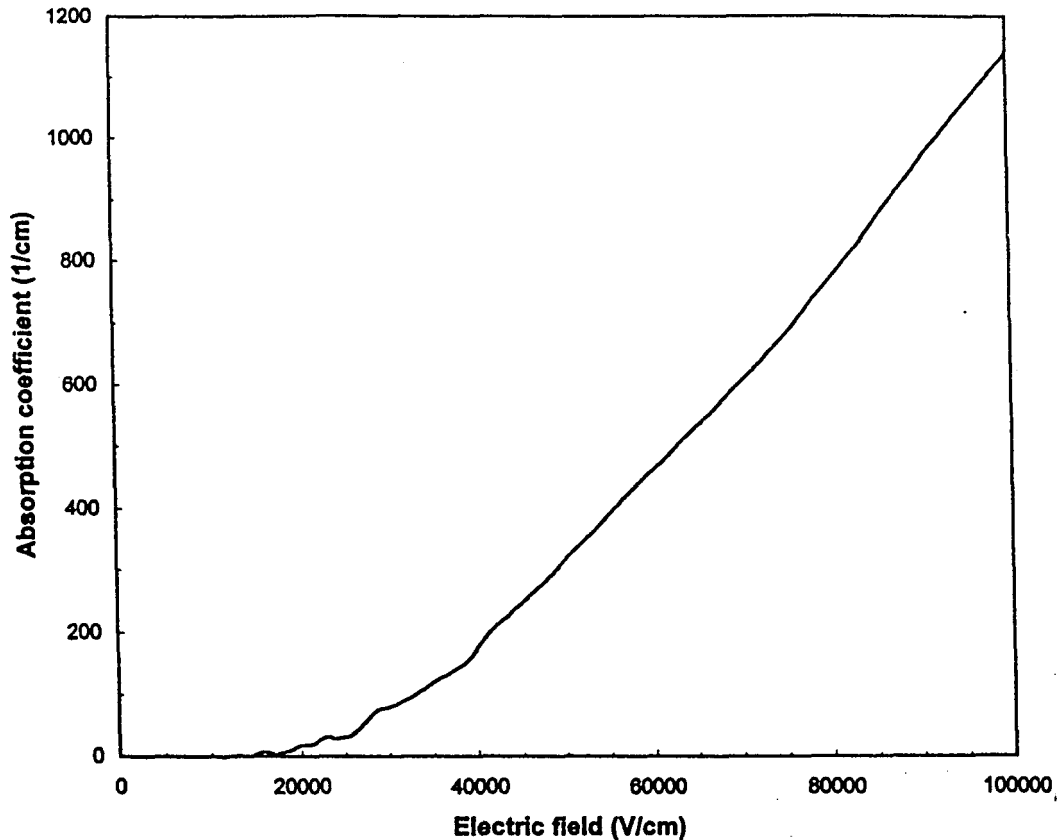
Fig. 4.4 Calculated Franz-Keldysh electroabsorption coefficient for GaAs at the
at the wavelength of 890nm vs. the applied electric field.

wavelength. So, for the on-state GaAs detector, they can draw much more photocurrent than zero-biased states at 890nm.

Let us compare the I-V characteristics of the detectors' at 890nm with that at 820nm. When $E_{photon}$ is greater than $E_{gap}$ and at low bias voltages, the responsivity of the detectors increases with increasing bias, however, the fraction of the input power that is absorbed in the detector is independent of the bias voltage. Under such conditions, a well-designed matrix switch will share the input signal evenly among all of the detectors in the array along a given waveguide. However, as the wavelength increases, the absorption in the lead detector decreases, allowing more light to reach the subsequent detectors. At longer wavelengths, when the photon energy approaches the bandgap, the absorption of the GaAs is significantly greater due to the Franz-Keldysh effect. This

67



**Figure 4.5**    I-V characteristics of the first photodetector in the array as a function of bias voltage for a series of input power levels at a wavelength of 890nm.

**Figure 4.6** I-V characteristics of the four in-line photodetectors for a fixed optical input power level of $431\mu W$ at wavelength 890nm.
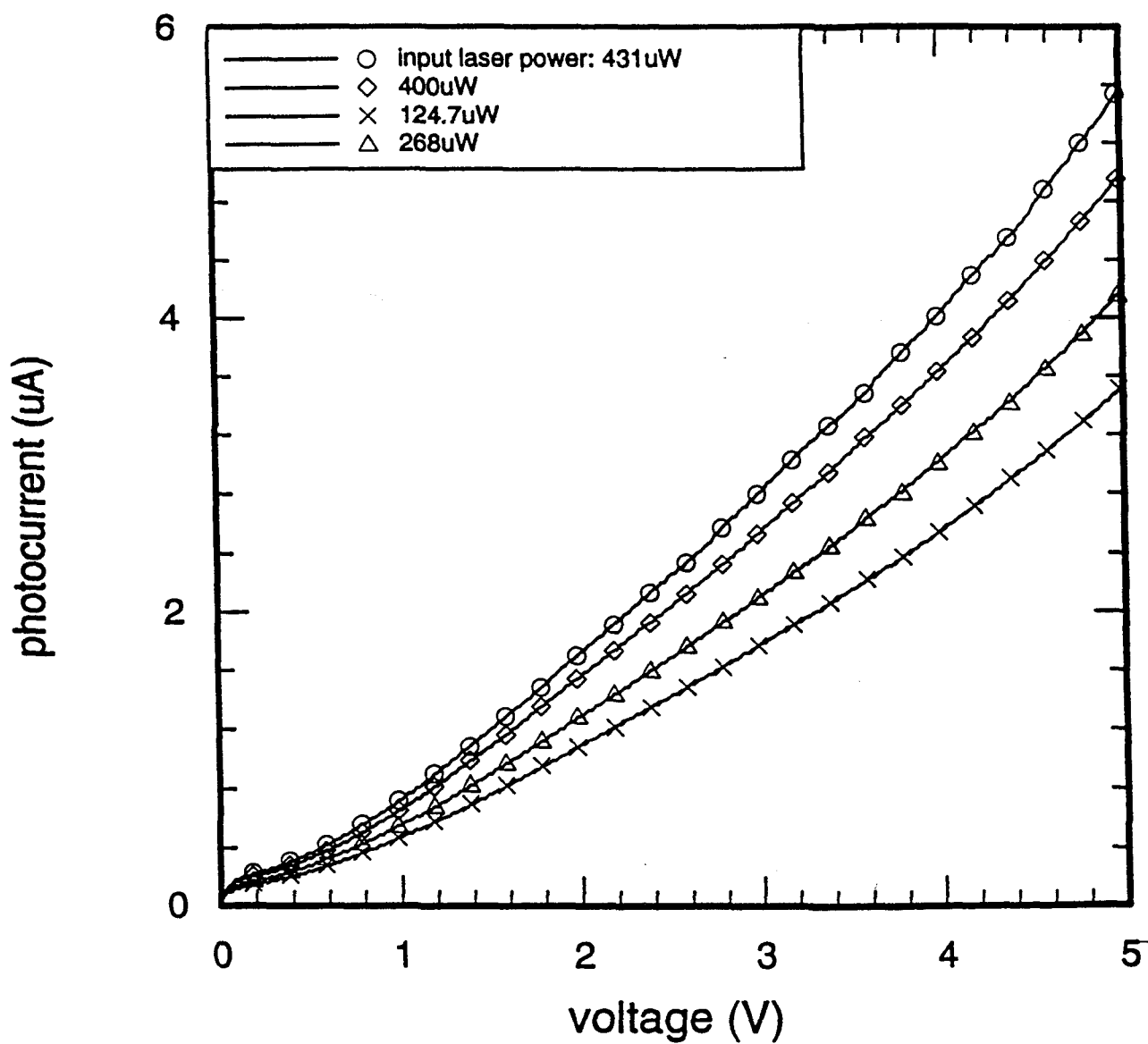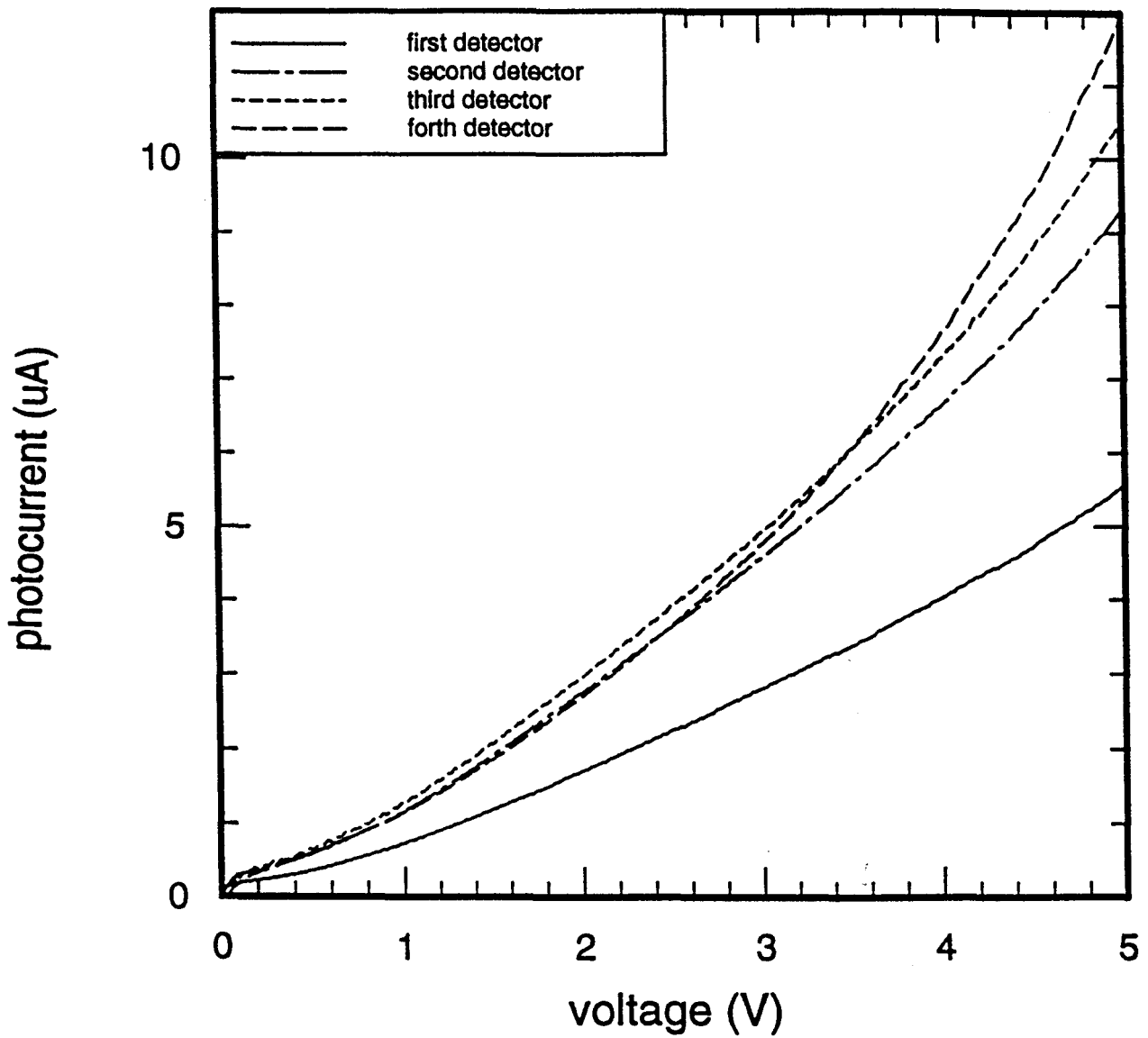
effect can enhance the absorption in the higher-biased state relative to the absorption in the lower-biased state. Thus, more efficient use can be made of the available input power.

In order to simulate a wide range of coupling strengths, the diode laser was replaced by a titanium: sapphire laser that could be tuned continuously on either side of the GaAs band edge to vary the absorption coefficient. The photocurrent of the first detector in the in-line detectors was measured at different bias voltages while the wavelength was tuned from 850 to 910 nm by X.C. Wu [4.15]. Each curve was normalized with respect to the photocurrent at 850nm. The result is shown in Fig.4.7. From this figure, we can see that in the wavelength range greater than the band gap wavelength (i.e., ~870nm), that is, for light that has a photon energy less than the band gap energy, as the bias voltage increases, the relative photocurrent also increases. While for the wavelengths shorter than the band edge wavelength, the photocurrent relatively drops a little as the electric field increases. So, a red shift for the band gap results due to Franz-Keldysh effect.

For the electroabsorption response in the Franz-Keldysh effect, transmission through the detector was measured both with and without the applied voltage. The spectra of the laser light transmitted through the detector with different bias voltages at the wavelengths of 820nm and 890nm, respectively. The results are shown in Fig.4.8(a) and (b), respectively. Let us compare the transmission at the two wavelengths. For the wavelength of 890nm, there is an obvious drop in the transmission as the bias voltage goes up, which is an indication of the increase in light absorption in the detector section. While for the wavelength of 820nm, transmission decrease is not as much as the wavelength of 890nm.

The detector transmission can be taken as the photocurrent response of the subsequent detectors as it is proportional to the transmission of the leading ones. We biased the lead detector at on-state and measured the photocurrent against bias voltage in its subsequent detector which is assumed to be the transmission of the lead detector. Then we switch the lead detector to off-state and measured its transmission in the same way again. Typical results are shown in Fig.4.9 and the measured transmission changes are listed in Table 4.1. More transmission is allowed for the detector and the increase is about 10-30% when it is shifted from 5-volt-on-state to zero-biased state.
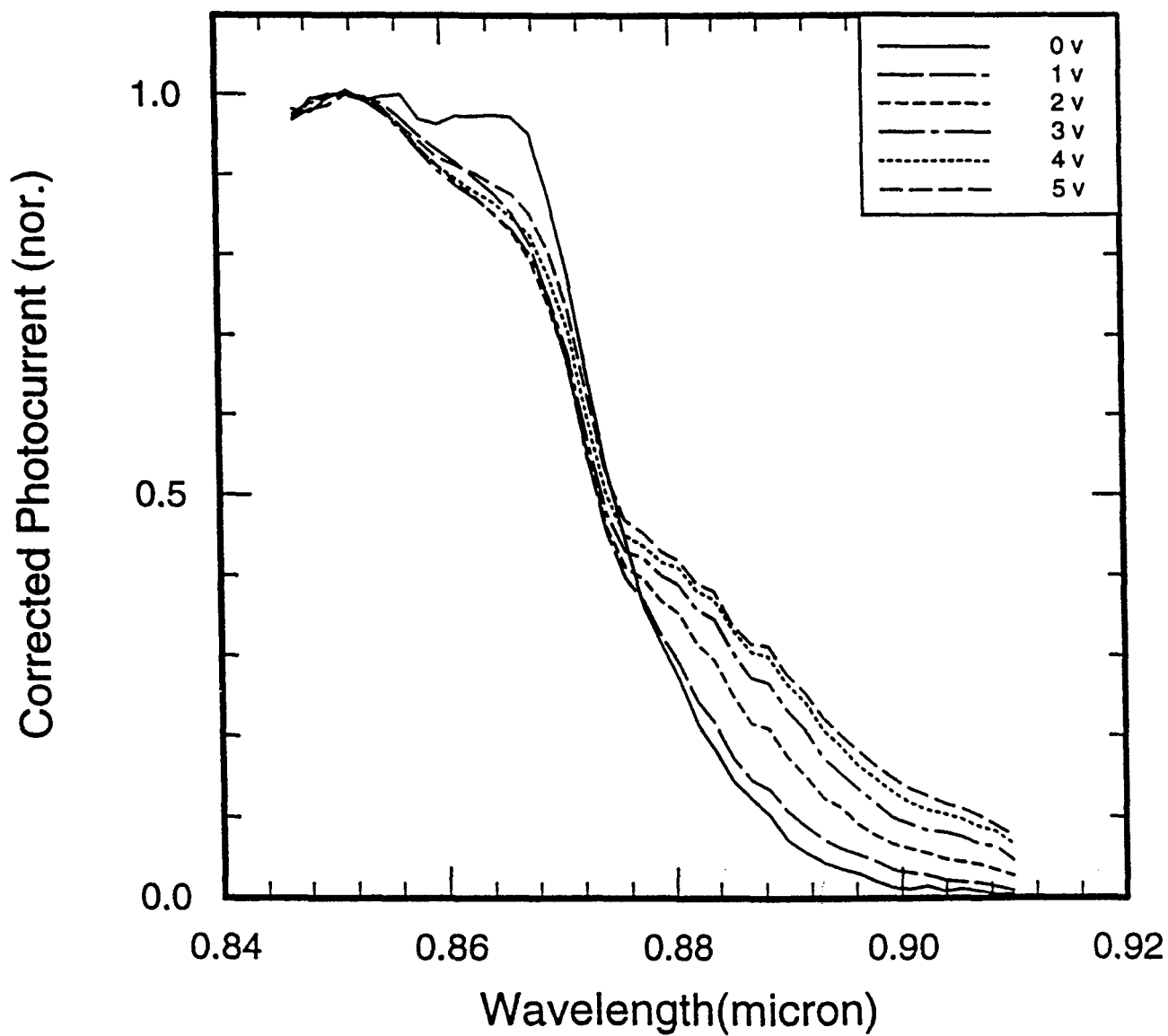
**Figure 4.7**    Photocurrent of the first detector measured at different bias voltages while the wavelength was tuned from 850 to 910nm. [after X.C.Wu]
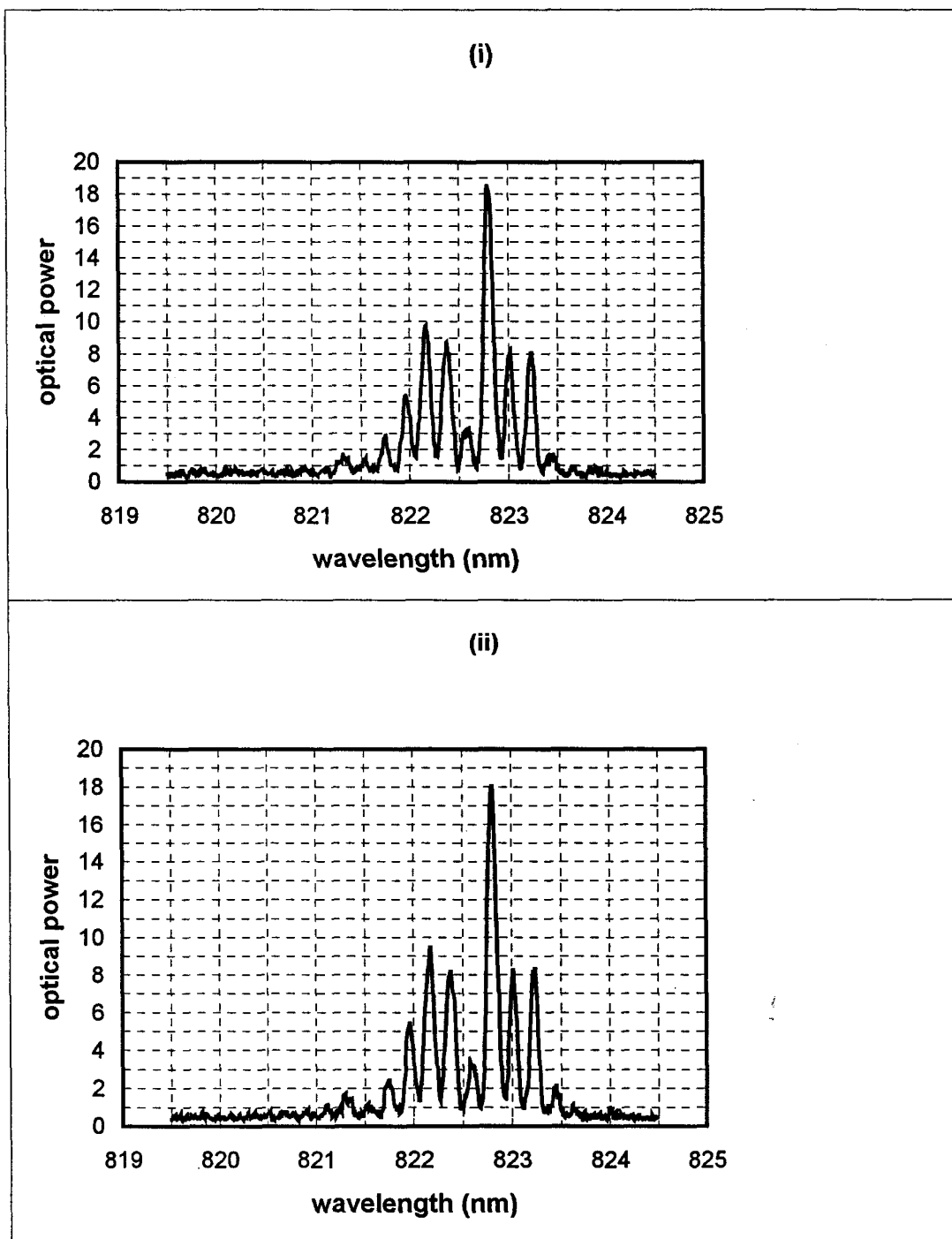
Figure 4.8 (a)  Spectrum of the first detector's transmission when it is biased at
( i ) zero volt, and ( ii ) five volts at the wavelength of 820nm, respectively.
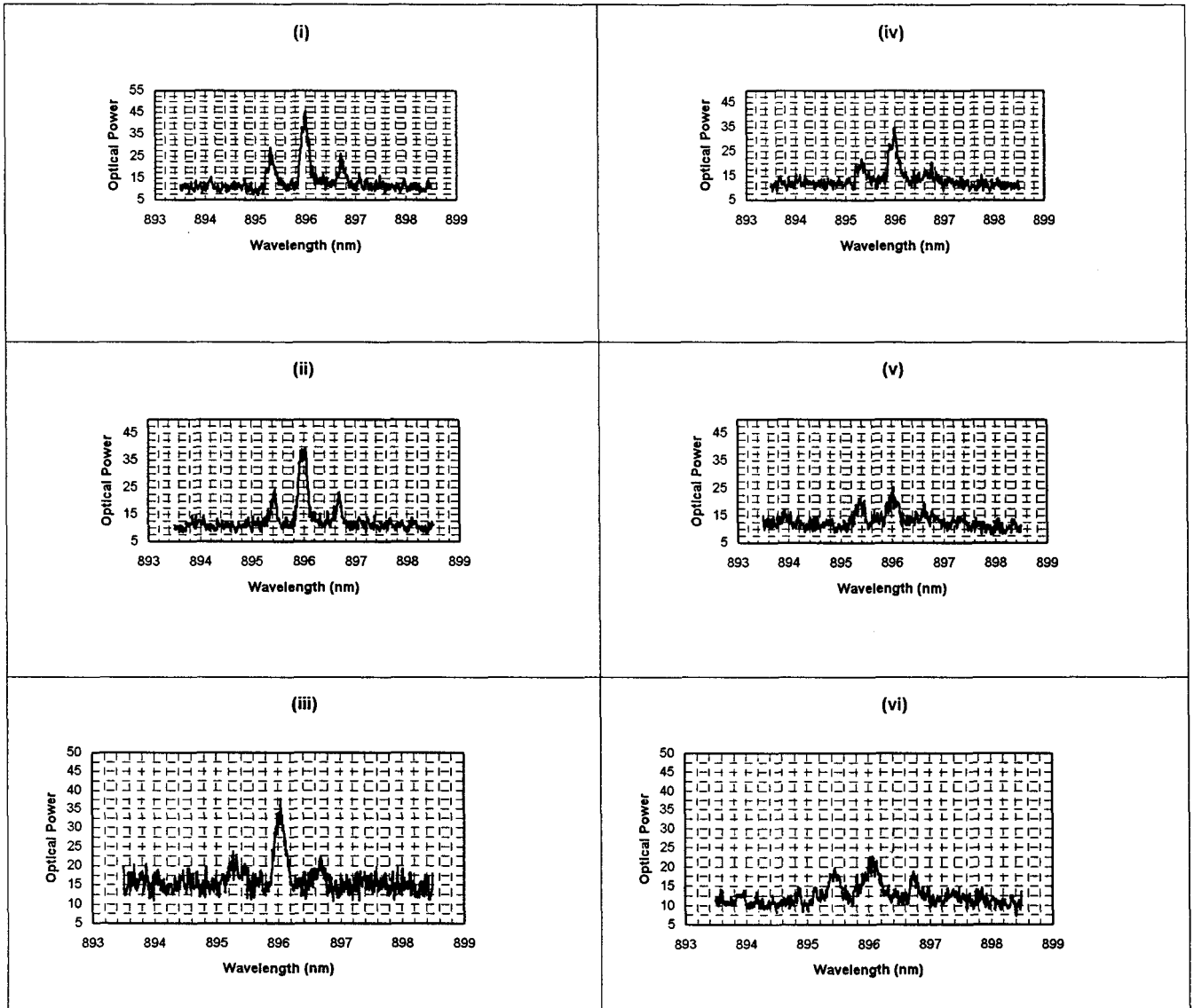
Figure 4.8(b)  Spectrum of transmission of the detector when it is biased at (i)0V, (ii)1V, (iii)2V, (iv)3V, (v)4V and (vi)5V at the wavelength of 890nm, respectively.
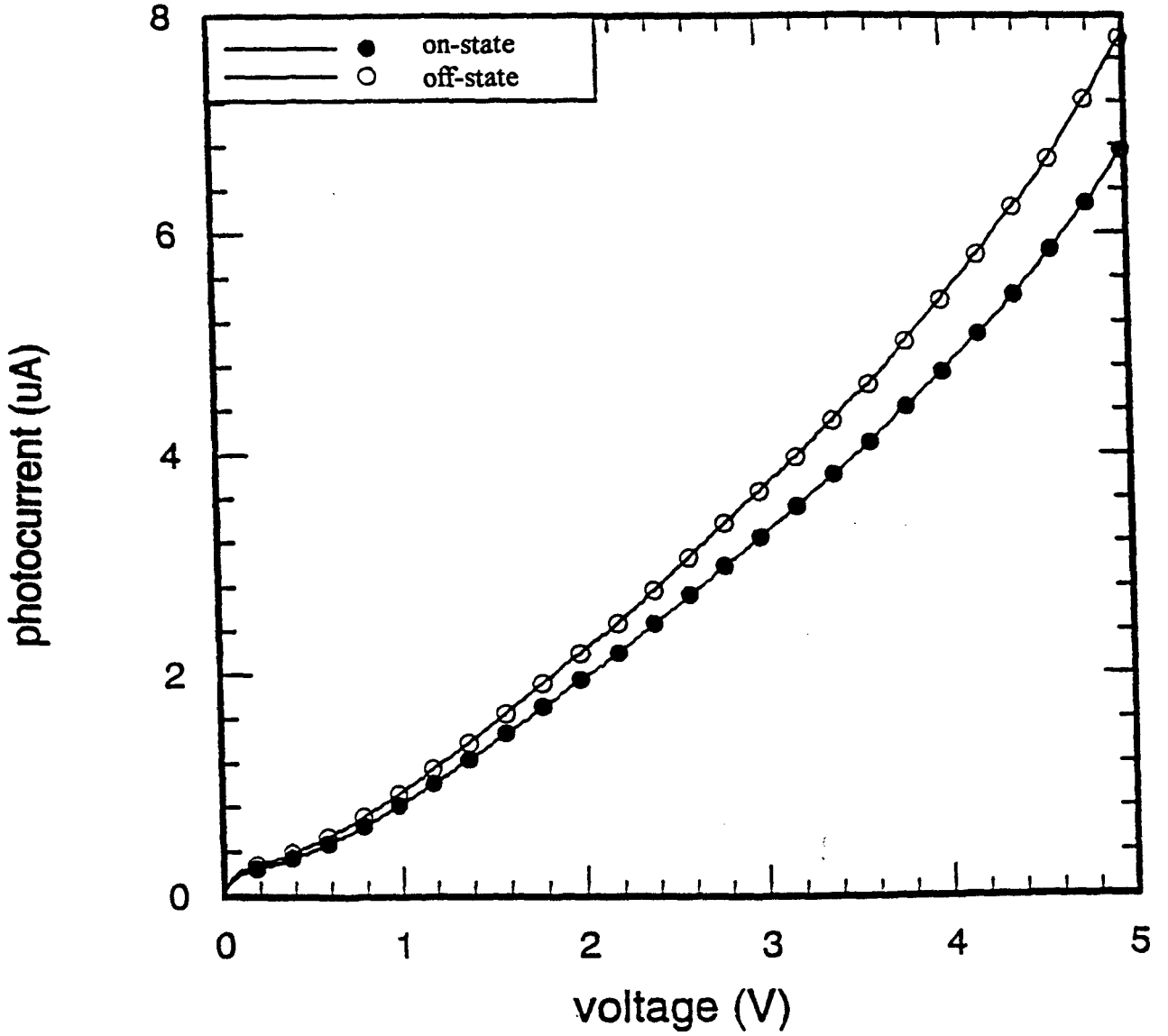
**Figure 4.9(a)** Photocurrent vs. bias voltage in the second detector for different bias conditions (on and off-states) in the first detector at the wavelength of 890nm for the case that the photodetectors are with interdigital contacts.
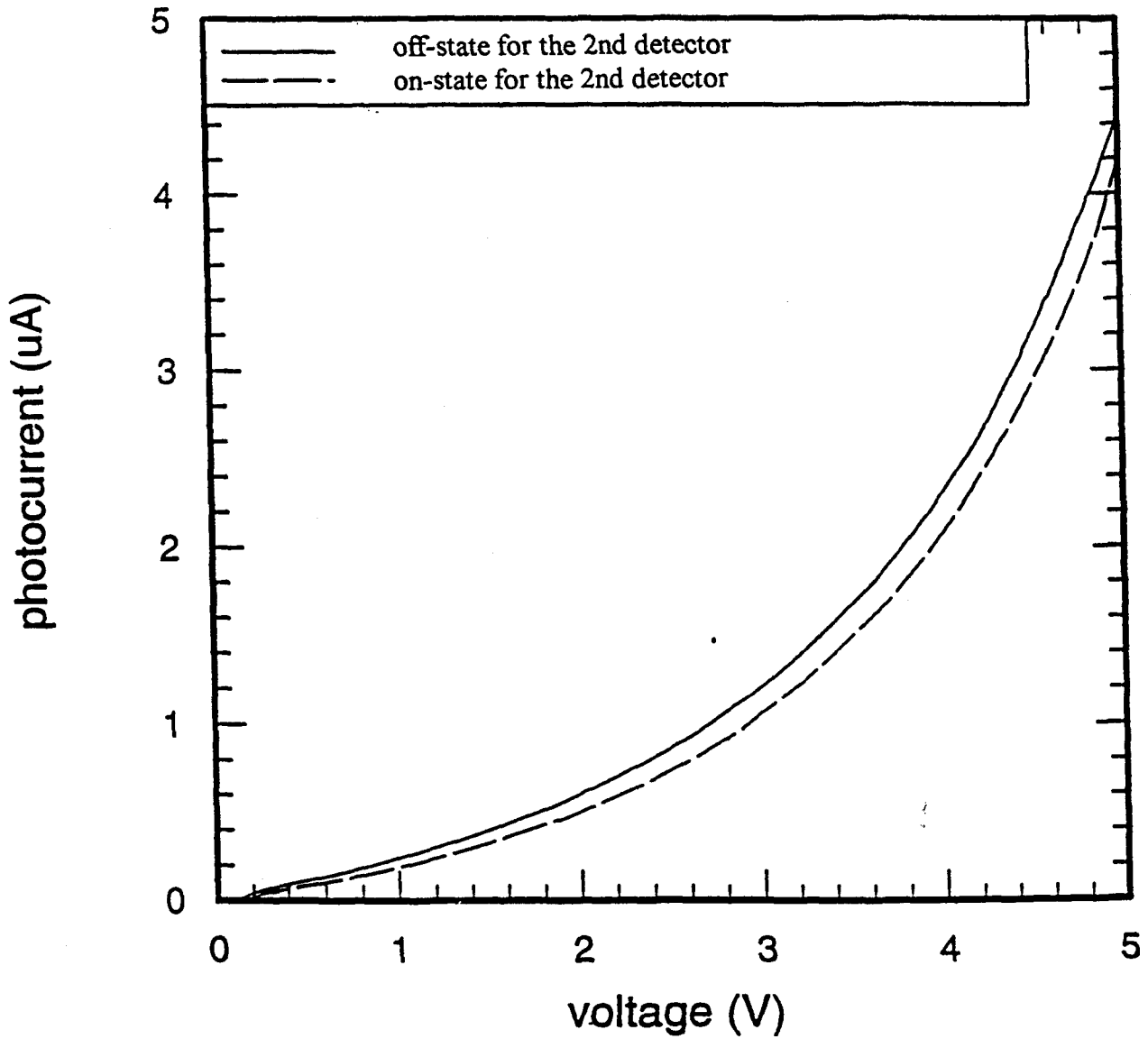
**Figure 4.9(b)** Photocurrent vs. bias voltage in the third detector for different bias
conditions (on and off-states) in the second detectors at the wavelength
of 890nm for the case that the photodetectors are with interdigital contacts.

**Figure 4.9(c)** Photocurrent vs. bias voltage in the fourth detector for different bias conditions (on and off-states) in the second and third detectors at the wavelength of 890nm for the case that the photodetectors are with interdigital contacts.

Table 4.1 Transmission Changes in the Franz-Keldysh Effect for the Detectors With and Without Fingers

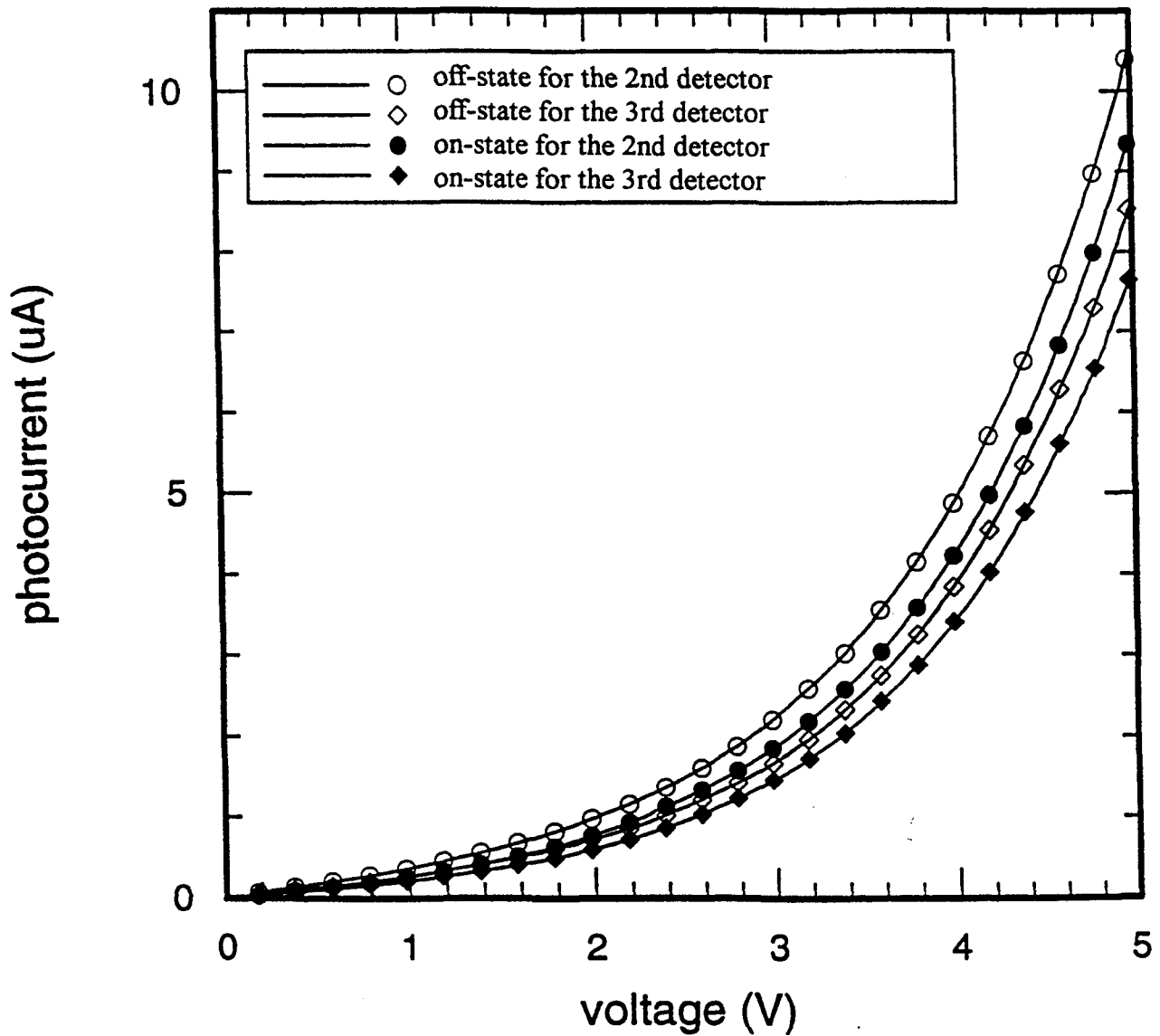| detectors | det. for output (uA)/det. for bias | 2nd/1st | 3rd/2nd | 3rd/1st | 4th/3rd | 4th/2nd | 4th/1st | 5th/4th | 5th/3rd | 5th/2nd | 5th/1st |
|---|---|---|---|---|---|---|---|---|---|---|---|
| detectors with fingers | with bias on the leading det. | 6.8 | 3.29 | | 7.71 | 9.39 | 9.58 | 4.97 | 4.41 | 5.43 | 4.86 |
| | with no bias on the leading det. | 7.79 | 4.3 | | 8.6 | 10.49 | 10.49 | 5.89 | 4.98 | 6.37 | 5.44 |
| | percentage of transmission increase (%) | 14.6 | 30.7 | | 11.5 | 11.7 | 9.5 | 18.5 | 12.9 | 17.3 | 11.9 |
| | with bias on the leading det. | 6.25 | 8.62 | 8.47 | 6.36 | 6.01 | 6.21 | 5.06 | 4.29 | 5.43 | 5.33 |
| | with no bias on the leading det. | 7.01 | 10.74 | 9.78 | 7.09 | 6.73 | 6.75 | 5.94 | 4.85 | 6.29 | 6.03 |
| | percentage of transmission increase (%) | 12.2 | 24.6 | 15.5 | 11.5 | 12.0 | 8.7 | 17.4 | 13.1 | 15.8 | 13.1 |
| | with bias on the leading det. | | 4.19 | | 7.17 | 9.49 | | | | | |
| | with no bias on the leading det. | | 4.45 | | 8.344 | 10.62 | | | | | |
| | percentage of transmission increase (%) | | 6.2 | | 16.4 | 11.9 | | | | | |
| detectors without fingers | with bias on the leading det. | 7.86 | 6.28 | 8.61 | | | | 5.43 | 5.65 | 5.92 | 5.78 |
| | with no bias on the leading det. | 9.31 | 10.46 | 10.49 | | | | 6.83 | 6.85 | 7.06 | 6.61 |
| | percentage of transmission increase (%) | 18.4 | 66.6 | 21.8 | | | | 25.8 | 21.2 | 19.3 | 14.4 |
| | with bias on the leading det. | 5.85 | 9.77 | 10.63 | 8.05 | 7.98 | 7.86 | 10.76 | 9.78 | 11.19 | |
| | with no bias on the leading det. | 6.55 | 13.11 | 12.98 | 9.4 | 9.41 | 8.89 | 11.72 | 11.81 | 13.85 | |
| | percentage of transmission increase (%) | 12.0 | 34.2 | 22.1 | 16.8 | 17.9 | 13.1 | 8.9 | 20.8 | 23.8 | |

## 4.6 Photodetectors without Interdigital Contacts

So far, the experiments that have been described deal with the regular detectors, that is, detectors with interdigital contacts. The interdigitated detectors are aimed at providing an increased area for receiving the available light, hence an increased responsivity. However, for operating wavelengths below the band gap, our emphasis may be also put on how to make effective use of the light. As far as the Franz-Keldysh effect is concerned, detector transmission increase from on-state to off-state should be favored. So let us consider a kind of photodetectors that do not have interdigital contacts (Fig.4.10).

Fig.4.11 shows the electric field distributions of the two kinds of the detectors, that is, one for detectors with fingers, the other, without. For the interdigitated detector (Fig.4.11(a)), the electric field distribution exists between the adjacent fingers that are oppositely biased. The electric field is zero underneath each metal finger. For the detectors without interdigitized fingers, electrodes are placed symmetrically on either side of the waveguide. A transverse electric field between the two electrodes is created with this configuration (Fig.4.11(b)). Fig.4.12 shows the photocurrents of such detectors with different light input power levels. The measured transmission changes between off-state and 5-volt-on-state for the detectors without fingers were also measured. Fig.4.13 is a typical response and Table 4.1 gives the measured data. Compared with the transmission change for the detectors with fingers, we can draw a conclusion on a statistical basis that the detectors without any fingers may have a larger percent of transmission increase when shifted from on-state to off-state than the detectors with fingers.

Overall, the Franz-Keldysh effect does work in our device and could be employed to broaden the operating wavelength for our detectors. It is expected that the electroabsorption effect would be considerably larger in quantum well structures, where it is called quantum-confined Stark effect.
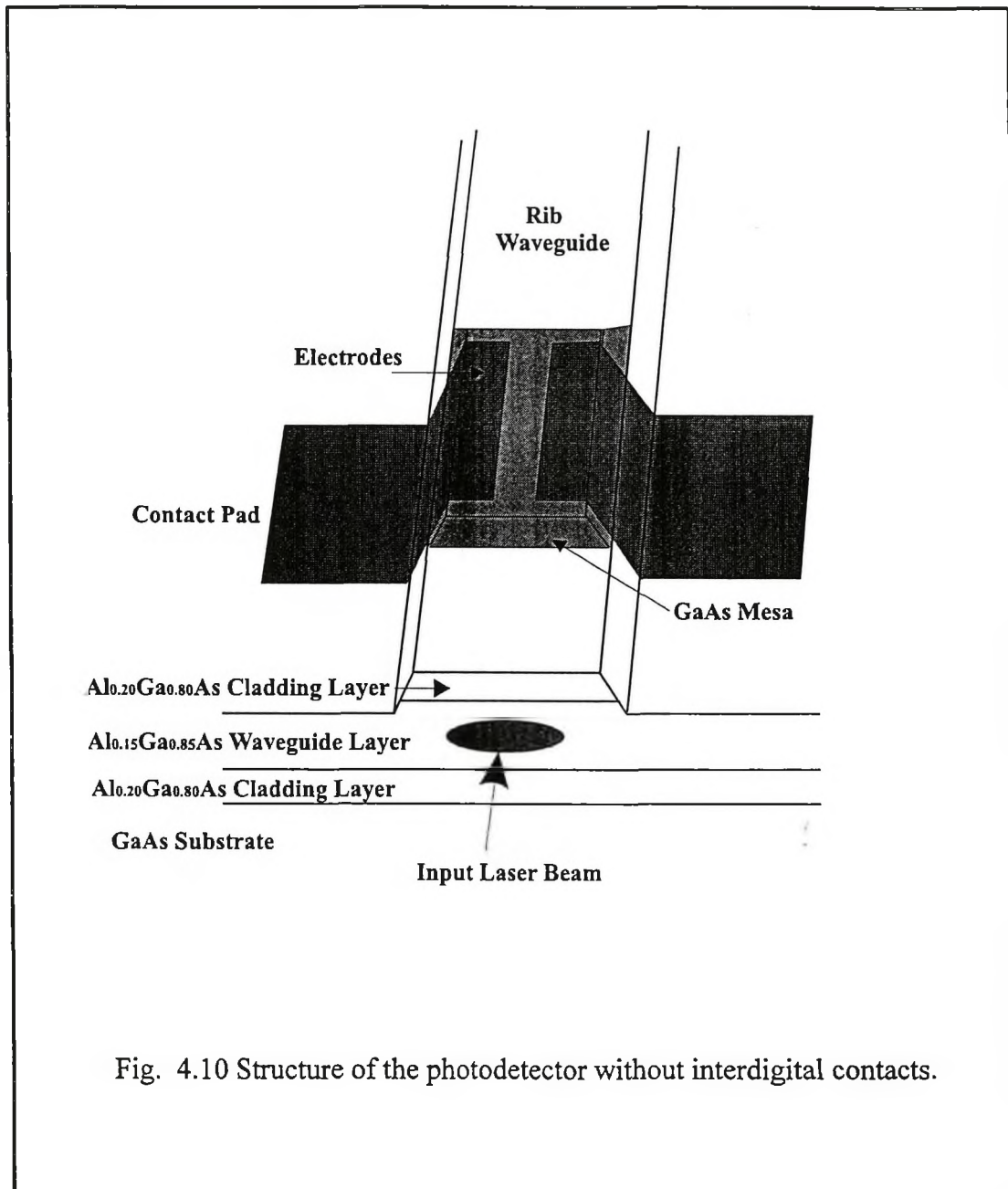
Fig. 4.10 Structure of the photodetector without interdigital contacts.
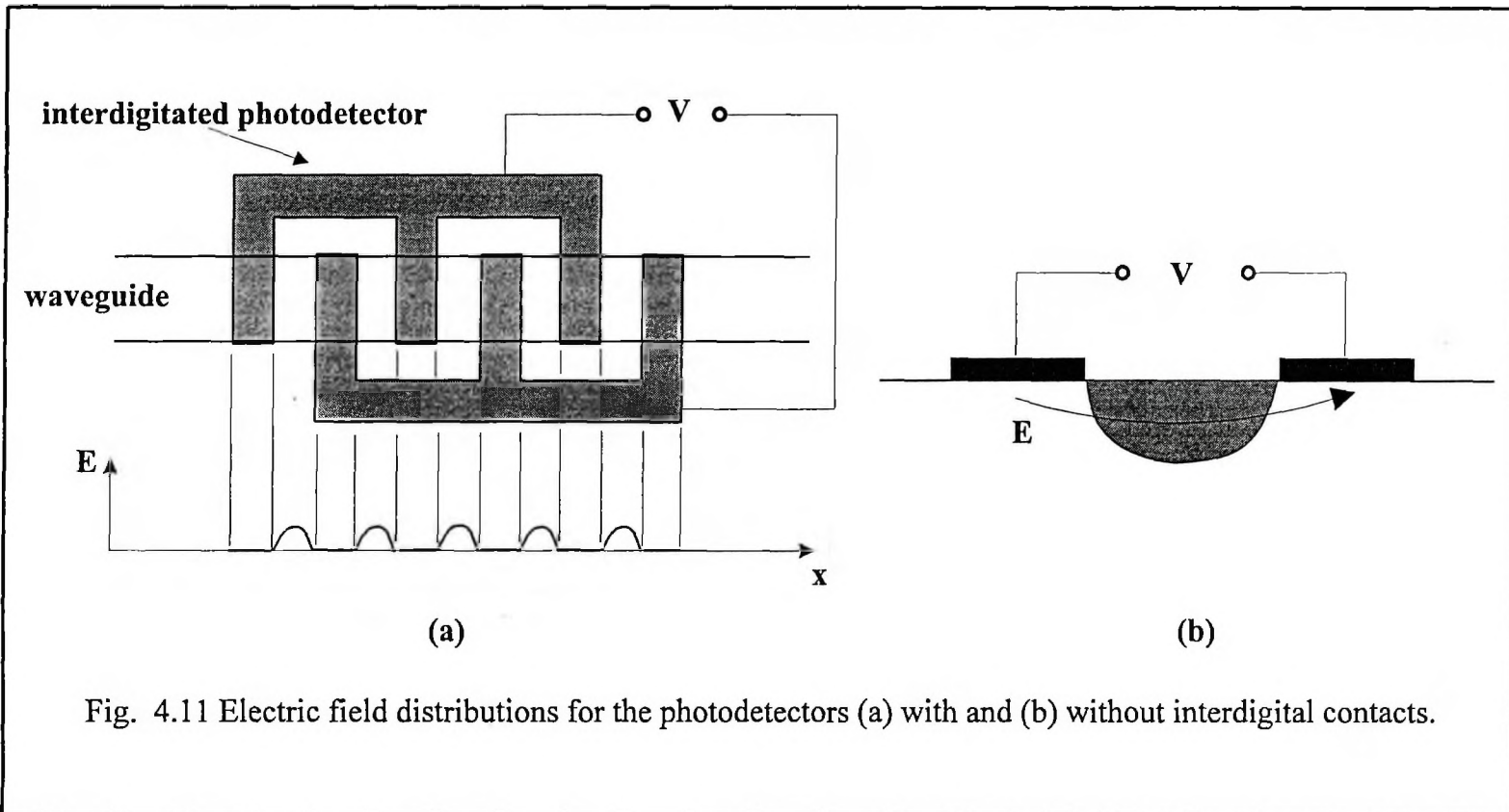
Fig. 4.11 Electric field distributions for the photodetectors (a) with and (b) without interdigital contacts.
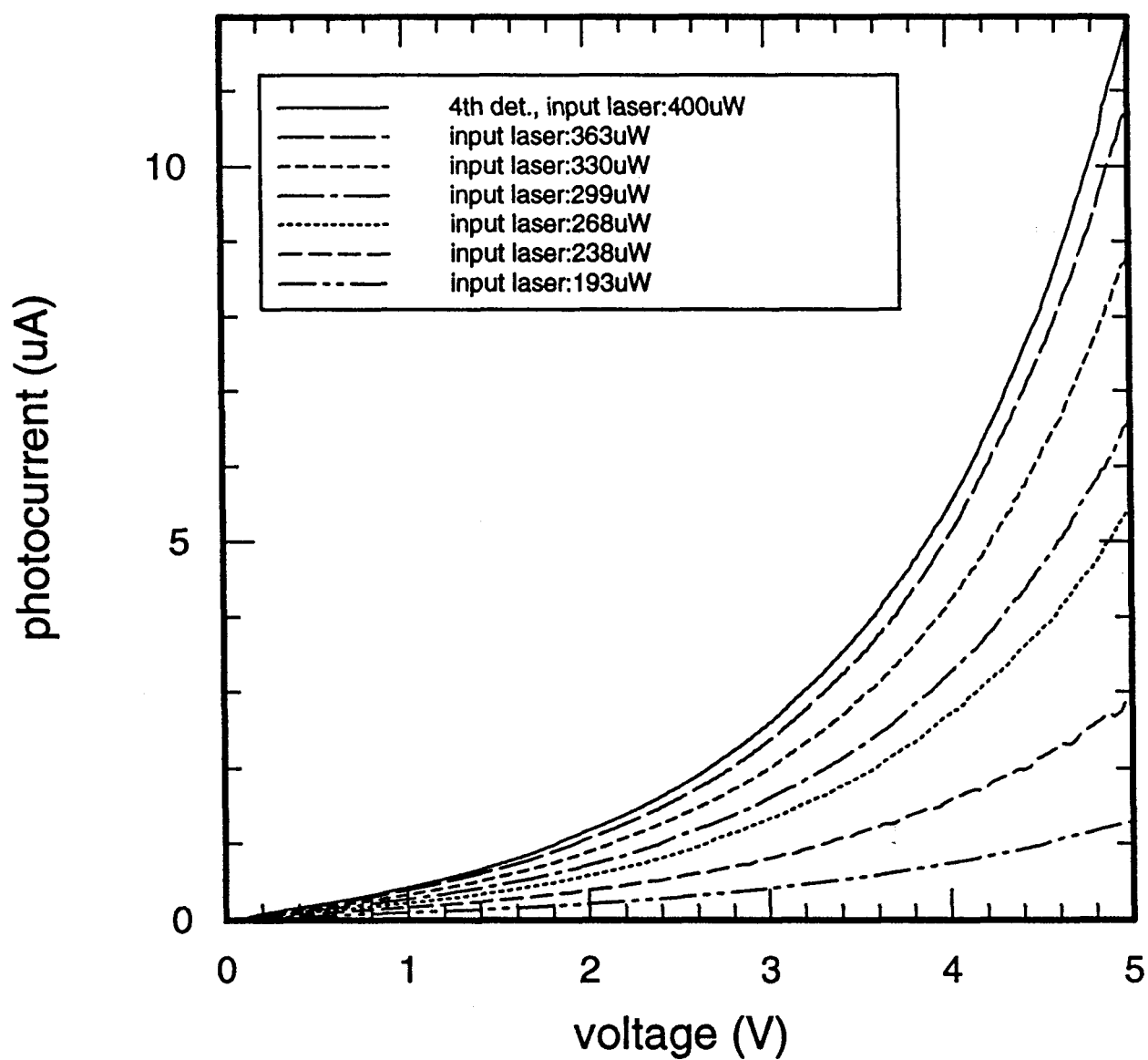
**Figure 4.12** I-V characteristics of the photodetector without interdigital contacts as a function of bias voltage for a series of input power levels at 890nm.
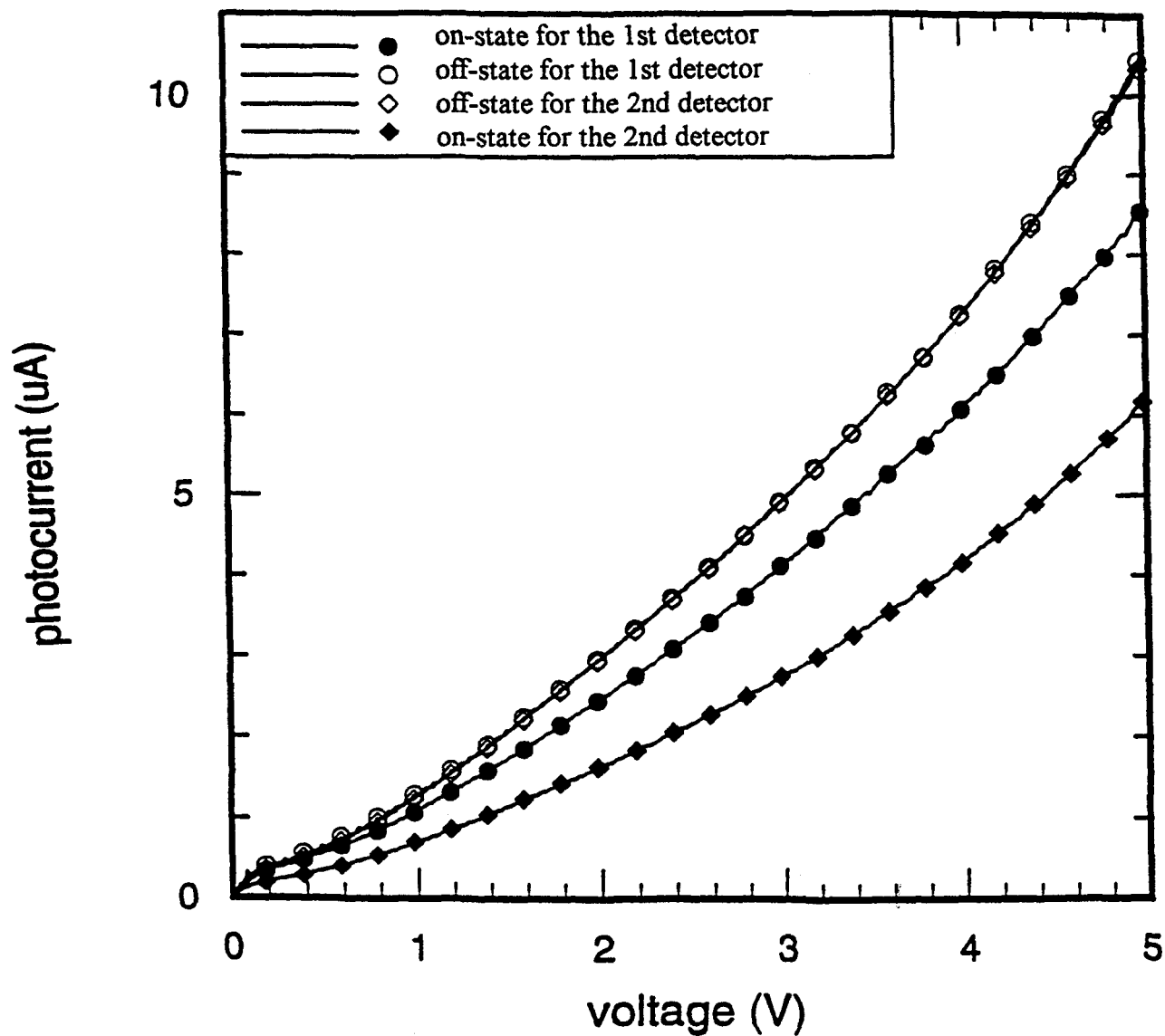
**Figure 4.13**  Photocurrent vs. bias voltage in the third detector for different bias conditions (on and off-states) in the first and second detectors at 890nm for the case that the photodetectors are without interdigital contacts.

# Chapter 5 The Potential for a Wavelength Monitor Based on In-line Photodetectors

## 5.1 Introduction

Both theoretical calculations and experimental measurements [5.1, 5.2] show that the detector response can be voltage-tuned for wavelengths near the absorption band edge due to Franz-Keldysh effect. An electric field shifts the absorption edge toward the red. We confirmed this in our device in Chapter 4. As the band edge shifts, the absorption coefficients at either side of the edge change: for photon energies less than the band edge energy $E_g$, the absorption coefficient increases with the electrical field, while for photon energies greater than $E_g$, there is a slight decrease of the absorption coefficient.

Consider the responses of two adjacent inline detectors in our device. A fraction of the input light is absorbed in the first detector while the remainder is transmitted through it and reaches the second detector. The first detector in the series acts like a filter which filters the light that reaches the second. For wavelengths near the absorption band edge the ratio of the second detector's photocurrent to that of the first is a function of wavelength. It increases as the waveguide's absorption coefficient decreases. There also is a variation of the absorption coefficient with electric field. Therefore, it would be interesting to see how this ratio changes with applied electric field at different wavelengths on either side of the GaAs absorption edge.

For both detectors the photocurrent is proportional to $P_i(1-e^{-\gamma\alpha(\lambda)L_i})$ where $P_i$ is the the input power to the front (i=1) or back (i=2) detector, $\gamma$ is the relative confinement factor of the waveguide mode to the detector layer, $\alpha(\lambda)$ is the wavelength and voltage dependent absorption coefficient and $L_i$ is the length of the detector. The ratio of the photocurrent of the second detector to that of the first one is therefore,

$$ratio = \frac{I_2}{I_1} = \frac{P_2(1-e^{-\gamma\alpha L_2})}{P_1(1-e^{-\gamma\alpha L_1})} \tag{5.1}$$

Assume that the attenuation in the passive waveguide section, or the power loss in between the two detector sections is so small compared with that in the detector section that it can be neglected. The power reaching the back detector is $P_2=P_1 e^{-\gamma \alpha L_1}$. So,

$$ratio = \frac{e^{-\gamma \alpha L_1}(1-e^{-\gamma \alpha L_2})}{(1-e^{-\gamma \alpha L_1})} \qquad (5.2)$$

If the two detectors are of the same length, $L_1=L_2=L$, the ratio of the back to the front detector's photocurrent is simply $e^{-\gamma \alpha L}$.

For wavelengths near the absorption band edge, this ratio could be used as a wavelength monitor due to the wavelength dependence of the absorption coefficient.

In practical uses such as fiber optic strain sensor systems based on optical fiber Bragg gratings where strain in the structure results in small changes in the fiber length and a corresponding shift in the centre wavelength of the grating's reflection band, changes in the wavelength have to be monitored. Now there is a growing interest in the use of optical fiber Bragg gratings in strain sensor systems [5.3, 5.4] where wavelength monitors are employed.

## 5.2 Experimental Results

We performed additional tests on the devices to evaluate their potential as wavelength monitors. At first, using two semiconductor diode lasers, we measured the photocurrent ratio at 820nm where the photon energy is above the GaAs band gap and at 890nm where it is below the band gap. Then we used a tunable titanium: sapphire laser pumped by an $Ar^{++}$ laser to probe the ratio response for the inline detectors at wavelengths between 820 and 890nm.

A monochromator was calibrated with a He-Ne laser at the wavelength of 6328Å and then was used to calibrate the dial reading of the Ti:Sapphire laser. Fig.5.1 shows the dial number of the Ti:Sapphire laser vs. the corresponding output wavelength. The output from the tunable laser at different wavelengths is illustrated in Fig.5.2.

Fig.5.3 shows the experimental set up. The laser light was coupled into the waveguide through
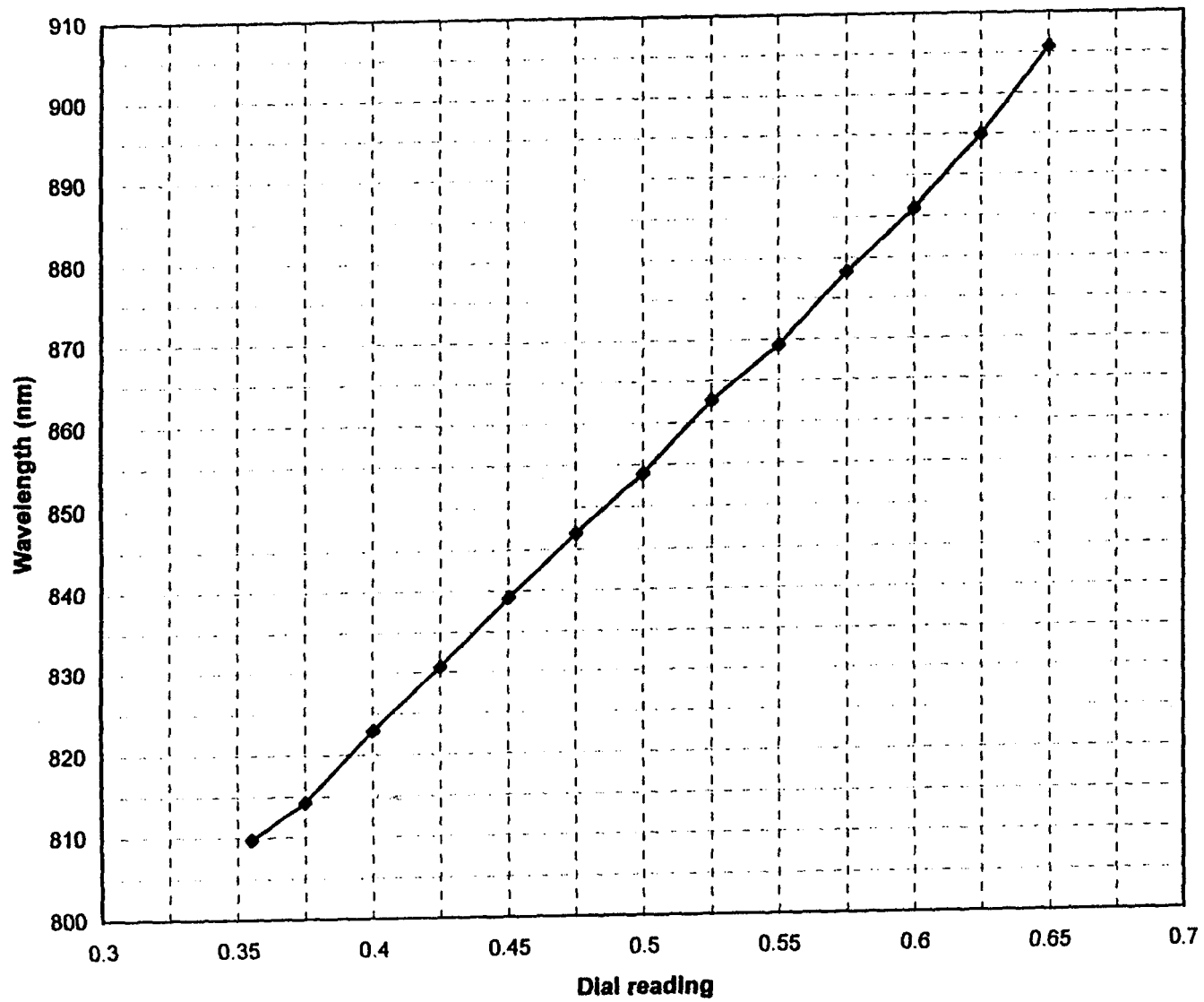
**Figure 5.1** Ti:Sapphire laser dial reading rectification.
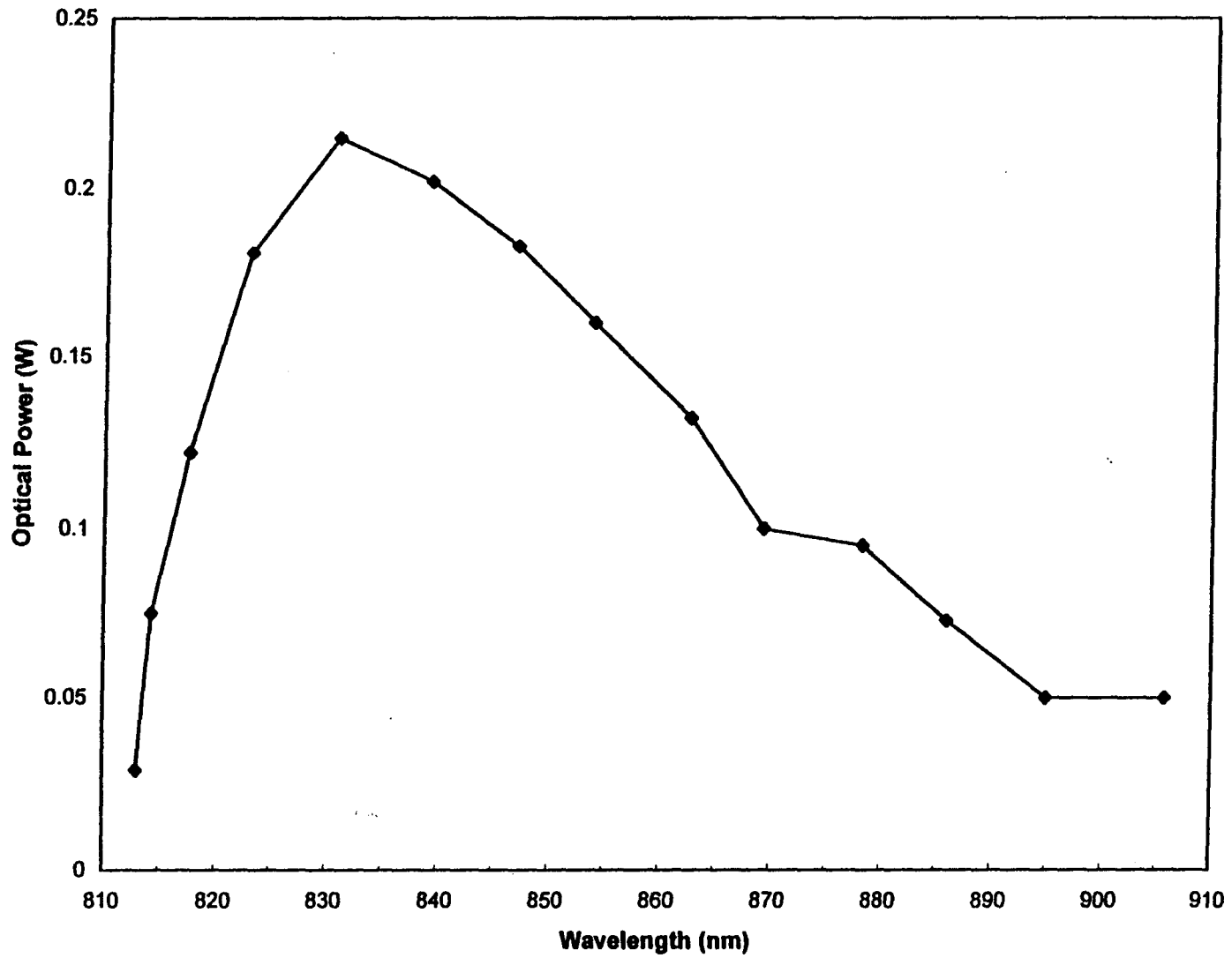
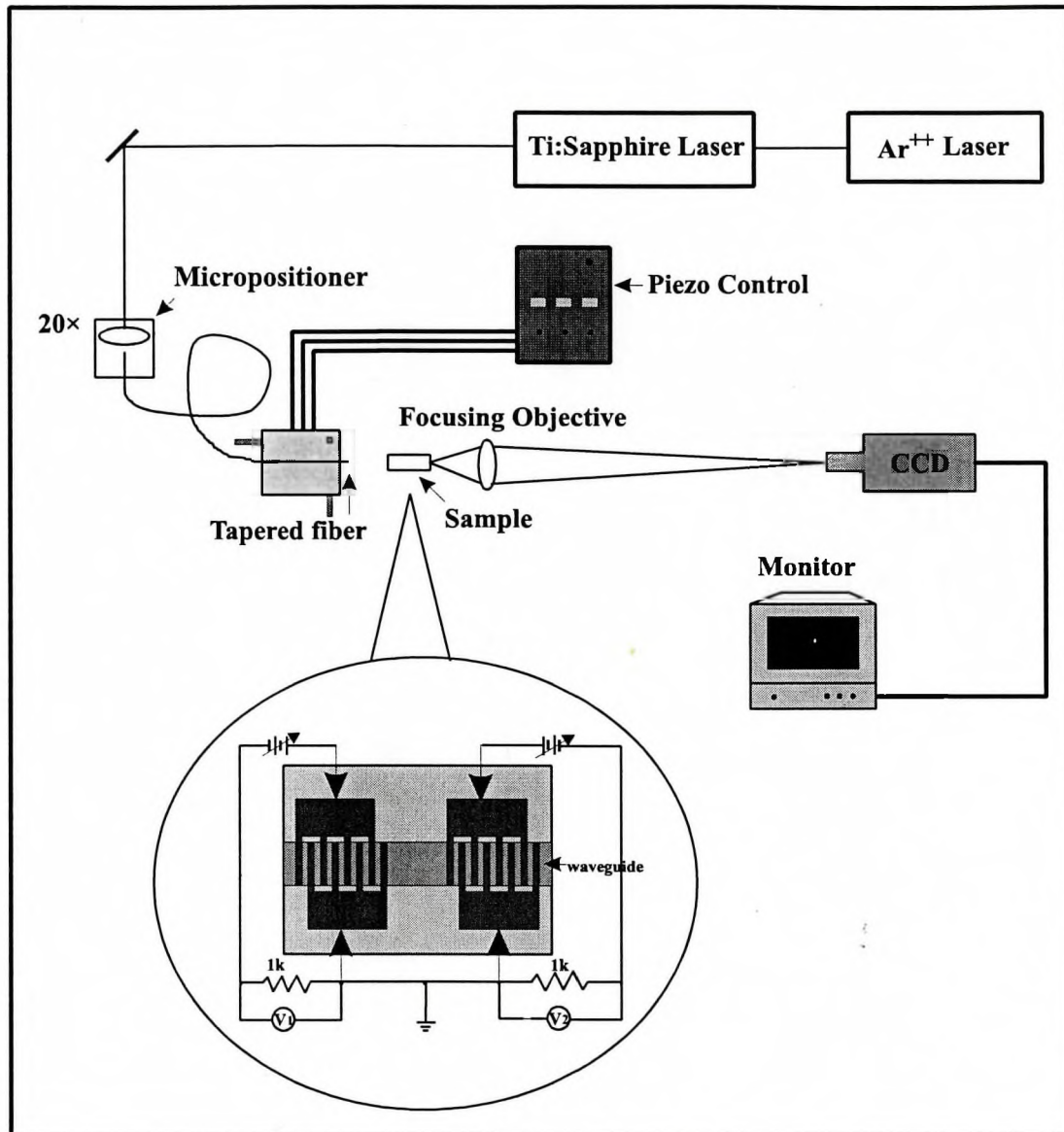**Figure 5.2** The output power level of Ti:Sapphire laser at different wavelengths.

Fig. 5.3 Experimental set-up for the measurement of the photocurrent ratio of the 2nd in-line photodetector to the 1st photodetector.

a tapered optical fiber. Each detector was biased using a separate circuit to avoid electrical current crossing from one circuit to the other. The two electric biasing circuits have a common ground. The detectors were biased with different voltages through 1kΩ resistors, and the photocurrents were determined from the voltages generated on the 1kΩ resistors. The ratio of the photocurrents in adjacent detectors were taken while the bias voltages on them were the same.

We did the measurement on two kinds of inline detectors: for the first kind, the detectors are the first two on the 10-μm waveguide with lengths of 45 and 67 μm, respectively, and a separation of about 900μm; the second is two adjacent detectors of the same length of 100 μm, and 10-μm separation in between. The measurement of the photocurrent ratio at the wavelengths of 823, 850, 873 and 896nm are shown in Figure 5.4 and 5.5 for the two cases, respectively.

From the measurement we see that at shorter wavelengths where the photon energy is greater than the band gap energy, the ratio goes up with the bias voltage; whereas at longer wavelengths, the ratio goes down as the bias increases. The average of the ratio difference at longer wavelengths is usually bigger than that at shorter wavelengths as the bias is increased by 1V. At the higher bias voltages the band edge transition becomes more gradual. The average ratio difference per Volt is the biggest at 873nm which corresponds to GaAs absorption band gap at zero-bias field.

It should be mentioned that there are fluctuations in the photocurrent during the measurement which are usually about 0.5% ~ 1%. The data shown in Figure 5.4 and 5.5 are the median or average readings with dark current subtracted.

Since our device is not a quantum well device, the transition is limited by both the degree of red shift and the abruptness in the absorption edge, thus it is not ideal for real applications. In quantum well photodetectors where the quantum confined Stark effect can be employed, a large energy shift occurs due to the major change in potential well. The tunable range can be 20nm, 30nm or more [5.5, 5.6]. For a fixed wavelength, the change in absorption coefficient with is much greater in the quantum well devices than in bulk semiconductors. The absorption band edge transition is much sharper and the location of the transition can be precisely spotted and tuned. In this case, wavelength selective detectors can be made for use in optical communications and sensitive wavelength monitors.
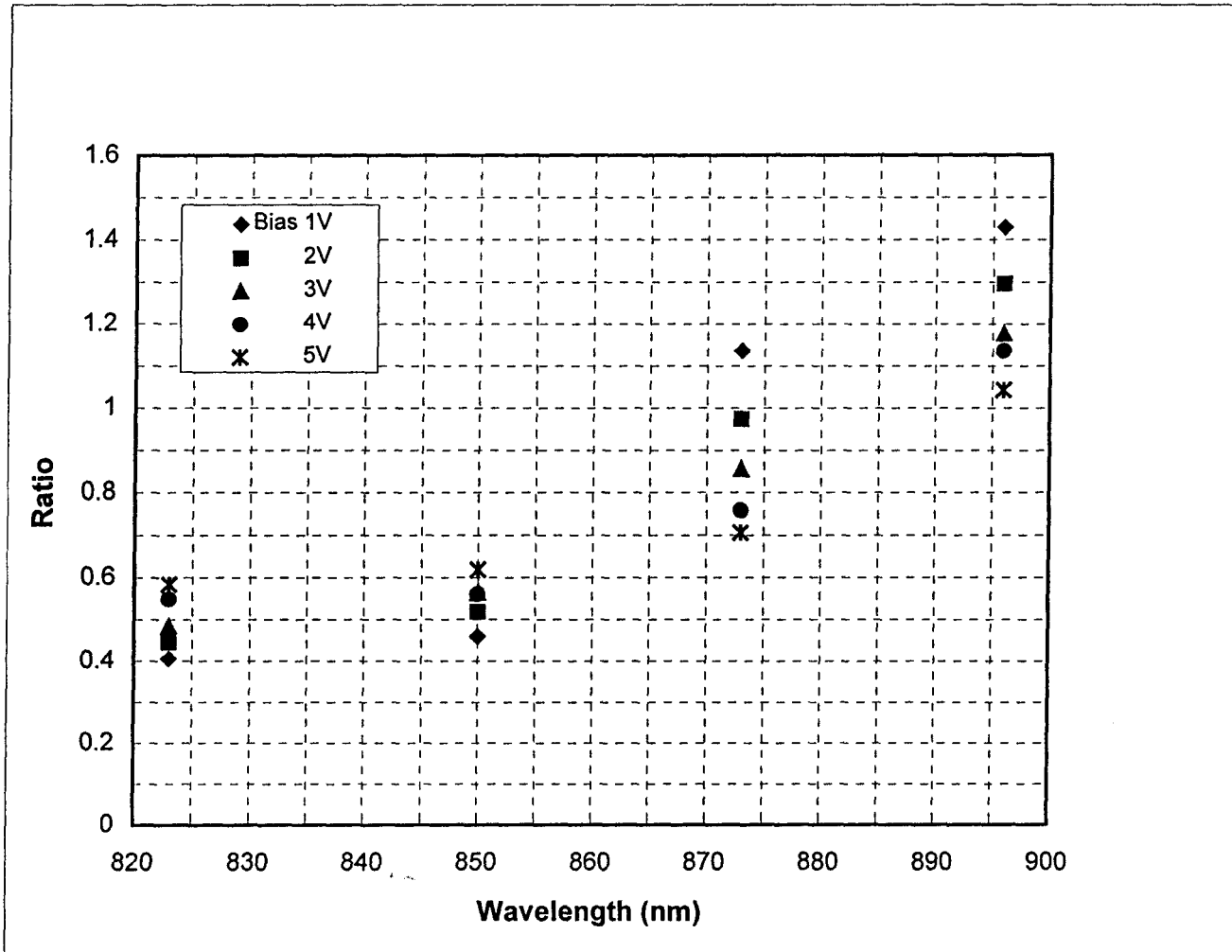
Figure 5.4  Photocurrent ratio of the second detector to the first on the 10-µm waveguide at different bias voltages and different wavelengths
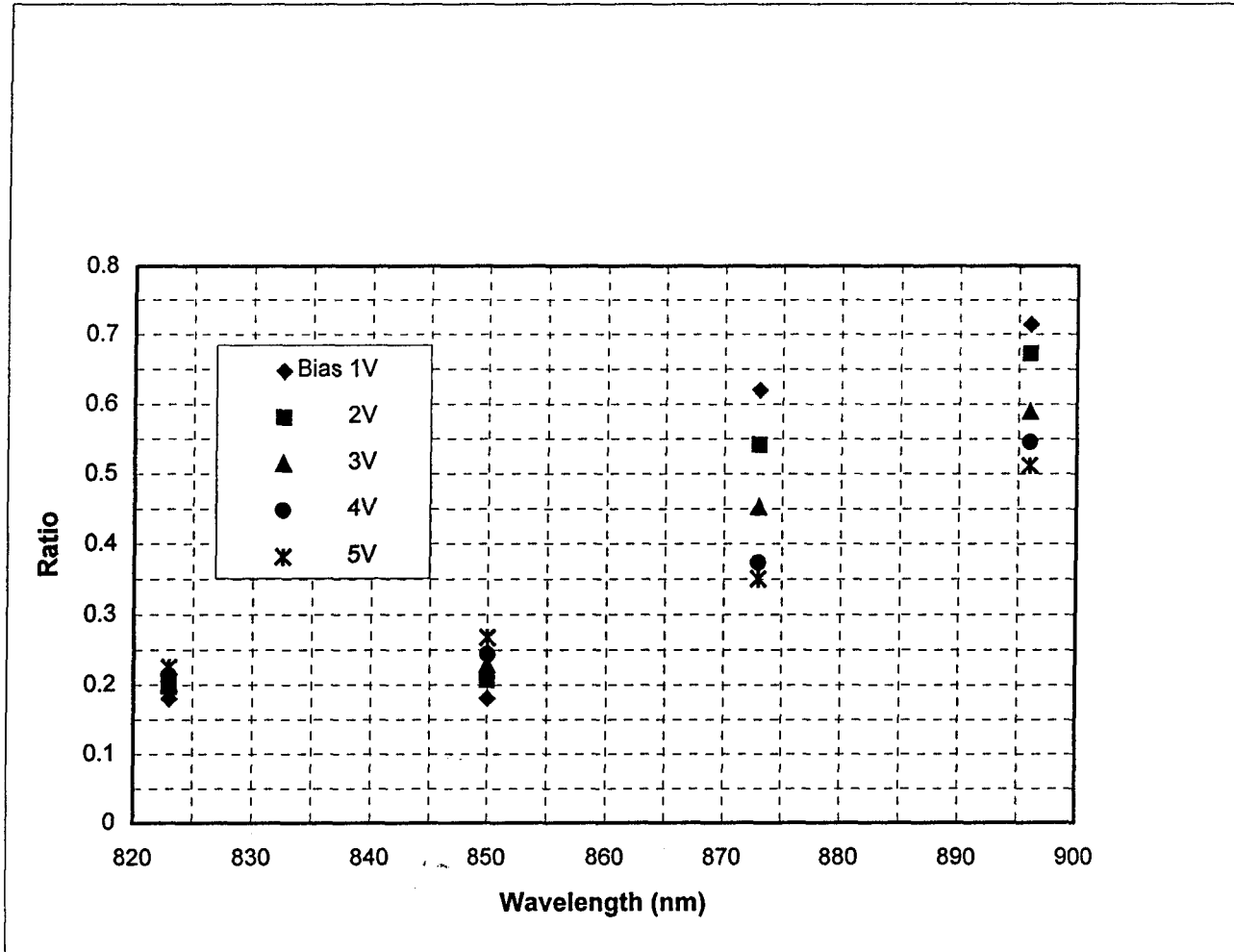
Figure 5.5  Photocurrent ratio of the second detector to the first for the adjacent detectors
at different bias voltages and different wavelengths

## Chapter 6  Crosstalk Between Detector Elements

### 6.1 Introduction

Crosstalk from electromagnetic coupling increases with frequency, so it is difficult to design conventional (non-optical) matrix switches for high frequency electronic signals. Good promise has been shown for high isolation matrices to handle signals in the dc to 10GHz range when a hybrid technique is used to exploit passive optical-signal distribution and switching by optoelectronic effects [6.1]. The key elements for such optoelectronic switches are optical detectors that have switchable sensitivity.

Theoretically speaking, because the signal energy is largely confined to its optical paths, signal cross coupling in such a matrix can be very low. The possible parasitic cross coupling exists only among the electrical output lines. They are interconnected by dielectric optical waveguide paths; thus, in principle, can be isolated to any required degree by shielding.

However, in real devices, there can be various causes of crosstalk such as electrical current leakage from the electrodes of one detector to those of another, detector's absorption of scattered light, mode coupling or mode interference between waveguides or detectors. These can be generated due to the proximity of the detectors or the waveguides, incomplete mode confinement in the waveguides or the mesas of the detectors, improper grounding, a large concentration of doping or background doping, different biases on the detectors, improper biasing circuits, improper etching depths of the mesas or waveguides, etc.

Due to the complexity of crosstalk measurement in real device, we simply attribute the crosstalk between the inline detectors as electrical crosstalk which is denoted by $X^E$, while that between waveguides as optical crosstalk denoted by $X^O$.

### 6.2 Electrical crosstalk

Theoretically, there should be no photocurrent output if there is no bias on the MSM detector

even if it is illuminated [6.2]. According to the analytical model of bias dependence of the photocurrent of MSM photodetectors presented in Chapter 2, the photocurrent is based on drift collection of carriers in the depletion regions of the cathode and anode and diffusion and recombination of carriers in the undepleted region. For small values of bias voltage, equal numbers of holes can diffuse to the anode or cathode and the device becomes almost symmetrical. The overall drifting effect of the photogenerated carriers is zero without any bias if the MSM is perfectly symmetrical. That is, the current becomes zero when no bias is applied.

However, since there exists electrical current leakage from the contacts of the biased detector to that of the adjacent unbiassed detector, an "effective bias" could be introduced onto the originally unbiassed adjacent detectors, hence the photocurrent output from them. We refer to the crosstalk due to the current leakage between the contacts of different detectors as electrical crosstalk.

Crosstalk in this case is defined as the signal level received from an unbiassed detector adjacent to a biased one [6.1]. In decibles, it is given by:

$$X^e_{jk} = 10\log(I_k^2 / I_j^2) \qquad (6.1)$$

which refers the crosstalk on detector k due to detector j. $I_k$ is the photocurrent in detector k. Here we use square of the photocurrent because it is proportional to the electrical power it generated.

In our experiment, the crosstalk was measured as the signal level of the unbiased 2nd, 3rd or 4th detector to the biased first in-line detector (Table 6.1).

Table 6.1  Crosstalk level between the first on-state detector

to the other off-state in-line detectors

| Unbiased in-line detector | 2nd | 3rd | 4th |
|---|---|---|---|
| crosstalk (dB) | ~30 | ~35 | ~38 |

From the measurements obtained, we can see that the level of crosstalk is dependent on the proximity of the two detectors and could therefore be improved.

When we consider the leakage going from the contact of the biased detector to that of an unbiased in-line detector, we may refer the effective resistance between them as $R_{eff}$. When an electric field is present in a semiconductor, charge transport (electrical current) is observed. The two metallic contacts on two different detectors with different bias act as if connected by a resistor (Fig.6.1) [6.3]. The farther the distance between them, the larger the resistance. Smaller effective resistance results in a lowered electric field across the receivers which reduces the response of the receiver when these defective crosspoints are in the ON-state.

## 6.3 Optical Crosstalk

In order to meet the needs of coherent communications systems, most photonic integrated circuit (PIC) applications require single-moded waveguide structures. Typically these waveguides are either strip-loaded[6.4, 6.5], deeply etched [6.6] or buried heterostructure designs [6.7]. Conventional strip-loaded rib waveguides support guided slab modes outside the actual rib resulting in high crosstalk between adjacent guides. In some cases, the optical mode is not confined to the waveguide into which the laser beam is coupled, which causes crosstalk between the waveguides. Also, when a wavelength is used other than the one for which the single-mode-waveguide structure is designed, optical field diffraction or multi-mode propagation may occur, which results in the optical crosstalk. Scattered light may cause crosstalk in the adjacent waveguides as well.

In measuring the crosstalk between the waveguides, we biased the first detector at on-state on the waveguide that was adjacent to the illuminated waveguide, checked its photocurrent and took crosstalk as the ratio of its photocurrent to the detector on the illuminated waveguide. The values are around 40dB.

## 6.4 Discussion and Ways of Reducing the Crosstalk

For crosstalk in an actual device, the distribution between electrical and optical crosstalk is more complicated than we suggested above. You cannot simply call everything between different waveguides "optical" and everything between inline detectors on the same waveguide "electrical". There could be scattered optical signal absorbed by inline detectors in addition to the absorption of direct coupling. And the electrical crosstalk could be across the various waveguides as well. If the adjacent pads of the two different detectors on adjacent waveguides have different bias voltages, there will exist electrical current leakage between them, hence some electrical
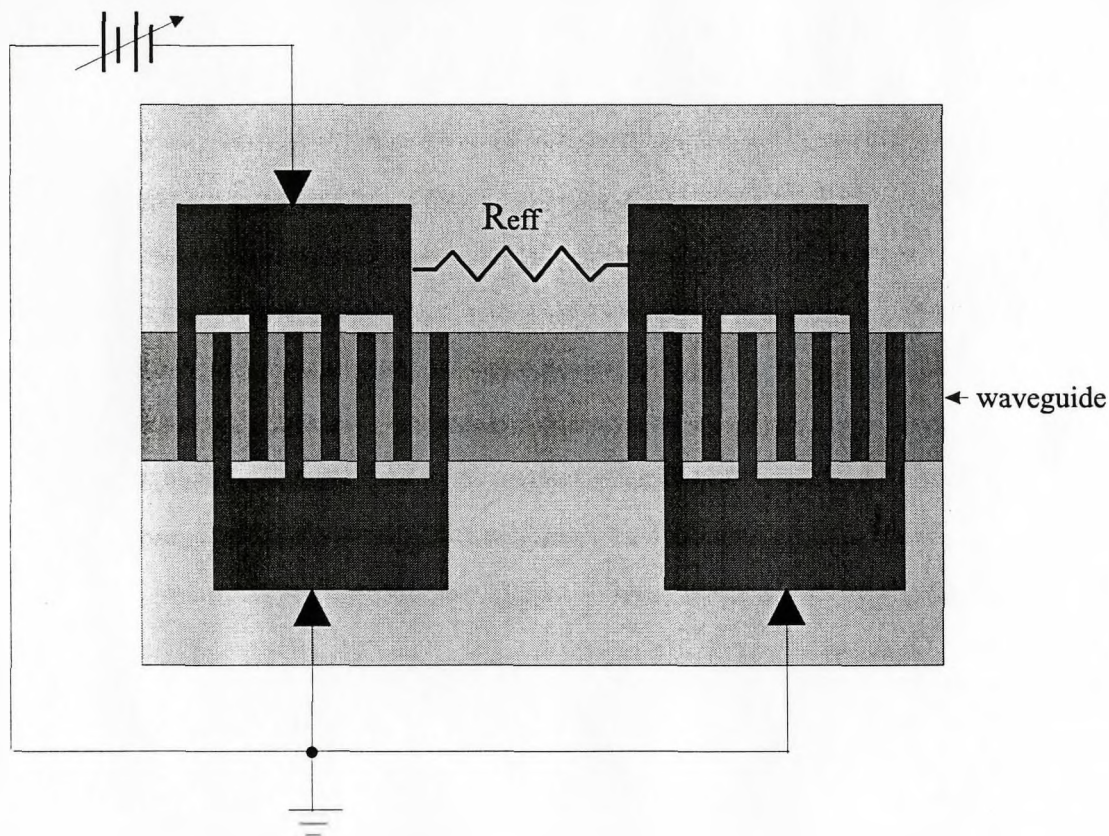
Fig. 6.1 Current leakage from one contact of a detector to that of the adjacent detector due to different bias states.

crosstalk in this situation.

What is required is to determine the electrical crosstalk first, and then measure the optical crosstalk in a way that minimizes or eliminates the electrical crosstalk.

To reduce the electrical and optical crosstalk, we suggest the following methods:

1. Bias the adjacent contacts of different inline detectors and/or detectors in different waveguides at the same voltages if possible (Fig.6.2). If the adjacent contacts are biased at the same potential, you can come close to eliminating the electrical crosstalk, while characterizing the optical crosstalk.

2. Add a grounded shield between the detectors (Fig.6.3). In this case, most of the leakage will go to the grounded shield instead of the adjacent contacts of other detectors if they have a different bias. The provision of a ground plane fabricated monolithically with the array isolates each individual detector, which can be an important factor in reducing the electrical crosstalk.

3. Properly coat the tapered fiber so that the scattered light could be reduced.

4. Etch deep trenches between the mesas of the detectors down to waveguide layer so that the optical modes can be largely confined to the waveguide. Etching trenches on either side of the rib to form a cutoff mesa can also provide electrical isolation as well [6.8].

But be aware that unless the trenches go far past the intrinsic layer of the device (and often even if they do), anytime you put a potential on one of the top contacts that differs from the potential on a neighbouring contact, a portion of any current through the detector will route through the adjacent top contact rather than the one you want. If the device is entirely intrinsic, the situation could be better, all depending on what the background doping levels are of course). How much of a problem this is will depend somewhat on how much light you have. Unless you have a lot, those erroneous currents (crosstalk) are going to overwhelm the signal.

## 6.5 Isolation

When a voltage is applied to a metal-semiconductor-metal (MSM) photodetector consisting of interdigitated metal contacts deposited on semiconductor substrates to form Schottky barriers,
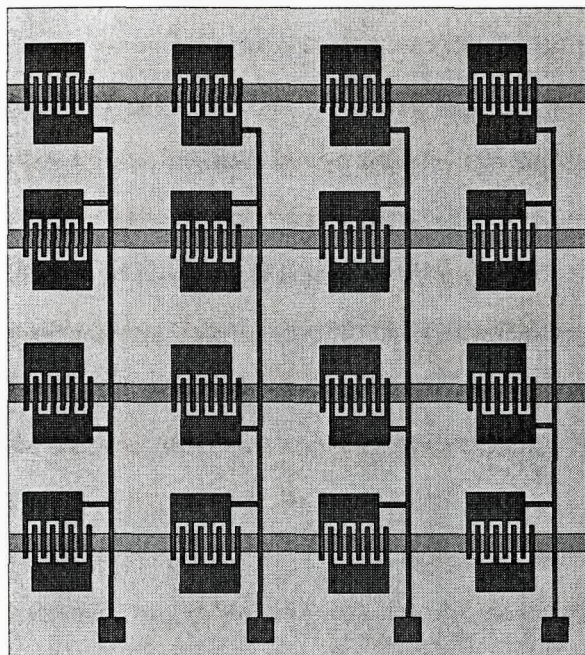
**Figure 6.2** Biasing scheme for the matrix switch to reduce electric crosstalk by reducing the current leakage between the contacts of different detectors. (Electrodes are put onto the contacts of the detectors directly.)

one of the barriers is under forward bias and the other is reverse biassed and acts as a photodiode whose depletion region spans the channel between contacts.

The effectiveness of an optoelectronic switch is measured by its isolation which is defined as the ratio of the electrical power of the received signal when the switch is in the on-state to the power received when it is in the off-state. The near absence of built-in electric fields in the device structure allows for an unbiased off-state in which the residual response can only be caused by diffusion of the photocarriers to the electrodes. This carrier diffusion process to the electrodes is quite small, mainly due to the distance separating the channel from the contacts, and is usually symmetrical. So isolation in MSM switches is dependent on an accurate balance between the opposing photovoltages at the two contacts when the device is unbiassed. MSM optoelectronic
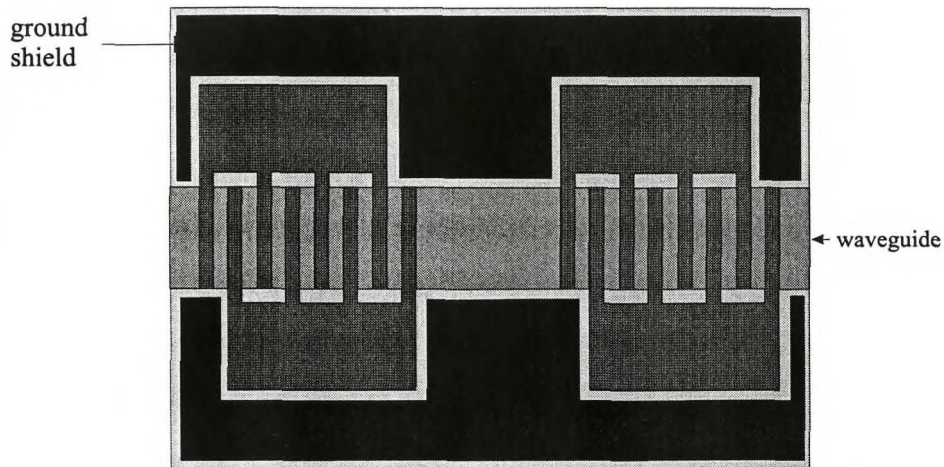
Fig. 6.3 Add a ground shield between the detectors to reduce the
electrical crosstalk.

switches have typically 50dB of isolation, whereas up to 70dB is obtained in photoconductors [6.9, 6.10]. However, this isolation level is quite sensitive to any residual electric field that may occur across the device.

The isolation of a typical 50μm-long detector in our device varies from 40dB at low frequencies to 20dB at 3GHz [6.11]. But even if every individual MSM detector is perfectly symmetrical, with a considerable crosstalk between them, you could not get a very low response for the off-state detectors, and thus the effectiveness of the device is lowered.

# Chapter 7  Conclusion

In this thesis, we reported the performances of AlGaAs waveguide-coupled GaAs metal-semiconductor-metal (MSM) photodetectors and a 4×4 optoelectronic matrix switch in which the photodetectors were designed for signal distribution.

The power delivered to multiple detectors that are placed in-line on a single AlGaAs waveguide can be balanced by varying the detector lengths along the propagation direction and by controlling the degree of coupling between the waveguiding and absorbing layers, or by using Franz-Keldysh effect.

Both theoretical calculations and experimental measurements confirmed that the coupling between the waveguiding and absorbing layers is enhanced when the higher mode is slightly above cut-off. This helps us design waveguide-coupled detectors that can tap off a controlled fraction of the guided optical power, which is very important for large-scale matrix switches.

If the device is operated at the wavelength whose energy is below the GaAs bandgap such as 890nm, the Franz-Keldysh effect becomes important. It was observed that the absorption is increased at higher-biased state compared with lower-biased state. The detector's transmission is increased by 10-30% if the detector is shifted from on-state to off-state. Using Franz-Keldysh effect would allow control over how much light can be absorbed and would overcome the difficulty in tailoring the absorption coefficient to a specific value. This would make the fabrication of large scale array systems more practical.

Since the detector exhibits a transition for wavelengths near the absorption band edge due to Franz-Keldysh effect, the first detector in a inline series detectors can act as a filter. In our work, the responses of two adjacent inline detectors were measured and the ratio of the two were taken. Conclusion shows that the inline detectors could serve as a wavelength monitor.

Crosstalk was also analysed in terms of electrical and optical crosstalk. Proposals for improvement were suggested such as etching trenches beside the mesa, adding a grounded shield between the detectors, etc.

For the work that can be done in our system in the future, as the Franz-Keldysh effect and wavelength monitor are concerned, quantum well materials are suggested in which case the field-induced change in the absorption coefficient can be at least as much as 50 times that of the current non-quantum-well materials. However, fabrication techniques required to make these materials are comparatively expensive and yet not perfect. For the whole system, the goal is to obtain a waveguide-coupled MSM photodetector matrix switch with large scale, large bandwidth, high speed and smaller bit-error rate by using bulk materials.

The driving force for photonic integrated circuits is the expected complexity of next-generation optical communications links, networking architectures, and switching systems. The simplicity and speed of MSM photodetectors have made them the prime candidates for integration in optoelectronic circuits. The optoelectronic integrated circuit will evolve as basic hardware which will be used for information processing systems in the next century.

# REFERENCES

[1.1] E.M.Wright, R.J.Hawkins, and R.J.Deri, "Coupled-mode theory of vertically integrated impedance-matched waveguide/photodetectors", Opt. Commun., vol.117, pp.170-178, 1995.

[1.2] W.K.Chan, J.H.Abeles, K.C.Nguyen, R.Bhat, and M.A. Koza, "Integration of high-speed optical taps with InP waveguides", IEEE Photon. Technol. Lett., vol.1, pp.65-67, 1989.

[1.3] R.J.Deri, W.Doldissen, R.J.Hawkins, R.Bhat, J.B.D.Soole, L.M.Schiavone, M.Seto, N.Andreadakis, Y.Silberberg, and M.A.Koza, "Efficient vertical coupling of photodiodes to InGaAsP rib waveguides", Appl. Phys. Lett., vol.58, pp.2749-2751, 1991.

[1.4] N.Emeis, M.Schier, L.Hoffman, H.Heinecke, and B.Baur, "High speed waveguide-integrated photodiodes grown by metal organic molecular beam epitaxy", Electron. Lett., vol.27, pp.344-345, 1992.

[1.5] J.Soole, Y.Silberberg, A.Scherer, H.Leblanc, N.Andreadakis, C.Caneau, J.Schumacher, and U.Erben, "Fast high-efficiency integrated waveguide photodetectors using novel hybrid vertical/butt coupling geometry", Appl. Phys.Lett., vol.61, pp.13-15, 1992.

[1.6] M.Veilleux and R.I.MacDonald, "An optoelectronic switching matrix with high isolation", IEEE J. Lightwave Technol., vol.10, pp.988-991, 1992.

[1.7] W. Ng, D.Yap, A. Narayanan, R.Hayes, and A.Walston, "GaAs optical time-shift network for steering a dual-band microwave phased array antenna", Optical Technology for Microwave Applications VI and Optoelectronic Signal Processing for Phased-Array Antennas III, S-K, Yao and B.M.Hendrickson, eds., Proc. SPIE 1703, pp.379-383, 1992.

[1.8] W. Ng, D.Yap, A. Narayanan, and A.Walston, "High-precision detector-switched monolithic GaAs time-delay network for the optical control of phased arrays", IEEE Photon. Technol. Lett., vol.6, pp.231-234, 1994.

[1.9] N.Uesugi, S. Machida, and T. Kimura, Opt. Quantum Electron. 15, 217 (1983)

[1.10] M. Ito, O. Wada, K. Nakai, and T. Sakurai, "Monolithic integration of a metal-semiconductor-metal photodiode and a GaAs preamplifier", IEEE Electron Device Lett., vol. EDL-5,pp.531-532, 1984.

[1.11] H.Hamaguchi, M.Makiuchi, T.Kumai, and O. Wada, "GaAs optoelectronic integrated receiver with high-output fast-response characteristics", IEEE Electron Device Lett., vol.EDL-8, pp.39-41, 1987.

[1.12] W. Roth, H.Schumacher, J.Kluge, H.J.Geelen, and H.Beneking, "The DSI diode -A fast large-area optoelectronic detector", IEEE Trans. Electron Devices, vol. ED-32, pp. 1034-1036, 1985.

[1.13] C. Moglesture, J. Rosenzweig, J. Kuhl, M. Klingenstein, M. Lambsdoff, A. Axmann, J.Schneider, and A. Hulsmann, "Picosecond pulse response characteristics of GaAs metal-semiconductor-metal photo detectors", J.Appl. Phys., vol.70, No.4, pp.2435-2448, 1991.

[1.14] M.Ito, and O.Wada, "Low dark current GaAs metal-semiconductor-metal (MSM) photodetectro using Wsix contacts", IEEE J. Quan. Electron., QE-22, pp.1073-1077, 1986.

[1.15] D.S.Malhi, J.M.Xu, F. Hegmann, B. Takasaki, and R.Surridge, "Effects of material modification on dark current of GaAs MSM photodetectors", in Semi-Insulating III-V Materials, A.G.Milnes and C.J.Miner, Eds. Philadelphia, PA, Toronto, Canada: Hegler, 1990, pp.451-456.

[1.16] D.L.Rogers, "Monolithic integration of a 3-Ghz detector/preamplifier using a refractory-gae, ion-implanted MESFET process", IEEE Electron Device Lett., vol.EDL-7, pp.600-602, 1986.

[1.17] C.W.Slayman and L.Figueroa, "Frequency and pulse response of a novel high speed interdigital surface photoconductor (IDPC)", IEEE Trans. Electron Devices Lett. EDL-2, pp.112-114, 1981.

[1.18] T.Sugeta, T.Urisu, S.Sakata, and Y.Mizushima, "Metal-semiconductor-metal photodetector for high speed optoelectronic circuits", Jpn. J. Appl. Phys., Suppl.19-1, vol.19, pp.459-464, 1980.

[1.19] J.B.Soole and H.Schumacher, "GaAs metal-semiconductor-metal photodetectors for long wavelength optical communications", IEEE J.Quan. Electron., vol.27, pp.737-752, 1991.

[1.20] S.Kawanishi, Y.Yamabayashi, T.Takada, H.Takada, M.Saruwatwri, and Nakagawa, "2Gb/s operation of an optical-clock-driven monolithically integrated GaAs D-flip-flip with

metal-semiconductor-metal photodetectors for high-speed synchronous circuits", IEEE Photon. Technol. Lett., vol.4, pp.160-163, 1992.

[1.21] M.Ersoni, X. Wu, P.E.Jessop, and J.P.Noad, "Optical Signal Distribution in Waveguide-Coupled Metal-Semiconductor-Metal Detector Arrays", J.Lightwave Commun., vol.15, pp.328-333, 1997.

[1.22] M. Ersoni, "Optical waveguide interconnects in optoelectronic matrix switches ", 1995.

[1.23] A.Alping, X.S.Wu, T.R. Hausken, and L.A.Coldren, "Highly efficient waveguide phase modulator for integrated optoelectronics", Appl. Phys. Lett., vol.48, pp.1243-1245, 1986.

[1.24] Y.Noda, M.Suzuki, Y.Kushiro, and S.Akika, "High-speed electroabsorption modulator with strip-loaded GaInAsP planar waveguide", J. Lightwave Technol., vol.LT-4, pp.1445-1453, 1986.


[2.1] T.Sugeta, T. Urisu, S. Sakata, and Y. Mizushima, "Metal-semiconductor-metal photodetector for high speed optoelectronic circuits", Jpn. J. Appl. Phys., Suppl. 19-1, **19**, 459-464 (1980)

[2.2] C.W.Slayman and L. Figueoa, "Frequency and pulse response of a novel high speed interdigital surface photoconductor (IDPC)", IEEE Trans. Electron Devices Lett. EDL-2, 112-112 (1981)

[2.3] C.J.Wei, H.-J. Klein, and H. Beneking, "Symmetrical Mott barrier as a fast photodetector", Electron. Lett., 17, 688-689 (1981)

[2.4] Liann-Chern Liou and Bahram Nabet, "Simple analytical model of bias dependence of the photocurrent of metal-semiconductor-metal photodetectors", Appl.Opt.,35(1), 15-23,1996.

[2.5] S.M.Sze, D.J.Coleman, Jr., and A. Loya, "Current transport in metal-semiconductor-metal (MSM) structure", Solid-State Electron., 14, 1209-1218 (1971)


[3.1] C.M.Kim, "Analysis of dielectric rectangular waveguide by modified effective index method", Electron. Lett., 22(6), pp.296-297, 1986.

[3.2] G.P.Agrawal and N.K.Dutta, "Semiconductor Lasers", pp.47-48, 1993.

[3.3] H. F.Taylor and A. Yariv, "Guided Wave Optics", Proc. IEEE, 62(8), 1044-1060, 1974.

[3.4] R.G. Honsperger, "Integrated Optics: Theory and Technology", 3rd edition, Chpater 3, p.31, Springer-Verlag, 1991.

[3.5] David Yevick and Björn Bermansson, "New formulations of the matrix beam propagation method: application to rib waveguides", IEEE J. Quan. Electron., 25(2), pp.221-229, 1989.

[3.6] B.Hermannsson and D.Yevick, "Numerical analyses of the model eigenfunctions of chirped and unchirped multiple-stripe-geometry laser arrays", J.Opt. Soc. Amer. A., vol.4, pp.379-390, 1987.

[3.7] Marko Erman, Philippe Jarry, Remi Gamonal, Jean-Lous Gentner, Pascal Stephan, and Critophe Guedon, "Monolithic Lutegration of a GaInAs p-i-n Photodiode and an Optical Waveguide Modeling and Realization Using Chloride Vapor Phase Epitaxy", J. Lightwave Technol., 6(3), pp. 399-411, 1988.

[3.8] Anders Larsson, Peter A. Andrekson, Sverre T. Eng, and Amnon Yariv, "Tunable Superlattice p-i-n photodetectors: Characteristics, Theory, and Applications", IEEE J. Quantum Electron., 24(5), pp. 787-798, 1988.

[3.9] Sadao Adachi, "GaAs, AlAs, and $Al_xGa_{1-x}As$: material parameters for use in research and device applications", J.Appl. Phys., 58(3), R1-R26, 1985.

[3.10] H.C.Casey, Jr., D.D.Sell, M.B.Panish, Appl. Phys. Lett., vol.24, 633, 1974.

[3.11] Sadao Adachi, "Optical dispersion relations for GaP, GaAs, GaSb, InP, InAs, InSb, $Al_xGa_{1-x}As$, and $In_{1-x}Ga_xAs_y P_{1-y}$", J.Appl. Phys. 66(12), 6030-6040,1989.

[3.12] T.S.Moss and T.D.H.Hankins, "Infrared absorption in Gallium Arsenide", Infrared Phys., 1, pp.111-115, 1961.

[3.13] M.D.Sturge, "Optical absorption of Gallium Arsenide between 0.6 and 2.75eV", Phys. Rev., 127(3), pp.768-773, 1962.

[3.14] D.D.Sell and H.C.Casey, Jr., "Optical absorption and photoluminescence studies of thin GaAs layers in $GaAs-Al_xGa_{1-x}As$ double heterostructure", J.Appl. Phys., 45(2), pp.800-807, 1974.

[3.15] H.C.Casey, Jr., D.D.Sell and K.W.Wecht, "Concentration dependence of the absorption coefficient for n- and p-type GaAs between 1.3 and 1.6eV", J.Appl.Phys.,46(1),250-257,1975.

[3.16] D.E.Aspnes and A.A.Studna, "Dielectric functions and optical parameters of Si, Ge, GaP, GaAs, GaSb, InP, InAs, and InSb from 1.5 to 6.0eV", Phys. Rev. B, vol.27, 985, 1983.

[3.17] M.C. Amann, "Analysis of a p-i-n photodiode with integrated waveguide", Electron. Lett., vol.23, pp.895-897, 1987

[3.18] M.Ersoni, X. Wu, P.E.Jessop, and J.P.Noad, "Optical Signal Distribution in Waveguide-Coupled Metal-Semiconductor-Metal Detector Arrays", J.Lightwave Commun., vol.15,pp.328-333, 1997.

[3.19] R.A. Logan and F.K.Reinhart, "Optical waveguides in GaAs-AlGaAs epitaxial layers", J.Appl. Phys., 44(9), pp. 4172-4176, 1973.


[4.1] W.Franz, "Einfluss Eines Elecktrischen Feldes auf Eine Optisore Absorptionskante", Z. Naturforschg, 13a, 484 (1958)

[4.2] L.V.Keldysh, "The effect of a strong electrical field on the optical properties of insulating crystals", Soviet Phys. JETP, 34, 788-790, 1958

[4.3] R.Williams, Phys. Rev., 117, 1487 (1960)

[4.4] T.S.Moss, J. Appl. Phys., 32, 2136 (1962)

[4.5] K.Tharmalingam, "Optical absorption in the presence of a uniform field", Phys. Rev., 130, 2204-2206 (1963)

[4.6] Joseph Callaway, "Optical absorption in an electric field", Phys. Rev., 130(2), 1963.[6] B.O.Seraphin, Phys. Rev., 140, A1716 (1965)

[4.7] G.E.Stilllman, C.M.Wolfe, C.O.Bolzler and J.A.Rossi, "Electroabsorption in GaAs and its application to waveguide detectors and modulators", Appl. Phys. Lett., 28, 544 (1976)

[4.8] A. Schmeller, W. Hansen, J.P. Kotthams, G.Tränkle, and G. Weimann, "Franz-Keldysh effect in a two-dimensional system", Appl. Phys. Lett., 64(3), pp. 330-332, 1994.

[4.9] J.I.Pankove, "Optical process in semiconductors", p29, Prentics Hall, Englewood Cliffs, NJ, 1971.

[4.10] Brian R. Bennett and Richard A. Soref, "Electrorefraction and electroabsorption in InP, GaAs, GaSb, InAs, and InSb",IEEE J.Quan. Electron., vol.QE-23, No.12, pp.2159-2166,1987.

[4.11] F.W.J.Olver, "Asymptotics and Special Functions", New York:Academic, 1974, pp.392-393.

[4.12] Shun Lien Chung, "Physics of optoelectronic devices", p544, John Wiley & Sons, Inc., 1995.

[4.13] Shun Lien Chung, "Physics of optoelectronic devices", p546, John Wiley & Sons, Inc., 1995.

[4.14] D.A.B.Miller, D.S.Chemla, T.C.Damen, A.C.Gossard, W.Wiegmann, T.H.Wood andC.A.Burrus, "Electric field dependence of optical absorption near the band gap of quantum-well structure", Phys. Rev. B, 32(2), pp.1043-1055, 1985.

[4.15] X.C. Wu, Ph.D. Thesis, 1998.


[5.1] P.K.Willardson and A.C.Beer, "Semiconductors and Semimetals",Vol.9, p300, AP.1972

[5.2] Joseph Callaway, "Optical absorption in an electric field", Physical Review, 134(4A), A998 (1964)

[5.3] T.Coroy and R.M.Measures, "Active wavelength demodulation of a Bragg grating fibre optic strain sensor using a quantum well electroabsorption filtering detector", Electron. Lett., 32, pp.1811-1812, 1996.

[5.4] M.A.Davis and A.D.Kersey,"Application of a fiber fourier transform spectrometer to the detection of wavelength-encoded signals from Bragg grating sensors", J.Lightwave Technol., 13, pp.1289-1295, 1995.

[5.5] X. Wu, D.M.Bruce, P.E.Jessop, B.J.Robinson, and D.A.Thompson, "A wavelength monitor based on electroabsorption in quantum well waveguide photodetectors", 1997.

[5.6] K.J.Cearns, X. Wu, A. Densmore, P.E.Jessop, B.J.Robinson and D.A.Thompson, "A two-element optical waveguide photodetector for wavelength monitoring in fiber optic strain sensors", 1997.

[6.1] R.I. MacDonald, "Optoelectronic matrix switching", Can.J.Phys., Vol.67, 389-393,1989.

[6.2] Liann-Chern Liou and Bahram Nabet, "Simple analytical model of bias dependence of the photocurrent of metal-semiconductor-metal photodetectors", Applied Optics, vol.35(1), pp.15-23 (1996)

[6.3] B.Sapoval and C. Hermann, "Physics of Semiconductors", pp.252-253, Springer-Verlag New York, Inc., 1995.

[6.4]H.Takeuchi and K.Oe, "Low-loss single-mode GaAs/AlGaAs miniature optical waveguides with straight and bending structures", J. Lightwave Technol., vol. 7, pp.1044-1054, July 1989.

[6.5] G.wenger, L.Stoll, B.Weiss, M.Schienle, R.Muller-Nawrath, S,Eichinger, J.Muller, B.Acklin, and G.Muller, "Design and fabrication of monolithic optical spot size transformers (MOST's) for highly efficient fiber-chip coupling", J.Lightwave Technol.,12,1782-1790,1994.

[6.6] C.T.Sullivan, S.D.Mukherjee, M.K.Hibbs-Brenner, A.Gopinath, E.Kalwert, T.Marta, W.Goldberg, andR.Walterson, "Switched time delay elements based on AlGaAs/GaAs optical wabeguide technology at 1.32um for optically controlled phased array antennas", Optic. Technol. Microwave Appl. VI and Optoelectron. Signal Processing for Phased-Array Antennas III Proc. SPIE, 1992, vol.1703, pp.264-271.

[6.7]Y.Shani, U.Koren, B.Miller, M.Young, M.Oron, and R.Alferness, "Buried rib passive waveguide Y junctions with sharp vertex on InP", IEEE Photon. Technol. Lett., vol.3, pp.210-212, Mar. 1991.

[6.8] G.Allen Vawter, Robert E.Smith, Beth Fuchs, Joel R.Wendt, Mike Hafich, and G.Ronald Hadley, "A rib optical waveguide with cutoff mesa isolation", J. Lightwave Techol., vol.14(20) 169-172, Feb. 1996.

[6.9] M.Veillenx, R.I.MacDonald, F.Gouin, and J.Noad, "High isolation optoelectronic switch matrix", International Topical Meeting on Photoic Switching (Kobe, Japan), 1990.

[6.10] M.Veilleux and R. Ian MacDonald, "An Optoelectronic Switching Matrix With High Isolation", J. Lightwave Technology, Vol.10(7), 988-991 (1992)

[6.11] M.Ersoni, "Optical waveguide interconnects in optoelectronic matrix switches", 1995.